Nanostructure of Dip-Coated Yttria-doped Zirconia Sol-Gel Coatings Studied by Grazing-Incidence Small-Angle X-ray Scattering

by

Kristin Høydalsvik

Aberystwyth University (AU)
2010
Dr. Rudolf Winter - Supervisor

THESIS
submitted to Aberystwyth University
by
Kristin Høydalsvik, B.Sc, M.Sc
In Candidature for the Degree of
PHILOSOPHIAE DOCTOR

Declaration

This work has not previously been accepted in substance for any degree and is not being concurrently submitted in candidature for any degree.

Signed ..... (candidate)

Date .....

Statement 1

This thesis is the result of my own investigations, except where otherwise stated. Other sources are acknowledged by footnotes giving explicit references. A bibliography is appended.

Signed ..... (candidate)

Date .....

Statement 2

I hereby give consent for my thesis, if accepted, to be made available for photocopying and for inter-library loan, and for the title and summary to be made available to outside organisations.

Signed ..... (candidate)

Date .....

Abstract

In this work, X-ray techniques have been used to study coatings of zirconia and yttria doped zirconia. The experimental techniques used were laboratory-based X-ray diffraction (XRD) and synchrotron radiation based small-angle X-ray scattering techniques in both transmission mode; small-angle X-ray scattering (SAXS), and reflection mode; grazing-incidence small-angle x-ray scattering (GISAXS).

By using XRD and (GI)SAXS measurements, information has been gained about the crystal structure of the coatings, and about the size- and surface structure of the scattering particles, respectively.

Two types of *in situ* experiments were performed; *in situ* dipping-and-heating cycles, and *in situ* incremental heating. SAXS was used for the measurements on the former, whilst both SAXS and GISAXS was used for the latter.

The coatings have been studied at various stages during calcination, and a novel methodology used for tracing the morphology quantitatively in systems subject to change, is presented here. This type of measurement and methodology is important, for example, in understanding mechanisms of corrosion and catalysis or ageing of materials.

I found that the coatings transform from polymeric gels to particulate films featuring agglomeration and Ostwald ripening, as the sample is heated. The yttria concentration was found to influence the size- and the surface structure of the scattering particles; the more yttria, the smaller particles. When the samples were heated, I found that the particles within the coatings with higher yttria concentration gets a rougher surface structure at lower temperature than the particles in the lower yttria concentration coatings.

Acknowledgements

I would like to thank Armin Hoell, Dragomir Tatchev and Sylvio Haas at BESSY II for their help with the GISAXS experiments, and Chris Martin and Graham Clark at SRS Daresbury for their help with the SAXS measurements. Also, many thanks to Twilight Barnardo for teaching me about sol-gel techniques and for helping with the experiments.

I would also like to thank Matt Gunn, Dave Francis, John Parry, Les Dean, Dave Lewis and Clive Willson for designing and building the GISAXS furnace and the dip-coater, the late Tudor Jenkins for the ellipsometry result, Pascal Lenormand (Université Paul Sabatier, Toulouse) for useful information about XRR results on zirconia films, Dag W. Breiby and Ingve Simonsen (Norges Teknisk-Naturvitenskapelige Universitet, Trondheim) for helpful discussions, and Justin Wells for proof-reading as well as helpful discussions. I would also like to thank Matt Gunn and Richard Fallows for taking photos.

And most of all, I would like to thank Rudi Winter for keeping his office door open, for his patience and great supervision.

Contents

Chapter 1

Zirconia- and yttria-stabilised zirconia coatings

1.1 Background

Materials that are exposed to working conditions far from ambient, such as high temperatures, oxidising or reducing atmospheres, corrosive and abrasive environments may soon exhibit reduced functionality and damage as a consequence. Examples of such devices are furnaces, incinerators and gas-turbines. One method of protecting the material in such devices is to apply a protective coating, such as a ceramic layer. Ceramic materials are often used for this application since they are having long traditions as refractory materials. An example of such a ceramic protective coating will be given in the following section, and some more theory about this material including the relevant descriptions of the crystal structure will

be given in section 1.1.2.

1.1.1 Thermal barrier coatings

Yttria-stabilised zirconia (YSZ) is a ceramic which has been found to have many applications as a protective coating, and for example, zirconia-based thermal barrier coatings have been developed for aero gas turbines, and they are presently used in aircraft engines [1].

The performance and efficiency of a gas turbine engine are directly related to the operating temperature [2; 3]. In order to protect the metal, thermal barrier coatings are used, consisting of a ceramic insulating layer on top of an intermediate metallic bond coat layer which is deposited directly on the metal. This offers protection for hot section components of the gas turbine against oxidation and hot corrosion [2; 1], and the reduction in metal temperature is now of around 100 °C; this is nicely illustrated by Taylor *et al.* (see figure 1 in [2]). The potential benefits are many; increased fuel economy, higher engine power, longer component life and reduced emissions [1].

The necessary criteria for the ceramic insulating layer is that it is refractory, chemically inert, phase stable, and that it possesses good mechanical strength and thermal shock resistance, good wear and erosion resistance, low thermal conductivity and a thermal expansion coefficient similar to that of the substrate.

The thermal expansion of the metal substrate, which is relatively high, dictates the thermal expansion needed from the ceramic layer. Few ceramics are having

a high thermal expansion coefficient, but zirconia does [2]. However, zirconia is having a problem with phase transitions, but this problem can be solved by making alloys with other oxides to obtain stabilised zirconia, as will be described in Section 1.1.3. Terblanche [4] studied yttria-stabilised cubic zirconia of different yttria contents in 1989, and this author found no significant differences in the thermal expansion of the different samples. However, in 2005 Hayashi *et al.* showed that for the temperature range -170 to 603 °C, the thermal expansion coefficient of YSZ decrease with the increase of yttria content [5].

1.1.2 Zirconia

Zirconia (ZrO_2) is a ceramic material that is considered as one of the most shock-resistant, corrosion-resistant and refractory materials [6]. In principle, zirconia would therefore be a useful material for lining furnaces, incinerators *etc.* However, zirconia crystal undergoes two reversible phase transitions:

1. m → t: Monoclinic (m) to tetragonal (t)

2. t → c: Tetragonal (t) to cubic (c)

as the temperature is increased. These crystal structures are described below, the webpage in Ref. [7] is recommended for better visualisation of these structures.

At ambient temperatures, zirconia is found in the monoclinic phase belonging to the space group $P2_1/c$ (No. 14), and has four molecules per unit cell [6]. The Zr^{4+} cations and O^{2-} anions all occupy the nonequivalent 4e positions in the lattice [8].

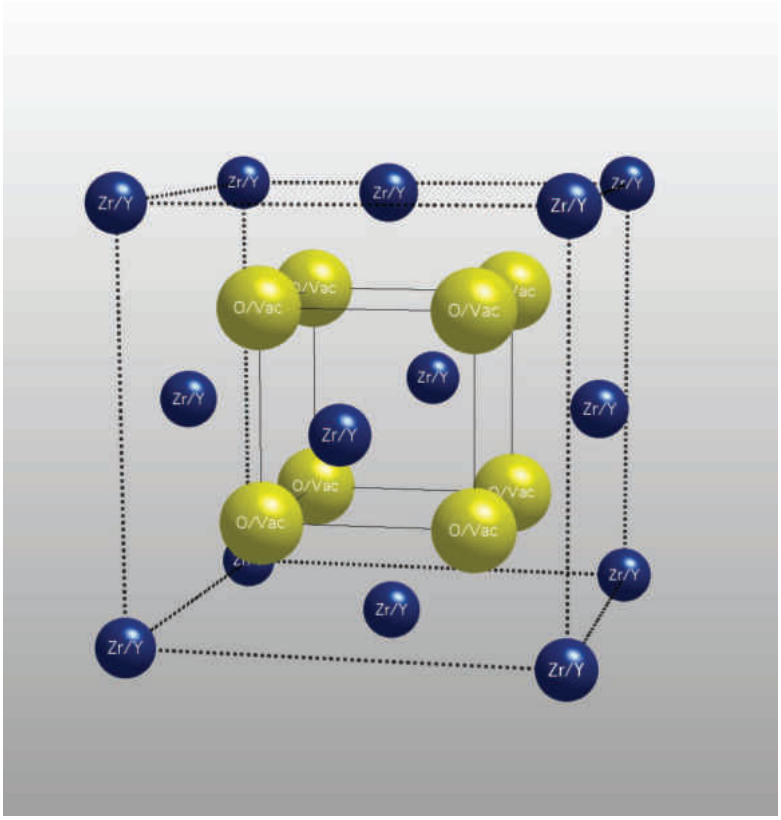

Figure 1.1: In the fluorite structure, the cations (dark blue, Y/Zr) form a fcc structure and the anions (yellow, oxygen/vacancies) form a simple cubic structure.

At higher temperatures, zirconia is found in the tetragonal phase belonging to the space group $P4_2/nmc$ (No. 137). The number of ZrO_2 molecules in each unit cell is in this case two, and Zr^{4+} cations occupy the 2b position and O^{2-} anions occupy the 4d positions [8].

Zirconia can also have a cubic crystal structure, which is typically found when zirconia has been heated to even higher temperatures. From Bragg reflections in X-ray diffractograms, cubic zirconia has been found to form the ideal *calcium fluorite structure* with lattice parameter $a = 5.135(9)$ Å [8] and in the space group $Fm\bar{3}m$ (No. 225) [8; 6; 9] with four ZrO_2 molecules per unit cell. The Zr^{4+} ions

are situated in an fcc lattice (the 4a positions), and the O^{2-} ions are situated in a simple cubic array within the calcium fluorite structure (the 8c positions), as shown in figure 1.1.

The temperature for which the crystal structure of zirconia changes from monoclinic to tetragonal is reported differently in different studies, for example, (in °C): 1100 [10], 1150 [6] and 1170 [8; 11]. The experimental results are often controlled by the small quantities of impurities, and Subbarao and Maiti claim that the "intrinsic behaviour is never observed" [10]. The t → c transition has been reported to take place at (in °C): 2350 [6] and 2370 [8; 11]. Scott [12] rather gives the transition temperatures on cooling, and here the c → t transition is reported to be at 2340 °C, and the t → m transition at 1170 °C. However, Salas [6] writes that this transition has a large hysteresis such that the m → t transition takes place at 1170 °C whilst the t → m transition is between 850 and 1000 °C.

The t → m transition causes substantial volume increase (of around 3 %), and this reduces the mechanical performance of the material [6]. With such large differences in volume, the thermal deviations that arises through the transformations tend to shatter objects of pure ZrO_2.

1.1.3 Yttria-stabilised zirconia

The problematic crystal structure transition can be avoided by letting zirconia remain in the tetragonal or cubic phase when cooled to ambient temperatures. This can be achieved by adding dopants to the zirconia. Several cations of lower

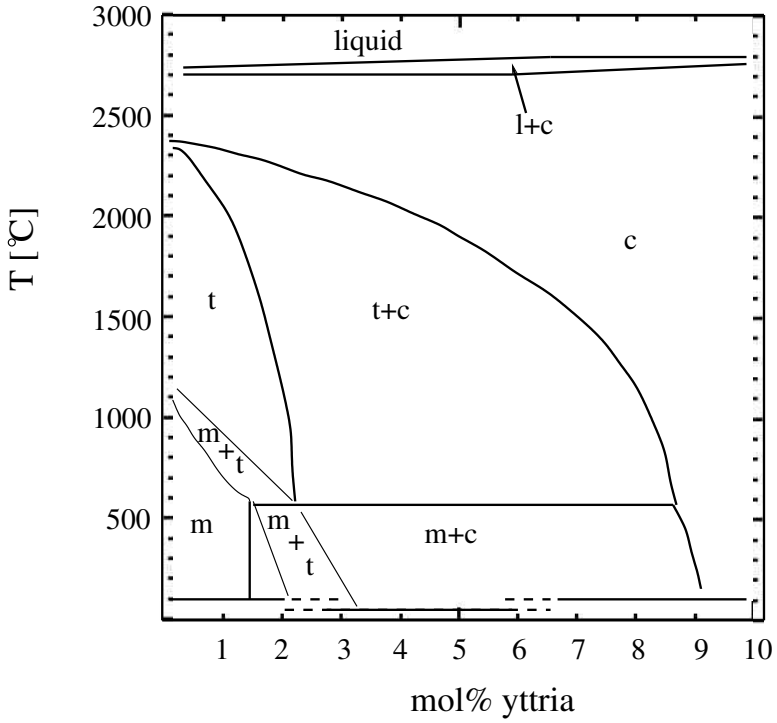

Figure 1.2: Phase diagram for the ZrO_2-Y_2O_3 system. "m", "t","c" and "l" refers to monoclinic, tetragonal, cubic fluorite and liquid structure, respectively. Information from [12] and [13].

valence than zirconium have been found to stabilise the zirconia in the tetragonal- and/or cubic phase, for example Y_2O_3, CaO, MgO and Ce_2O_3 [8]. However, since yttria is one of the most commonly used stabilising materials, this is the one that will be discussed further in this work.

1.1.3.1 Yttria concentration

From the phase diagram in figure 1.2, it is observed that the cubic form of yttria-stabilised zirconia (YSZ) is stable down to room temperature for concentrations larger than about 9 mol% yttria. When the concentration is between 0 and 2.25 mol% yttria then the temperature for the m $\rightarrow$ t phase transition is lowered

progressively. [12]

1.1.3.2 Yttria stabilisation of zirconia

When zirconium is replaced with yttrium ions, then one yttria formula unit replaces two zirconia formula units: $Y_2O_3 \rightarrow 2 \cdot ZrO_2$, and from this it is observed that there must be one oxygen vacancy for each pair of zirconia molecules that is replaced by an yttria molecule.

Salas *et al.* writes that [6]: "It is generally accepted that the mechanism associated with this phase stabilisation, is the generation of metastable states in the system due to the presence of vacancies in the oxygen sublattice which in turn produce internal shear deformations" and that "these internal shear deformations in the oxygen sub-lattice reduces the phase-transition temperature, leading to the formation of stabilised zirconia at room temperature." Additionally, by studying YSZ during *in situ* heating using ASAXS (anomalous small-angle X-ray scattering), the suggested mechanism for stabilisation is that pure zirconia crystals initially nucleate and absorb yttria as they grow, which results in stabilisation of the cubic phase [14]. These are just a couple of examples; despite a great amount of studies performed using different techniques, the exact nature of YSZ is still not clear [15].

1.1.3.3 Conductivity of oxygen ions

From the previous discussion, it is clear that there are oxygen vacancies in the YSZ lattice. At high temperatures oxygen atoms in the lattice become quite mobile;

hopping through the vacant sites and displaying substantial conductivity [6]. The highest conductivity is found for dopant concentrations of around 8-10 mol% yttria [16; 11]. When the concentration is less than 10 mol% yttria, oxygen vacancies are found to be distributed at random, although distortion of the cubic structure is observed. On the other hand, when the concentration exceeds 10 mol% yttria, the ionic conductivity decreases, which is thought to be caused by the fact that short-range ordering of oxygen vacancies arises, and this imparts the oxygen-ion transport [15]. More work is needed, however, in order to properly explain the effect of yttria concentration on the oxygen-ion transport.

1.1.4 Applications of YSZ

In addition to be a good material for *thermal barrier coatings*, as was discussed in the beginning of this chapter, YSZ has several different applications which are described in this section.

1.1.4.1 Ionic conduction

Because of YSZ's ability to conduct oxygen ions, YSZ is used in particular applications where *ionic conduction* is needed:

Solid oxide fuel cells (SOFCs) are a class of fuel cell characterised by the use of a solid oxide materials. The cell is constructed with an electrolyte that is sandwiched between the two porous electrodes. When an oxygen molecule hits the cathode-electrolyte interface, it acquires electrons from the cathode. The oxygen

ions diffuse into the electrolyte material and migrate to the other side of the cell where they contact the anode. At the electrolyte-anode interface, the oxygen ions encounter the fuel and react catalytically, giving off water, carbon dioxide, heat and electrons [17]. Since the anode is connected to the cathode through an external circuit, the released electrons are transported from the anode to the cathode, and thus providing electrical energy.

One of the requirements to the electrolyte material is that it must have a good ability of conducting oxygen-ions, and due to the oxygen-ion conducting properties of YSZ, it is used as electrolyte in SOFCs. A challenge in the SOFC industry, is that there must be a trade-off between ion-conduction (high), operating temperature (low) and production costs (low). As a compromise of these, YSZ is currently one of the best electrolyte materials available. For time being, the operating temperature of SOFCs is between 600 to 1000 °C [17]; the oxygen-ion conduction stops if the temperature becomes too low.

Oxygen sensors are electronic devices that measures the proportion of oxygen (O_2) in the gas or liquid that is being analysed. The most common application is to measure the concentration of oxygen in the exhaust gas for internal combustion engines in cars and other vehicles. Again, because of the oxygen-ion conducting properties of YSZ, this material is used as electrolyte.

An oxygen sensor consists of an YSZ electrolyte that is sandwiched between the two electrodes. These two electrodes are connected by an external circuit. The output voltage measured in this circuit, corresponds to the quantity of oxygen in

the exhaust relative to that in the atmosphere.

1.1.4.2 Optics

Due to the high refractive index of cubic stabilised zirconia (n=2.16) for light at the air-material interface, one of the main uses is in glazes as an opacifier, and it is also used to increase the refractive index of other materials [6]. The refractive index and the scattering power of cubic zirconia is comparable to that of diamond, and this material is therefore popular as a substitute for diamond.

1.2 Sol-gel processing

The sol-gel process combined with dip-coating is a convenient method of making films and coatings containing a well defined doping level and a homogeneous distribution of dopants. The dip-coating procedure will be described in the experimental chapter (Section 3.2.3), and the aim in this section is to give an overview of sol-gel theory for the sols used in this work.

The recipe used for the zirconia sol was based on previous work within our own research group; Twilight Barnardo did an excellent job in optimising the different parameters, especially the volumetric ratios used (which are given in Section 3.2.2). The sol-gel processes and the reasons for using these specific ratios are described very well in Barnardo's thesis [18], and only the most relevant sol-gel theory for producing zirconia-sols is repeated here.

Zirconium(IV)propoxide was used as a precursor for zirconium; this type of

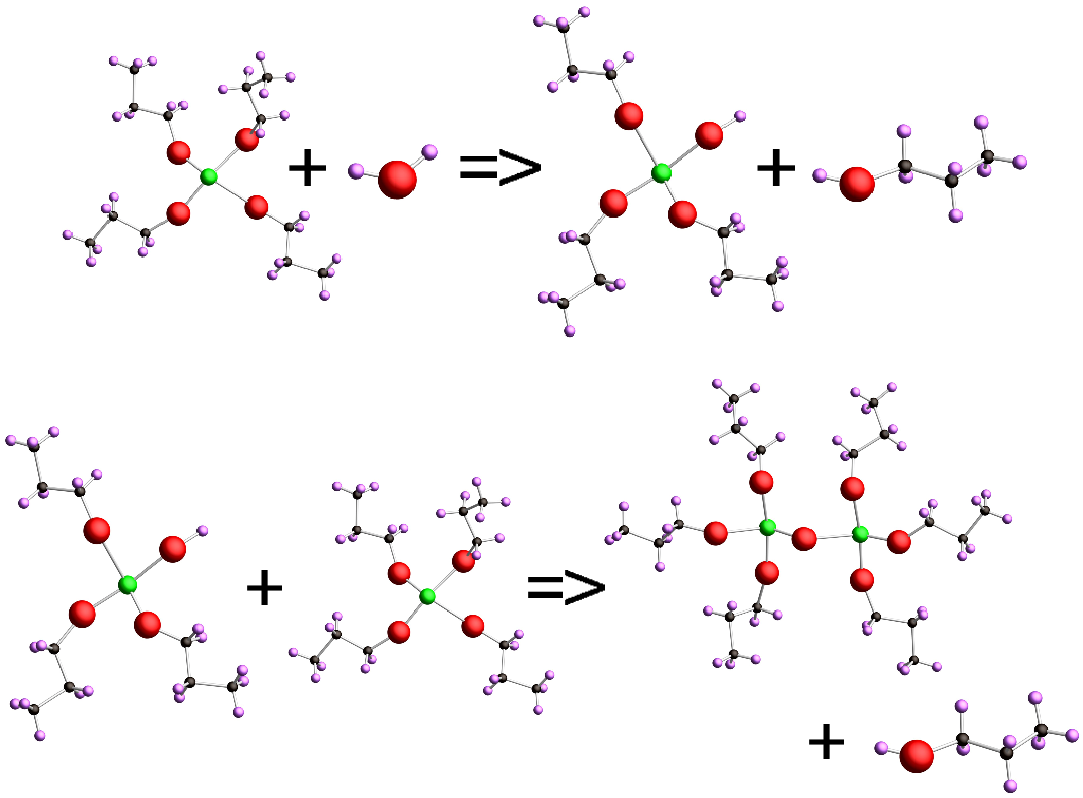

Figure 1.3: Schematic representation of the sol-gel reactions: Zirconium (green), oxygen (red), carbon (black), hydrogen (purple). Upper row: Zr(O nPr)$_4$ reacts with water and forms ZrOH(O nPr)$_3$ and propanol. Bottom row: The newly formed ZrOH(O nPr)$_3$ molecule reacts with a new precursor molecule and starts forming a Zr-O-Zr network and residual propanol.

molecule is illustrated in the upper left hand corner of figure 1.3. When water is added to the zirconium precursor molecules (Zr(O nPr)$_4$), the reaction

$$\mathrm{Zr(O\ nPr)_4 + H_2O \rightarrow ZrOH(O\ nPr)_3 + nPr\ OH} \tag{1.1}$$

starts taking place, as illustrated in the upper row of figure 1.3. nPr is $CH_2CH_2CH_3$, and the last term in the equation is propanol: nPr OH = $CH_3CH_2CH_2OH$. In this reaction then, one of the (nPr) chains leaves the Zr-atom, and is replaced

with an H-atom from the water molecule. The rest of the water molecule reacts with the nPr chain that left, and forms propanol.

In the *gelation process*, the new modified molecules react with new precursor molecules as illustrated in the bottom row of figure 1.3, and start forming a network of Zr-O bonds:

$$\mathrm{Zr(O\ nPr)_4 + ZrOH(O\ nPr)_3 \rightarrow (nPr\ O)_3 - Zr - O - Zr - (O\ nPr)_3 + nPr\ OH} \quad (1.2)$$

Some additional chemicals are also needed in order to produce a clear sol successfully, and in the case of a zirconia sol; acetylacetone, acetic acid and isopropanol are used, and the reasons will be explained below.

The role of acetylacetone is to be a "chelating agent". In order to produce clear homogeneous gels and sols for transition metals, a chelating agent needs to be introduced to make the transition metal ions coordinately saturated.

Acetic acid is often used for its property as a proton donor. It also prevents precipitation and acts to slow the polymerisation reactions. An overly acidic environment will result in a clear sol where no polymerisation reactions occur.

Water makes the sol-gel reactions happen very fast, but too fast reactions are not desirable since this often leads to precipitation. Adding isopropanol to the water slows down the reactions.

Yttria doping was obtained by crunching the grains of yttrium nitrate hexahydrate ($\mathrm{Y(NO_3)_3 \cdot 6H_2O}$) and adding it to the isopropanol+water solution before it

was mixed with the other solution.

The residual hydrocarbons coexist with the polymerised metal complexes in the sol after the gelling reactions (Eqs. (1.1) and (1.2)) have taken place. This is the reason for why drying the produced gels is necessary. Drying is typically achieved by heat treatment. The drying process causes the residual hydrocarbons and the water molecules to evaporate, and the nitrates to decompose by releasing NO and NO_2.

The exact positions of the yttrium ions in the resulting gel are not clear, but it has been suggested that pure zirconia crystals initially nucleate and absorb yttria as they grow [14]. The yttrium ions will then substitute for zirconium ions in the lattice.

Summary

Some of the theory on the structural properties of zirconia and yttria-stabilised zirconia (YSZ) was reviewed in this chapter. YSZ has numerous applications, such as thermal barrier coatings, fuel cells, oxygen sensors and several optical applications. A convenient way of producing YSZ is by using sol-gel processes, and some basic theory of these chemical processes are also given here. Further on in this work, the nano-structure of zirconia and YSZ coatings are studied using X-ray techniques, and these techniques will be described in the following chapter.

Chapter 2

X-ray techniques in material science

2.1 Introduction

X-ray techniques such as SAXS (Small-Angle X-ray Scattering), GISAXS (Grazing-Incidence -SAXS) and XRD (X-Ray Diffraction) are well suited for studying the heating effects on coatings *in situ*, and the principle of small-angle X-ray scattering, starting with some background information for X-rays, is discussed in this chapter.

2.1.1 X-rays

X-rays are electromagnetic radiation which are having wavelength (denoted by λ) in the range 0.1 to 100 Å. The X-ray energy, E, is related to the wavelength by

$E = (hc)/\lambda$, where h is Planck's constant and c is the velocity of light in vacuum. Consequently, the energy range of X-rays is from 120 eV to 120 keV.

The light used for studying an object needs to have a wavelength comparable to or smaller than the size of the object in question. Consequently, it is not possible to study the atomic structure of a crystal, where the separation of the atoms is typically 2 Å, unless the wavelength of the light is on the order of a few Å, or smaller.

In 1912 the German physicist Max von Laue suggested that X-rays could be used for probing the atomic structure of crystals because of the comparable size of the interatomic spacing and the wavelength of the X-rays. Because of this, von Laue suggested that a crystal might be capable of strongly diffracting these rays, acting like a grating. This has indeed been found to be the case, and William Lawrence Bragg explained this diffraction using a simple model where X-rays are being reflected by flat lattice planes in a crystal. The constructive interference from the reflected beams produce a diffraction pattern.

Let d denote the distance between the lattice planes, then the difference in path-length between two beams is given by $2d \sin \theta_B$ where θ_B is the angle between the lattice plane and the beam. Constructive interference occurs when the difference in path-length is equal to $n\lambda$, and the resulting equation is called Bragg's law:

$$n\lambda = 2d \sin \theta_B \tag{2.1}$$

2.2 Small-angle X-ray scattering

In the 1930's it was observed experimentally that certain samples cause an intense, continuous scattering at small angles ($< 2°$) which were lacking a typical X-ray diffraction pattern [19]. This was first observed by Krishnamurti [20] and Warren [21] for different samples containing fine particles of submicroscopic size. The scattering observed is due to the halo produced by the passage of a beam in a powder where the grain size is in the order of $100 \cdot \lambda$ [19]. This phenomenon is called *small-angle scattering*, and it is helpful for getting information from structures that are too large to be studied by X-ray diffraction.

At first it appears helpful to obtain an expression for the intensity of the scattered waves as a function of the scattering angle. It is, however, more useful to obtain an expression for the intensity of the scattered waves as a function of the wave-vector transfer, $I(q)$, where q is related to the scattering angle. From this we will be able to see how the size- and surface structure of the scattering objects can be found, and we start by considering the propagation of the X-rays hitting the scattering object. The propagation of electromagnetic waves, such as X-rays, along the direction $\mathbf{r}$ can, at the time t, be described by

$$\mathbf{E}(\mathbf{r}, t) = Ae^{i(\omega t - \mathbf{k}\cdot\mathbf{r})}\hat{\mathbf{e}}_y \tag{2.2}$$

where $\mathbf{E}$ is the electric field with the amplitude A, $\hat{\mathbf{e}}_y$ is the unit vector along

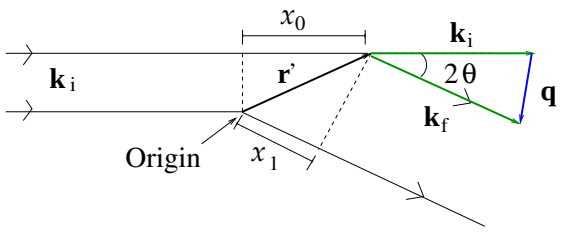

Figure 2.1: Illustration of the geometry of a scattering event. The scattering centre is situated at a position $\mathbf{r}'$ from the origin. We have assumed that the observation point is sufficiently far away from the scattering event that the rays can be considered to be parallel.

the electric field and ω is the angular frequency. $\mathbf{k}$ is the wave-vector, and the wave-number is the absolute value of $\mathbf{k}$,

$$k = |\mathbf{k}| = \frac{2\pi}{\lambda}. \tag{2.3}$$

Figure 2.1 illustrates a scattering event where the incoming wave has wave-vector $\mathbf{k}_i$ and the scattered wave $\mathbf{k}_f$. From this figure it is observed that

$$\sin\theta = \frac{|\mathbf{q}|/2}{|\mathbf{k}_i|} = \frac{q\lambda}{4\pi} \tag{2.4}$$

and, by rearranging, the relationship between the the magnitude of the wave-vector transfer q and the scattering angle 2θ is obtained as

$$q = \frac{4\pi}{\lambda}\sin\theta. \tag{2.5}$$

In the case of X-rays striking an object, every electron becomes the source of a scattered wave. The intensity of this scattering is constant, and practically equal to unity for the small angles considered here. [22]

The scattered waves are coherent and this means that the amplitudes are added and the intensity is then given by the modulus squared of the resulting total amplitude:

$$I(\mathbf{q}) = |A(\mathbf{q})|^2. \tag{2.6}$$

These amplitudes differ only by their phase ϕ which depends on the position of the electron. Every single secondary wave can be represented by $e^{i\phi}$, where the phase ϕ is given by [22]

$$\phi = \frac{2\pi p}{\lambda}. \tag{2.7}$$

p is the total path length difference between the optical path and some arbitrary reference point.

In the scattering event illustrated in figure 2.1, the scattering centre is not at the origin but at some position $\mathbf{r}'$ from the origin. The distance x_0 is given by

$$x_0 = \hat{\mathbf{k}}_i \cdot \mathbf{r}' = \frac{\mathbf{k}_i \cdot \mathbf{r}'}{k} = \frac{\lambda}{2\pi}(\mathbf{k}_i \cdot \mathbf{r}') \tag{2.8}$$

and, similarly

$$x_1 = \frac{\lambda}{2\pi}(\mathbf{k}_f \cdot \mathbf{r}'), \tag{2.9}$$

so that the path length difference, p, becomes

$$p = x_0 - x_1 = \frac{\lambda}{2\pi}(\mathbf{k}_i \cdot \mathbf{r}') - \frac{\lambda}{2\pi}(\mathbf{k}_f \cdot \mathbf{r}') = -\frac{\lambda}{2\pi}(\mathbf{q} \cdot \mathbf{r}') \tag{2.10}$$

where

$$\mathbf{q} \equiv \mathbf{k}_f - \mathbf{k}_i. \tag{2.11}$$

From Eq. (2.7), we get that the total phase change induced by the path difference p is given by [22],[23]

$$\phi = \frac{2\pi p}{\lambda} = -(\mathbf{q} \cdot \mathbf{r}'). \tag{2.12}$$

The total scattering amplitude is given by the sum of all the secondary waves from the electrons, each represented by $e^{-i\mathbf{q}\cdot\mathbf{r}'}$ ([22], p. 19). However, since the number of electrons is enormously large and since single electrons cannot be exactly localised, it is more useful to introduce the concept of electron density, $\rho_e(\mathbf{r}')$. A volume element $d\mathbf{r}'$ positioned at $\mathbf{r}'$ will therefore contain $\rho_e(\mathbf{r}')d\mathbf{r}'$ electrons. Because of the large number of electrons, the summation can be replaced by an integration over the volume V irradiated by the incident beam, and the scattering amplitude is thus given by [22]

$$A(\mathbf{q}, \mathbf{r}') = \int_V \rho_e(\mathbf{r}') e^{-i\mathbf{q}\cdot\mathbf{r}'} d\mathbf{r}'. \tag{2.13}$$

Consider a dilute solution of identical particles of constant electron density ρ_e embedded in a medium of another constant electron density $\rho_{e,0}$. Only the

difference in electron density, $\Delta\rho_e = \rho_e - \rho_{e,0}$, is relevant for scattering. If the particles are separated widely enough, it is plausible to assume that they will make independent, *i.e.* non-interacting, contributions to the scattered intensity. In this case, only one single particle needs to be considered at first. [22]

In real materials, the X-rays will be scattered by a range of particles that are having a variety of sizes and shapes. In order to understand the resulting patterns from the scattering experiments, it is useful to start by solving the simplest type of scattering problem and then advance in complexity:

(i) Scattering from one spherical particle

(ii) Scattering from many identical spherical particles

(iii) Scattering from many spherical particles of different sizes

(iv) Scattering from many particles of arbitrary shapes as well as different sizes

2.2.1 Scattering from a single particle

The simplest type of scattering problem will be considered first: The scattered amplitude from one particle of electron density ρ_e is given by [24]

$$A_p(\mathbf{q}, \mathbf{r}') = V_p \rho_e F(\mathbf{q}, \mathbf{r}'), \tag{2.14}$$

where V_p is the volume, and $F(\mathbf{q}, \mathbf{r}')$ is the amplitude of the form factor for the particle. Consequently, since the scattered intensity is the modulus squared of the amplitude,

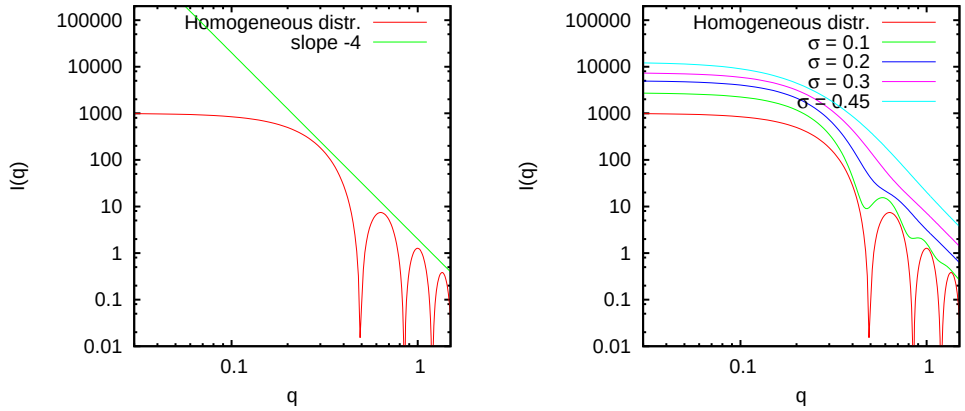

Figure 2.2: The simulated scattering pattern from spheres. Left: homogeneous distribution of particles of radius $R = 9.116$. Right: a distribution of particle sizes simulated by implementing a log-normal distribution for the particle sizes, where the median of the radius was set to 9.116 and using different standard deviations (σ).

$$I_p(\mathbf{q}, \mathbf{r}') = V_p^2 \rho_e^2 P(\mathbf{q}, \mathbf{r}'). \tag{2.15}$$

$P(\mathbf{q}, \mathbf{r}')$ is the form factor for the particle, and for spherical objects $P(q, r) = F^2(q, r)$ [24]. The form factor for homogeneous spheres was first derived by Lord Rayleigh in 1914 [25]. Appendix A shows the derivation of the form factor amplitude for a sphere, and it is found to be

$$F(q, R) = 3\frac{\sin(qR) - qR\cos(qR)}{(qR)^3} \tag{2.16}$$

where R is the radius.

2.2.2 Scattering from many particles

The scattering intensity from a single particle (see Eq. (2.15)) can be written as $I_p(\mathbf{q}, \mathbf{r}') = V_p^2(\Delta\rho_e)^2 P(\mathbf{q}, \mathbf{r}')$, where $\Delta\rho_e$ is the difference between the particle and the matrix electron density. For coherent scattering from many particles, this becomes $I(\mathbf{q}, \mathbf{r}') = N_p \cdot I_p(\mathbf{q}, \mathbf{r}')$, where N_p is the number of irradiated particles, and the scattering intensity from many particles is therefore given by

$$I(\mathbf{q}, \mathbf{r}') = N_p V_p^2(\Delta\rho_e)^2 P(\mathbf{q}, \mathbf{r}'). \tag{2.17}$$

The scattering pattern calculated using Eq. (2.17) with form factor from Eq. (2.16) (using that $P(q, r) = F^2(q, r)$) is shown in figure 2.2 (left panel).

However, all the particles does not have the same size, and it is reasonable to assume that the particle sizes follow a log-normal distribution (see, for example, [26]), given by

$$f(R; \sigma, \mu) = \frac{1}{R\sigma\sqrt{2\pi}} \cdot \exp\left(-\frac{(\ln R - \mu)^2}{2\sigma^2}\right) \tag{2.18}$$

where R is the radius of the particle, and μ is the mean, for different standard deviations, σ. In the right hand panel of figure 2.2, different widths of the size distribution are compared. In both panels, the red curve is for a homogeneous distribution of spheres. We are interested in the median R, see for example [27], and the median of this distribution is found from the solution of $(df(R; \sigma, \mu)/dR) = 0$:

$$R_{median}(\mu, \sigma) = e^{\mu - \sigma^2}. \tag{2.19}$$

For example, setting $\mu = 2.3$ and $\sigma = 0.3$, gives $R_{median} = 9.116$, and this is the value that is used for the particle radii in Eqs. (2.16) and (2.17) for simulating the intensities in figure 2.2.

2.2.2.1 Guinier's approximation

It is possible to extract information from the scattering curves about the particle sizes in the sample by investigating the behaviour of $I(q)$ at small q-values. The particle sizes may in theory be found by using the exact solutions discussed in the previous section for simulations if the particle system is well characterised. However, for an unknown particle system this method is not especially practical, and an approximation can be used with advantage. The most common approximation for extracting the particle size, is known as the Guinier approximation, and it can be derived as follows. First, the form factor for homogeneous spheres is found by squaring Eq. (2.16), and using that $P(q, r) = F^2(q, r)$ for spherical particles:

$$P(q, R) = 9 \left[\frac{\sin(qR) - qR\cos(qR)}{(qR)^3} \right]^2 \tag{2.20}$$

and rearranging,

$$P(q, R) = \frac{9}{(qR)^4} \left[\frac{\sin(qR)}{qR} - \cos(qR) \right]^2. \tag{2.21}$$

The next step in the derivation is to expand the trigonometric terms. The expansion for $\sin(qR)/(qR)$ is simply found by taking the Taylor expansion for $\sin(qR)$ (from for example Ref. [28]) and dividing each term by qR:

$$\frac{\sin(qR)}{qR} \approx 1 - \frac{(qR)^2}{3!} + \frac{(qR)^4}{5!}. \tag{2.22}$$

Similarly, the expansion for $\cos(qR)$ is [28]

$$\cos(qR) \approx 1 - \frac{(qR)^2}{2!} + \frac{(qR)^4}{4!}. \tag{2.23}$$

Inserting these expansions into Eq. (2.21), it can be seen that

$$\begin{aligned} P(q,R) &\approx \frac{9}{(qR)^4}\left[\left(1 - \frac{(qR)^2}{6} + \frac{(qR)^4}{120}\right) - \left(1 - \frac{(qR)^2}{2} + \frac{(qR)^4}{24}\right)\right]^2 \\ &= \frac{9}{(qR)^4}\left[\frac{(qR)^2}{3} - \frac{(qR)^4}{30}\right]^2 \\ &= \left(1 - \frac{(qR)^2}{10}\right)^2 \\ &= 1 - \frac{(qR)^2}{5} + \frac{(qR)^4}{100}. \end{aligned} \tag{2.24}$$

Since the last term is very small, $P(q,R)$ can be written as

$$P(q,R) \approx 1 - \frac{(qR)^2}{5}, \tag{2.25}$$

and by using the expansion $e^{-x} = 1 - x + (x^2/2) - \cdots$ [28], it can be observed that the following approximation is valid for small values of qR,

$$P(q,R) \approx \exp\left(-\frac{q^2R^2}{5}\right). \tag{2.26}$$

This equation can be adapted for an arbitrary shaped particle by using the radius of gyration R_g instead of the radius R. By analogy with classical mechanics, R_g can be considered as the electronic radius of gyration of the particle about its electronic centre of mass [19]. For a sphere, the radius of gyration is given by

$$R_g^2 = \frac{3R^2}{5}. \tag{2.27}$$

By using this, the form factor is now approximated by

$$P(q,R_g) \approx \exp\left(-\frac{q^2R_g^2}{3}\right). \tag{2.28}$$

The scattering intensity can be found from Eq. (2.17), where in this case

$$I(q) = N_pV_p^2(\Delta\rho_e)^2P(q,R_g). \tag{2.29}$$

Inserting Eq. (2.28) for $P(q,R_g)$ in the equation above, the scattering curve takes the form

$$I(q) \approx N_pV_p^2(\Delta\rho_e)^2\exp\left(-\frac{q^2R_g^2}{3}\right). \tag{2.30}$$

The approximation for the form factor $P(q,R)$ in Eq. (2.26) is called Guinier's approximation. It is a very good approximation at small angles, and remains valid

for $qR_g \lesssim 1.3$ for spherical particles [19]. This means that the particle size can be obtained by fitting a straight line to the low-q limit in a log (I) *vs.* q^2 plot, or by fitting an exponential curve on the log (I) *vs.* log (q) plot. A great advantage of the Guinier approximation is that the radius of gyration, *i.e.*, a size parameter, can be determined from uncalibrated small-angle scattering data. [29]

2.2.2.2 Porod Slope

The particle shape can be obtained by looking at the behaviour of the scattering pattern in the region towards the highest q-values. In this region the scattering pattern is representative of the surface properties of the particles; it is the relevant region for Porod's approximation which can be applied when $qR \gg 1$. Here

$$\lim_{qr\to\infty} \frac{\sin(qR)}{qR} = 0, \tag{2.31}$$

and Eq. (2.21) becomes

$$P(q) \approx \frac{9}{(qR)^4} \cos^2(qR). \tag{2.32}$$

For a distribution of particle sizes, the average of $\cos^2(qR)$ has to be used; $< \cos^2(qR) > = 1/2$. The scattered intensity (Eq. (2.17)) in this limit follows

$$I(q) = \frac{9}{2R^4} N_p V_p^2 (\Delta\rho_e)^2 q^{-4}. \tag{2.33}$$

This means that for smooth spheres, the scattered intensity will fall off with

q^{-4}. Eq. (2.33) can be rewritten as

$$I(q) \propto q^{-P}, \tag{2.34}$$

for arbitrarily shaped particles, where P is related to the surface structure and to the shape of the particles. For example, for rods $P = 1$ and for discs $P = 2$ [30]. From the value of P, the mass- (D_m) or surface- (D_s) fractal dimension of the scattering particles can be calculated. For a mass fractal, $P = D_m$, and since $1 \leq D_m \leq 3$, this means that if the value of P is between 1 and 3, the particle is having a mass fractal nature. On the other hand, if $3 \leq P < 4$, the particle is having surface fractal nature since $P = 6 - D_s$ and $2 < D_s \leq 3$ (see, for example, [31; 32]).

In a log (I) *vs.* log (q) plot, this slope is observed as a straight line at high q-values, and the slope of this line will be described by q^{-P}, where $-P$ is the value of the steepness of this slope, the *Porod slope* [29; 30]. This can be seen from, for example, figure 2.2. In the left hand panel a line of slope -4 is included. The line coincides with the maxima of the simulated scattering curve. The model used for simulating the patterns in this figure is based on a smooth sphere such that $P = 4$ (from the above discussion). For the more realistic scenario modelled in the right hand panel, especially for $\sigma = 0.45$, it is observed that the slope for the pattern at high-q values is also very close to -4.

2.2.2.3 Structure factor

If the particles are densely packed, interference effects arise. This can be accounted for by rewriting Eq. (2.17) as

$$I(\mathbf{q}, \mathbf{r}') = N_p V_p^2 (\Delta\rho_e)^2 P(\mathbf{q}, \mathbf{r}') S(\mathbf{q}), \tag{2.35}$$

where $S(\mathbf{q}) = 1$ over the whole q-range for dilute systems (see, for example, [24]). The form factor $P(\mathbf{q}, \mathbf{r}')$ is dependent on the shape of the particle, whilst the structure factor $S(\mathbf{q})$ depends on the way the particles interact. $S(\mathbf{q})$ describes inter-particle correlations and is a function of local order and inter-particle potentials. The inter-particle interactions cause a change in the shape of the scattering curve, particularly at low q-values, with the appearance of a maximum in this region.

The structure factor used in this work is based on the Hosemann model for paracrystalline systems [33; 34]. Another model was also tested; the semi-empirical function for $S(q)$ in [35; 36], which describes damped spherical correlations of colloidal particles, and was found to give worse results at high q-values than the Hosemann model. The derivations for the Hosemann model is given in Appendix B, and the result is

$$S(q) = \frac{1 - \exp(-2w^2q^2)}{1 - 2\exp(-w^2q^2)\cos(q\bar{a}) + \exp(-2w^2q^2)} \tag{2.36}$$

where $\bar{a}$ is the average separation distance between scattering objects. The

exponential function $\exp(-w^2q^2)$ within the expression for $S(q)$ is a Gaussian function where the substitution $w = \sigma/\sqrt{2}$ has been used (σ is the standard deviation for the Gaussian distribution).

2.2.3 Beaucage's unified model

The traditional Guinier and Porod plot methods are only valid for restricted parts of the q-range; the Guinier method is generally only valid for $qR_g \lesssim 1.3$ [19], and the Porod method is only valid for the high-q slope. These limitations are corrected for in the unified model which was developed by G. Beaucage and D. W. Schaefer in 1994 [35], and more detailed described by Beaucage in 1995 [37]. This approach models both Guinier exponential and structurally limited power-law regimes, *i.e.* the Porod regime, without introducing new parameters, and it is given by [37]

$$I(q) = G\exp(-q^2R_g^2/3) + B\{[\mathrm{erf}(qR_g/\sqrt{6})]^3/q\}^P. \tag{2.37}$$

R_g is the radius of gyration for the scattering particles, and $-P$ is the Porod slope. G and B is given by Eqs. (2.38) and (2.39), respectively:

$$G = N_pV_p^2\rho_e^2 = N_pn_e^2, \tag{2.38}$$

where $n_e = V_p\rho_e$ is the number of electrons in a particle.

$$B = 2\pi N_p\rho_e^2S_p, \tag{2.39}$$

where the particle's electron density is $\rho_e = n_e/V_p$ and S_p is the surface area for the particle.

For example, if particles within the sample form aggregates, the small particles within the aggregates are within one *structural level*, and the aggregates are within another structural level. The traditional methods described previously, the Guinier- and Porod approximations, only account for one structural level. On the other hand, the unified model can be extended to account for multiple structural levels, and it is therefore valid for the entire q-range. Each structural level is described by a Guinier term (Eq. (2.30)) and an associated power-law regime (Eq. (2.33)). In the extended unified model, the total intensity is the sum of the contributions from each structural level [35; 38]:

$$\begin{aligned} I(q) \quad &= \sum_{i=0}^{n-1} G_i \exp(-q^2 R_{g,i}^2/3) + B_i \exp(-q^2 R_{g,i+1}^2/3) \\ &\times \{[\mathrm{erf}(qR_{g,i}/\sqrt{6})]^3/q\}^{P_i}, \end{aligned} \tag{2.40}$$

where n is the number of structural levels included, and the lowest number for n corresponds to the largest structural level.

2.3 X-ray reflectivity theory

When X-rays hit very large objects compared to the wavelength, some of the beam gets refracted and some of it gets reflected. X-ray reflectivity (XRR) is a well established technique, and the theory derived for this technique is helpful for describing the behaviour of the principal X-ray beam as it is refracted and reflected from the sample.

The technique of *Grazing-Incidence Small-Angle X-ray Scattering* (GISAXS) is a type of SAXS experiment where the geometry is altered such that it is the part of the beam that is *reflected* from the sample that hits the detector - in other words; a SAXS experiment in reflection geometry. For this reason, it is very useful to know some of the theory of reflectivity from surfaces. Much of the GISAXS theory does indeed build on the more established XRR theory, and this is the reason for why the XRR theory necessary for understanding GISAXS will be discussed before the actual GISAXS theory.

In order to probe the surface layers of the sample, the incident angle of the X-rays needs to be very small. The GISAXS signal originates from the scattering and reflection of the X-ray beam by any type of surface roughness, scattering entity or lateral contrast variation present on the surface or buried inside a film at depths less than the penetration depth of the X-rays.

Consider first the refraction of X-rays by an interface. For finding the refracted angle for the beam entering a medium, Snell's law is used. For X-rays it is normally written as [39]

$$\cos(\alpha_t) = \frac{\cos(\alpha_i)}{n} \tag{2.41}$$

where α_t is the angle between the transmitted beam and the surface, α_i is the incident angle and n is the effective refractive index for the air-sample interface: $n = n_f/n_{air}$, where n_f is the refractive index for the film, and $n_{air} \simeq 1$. The refractive index is different for X-rays than for visible light.

2.3.1 Historical aspects

L. G. Parratt published an important paper for X-ray reflectivity in 1954, where reflection and refraction from stratified homogeneous media are discussed [40]. The refractive index for X-rays in a medium is close to, but less than 1, and it is also complex:

$$n = 1 - \delta - i\beta. \tag{2.42}$$

β is due to absorption, and it is typically in the order of $\sim 10^{-7}$ to 10^{-8}, and it is related to the linear absorption coefficient μ by

$$\beta = \frac{\lambda\mu}{4\pi}. \tag{2.43}$$

δ is the real part of the deviation from 1 of the refractive index. It is typically in the order of 10^{-6}, and it will be discussed further in Section 2.3.2. It is useful to group all the physical constants into one, and this grouping was first introduced by Parratt;

$$A' = \frac{N_A}{2\pi}\frac{e^2}{m_e c^2}. \tag{2.44}$$

The factor A' will be used again in Section 2.3.2 where δ and β are derived. In Eq. (2.44), N_A is Avogadro's number, e and m_e the electronic charge and mass, and c is the velocity of light in vacuum. Using old values for the physical constants and CGS units, Parratt obtained a value of $A' = 2.7019 \cdot 10^{10}$ [cm/g] in this paper [40], but this value has now been found to be slightly different when modern values for the physical constants and SI units were used.

Another important discovery in the history of the X-ray reflectivity technique was done by Y. Yoneda in 1963; the discovery of a so-called "anomalous surface reflection" at a very small exit angle [41]. Yoneda found that for incident angles α_i larger than the critical angle α_c the reflected power is split into two separate beams, one at the expected reflection angle $\alpha_r = \alpha_i$ (equiangular or specular reflection), and the other one at the so-called anomalous angle α_a at lower angle. O. J. Guentert investigated Yoneda's discovery more closely in 1965, and this led to an interesting paper (Ref. [42]), where it was found that $\alpha_a \simeq \alpha_c$ independent of incident angle α_i, and the reason for this will be discussed in Section 2.4.2. α_c

is the critical angle of total external reflection, and the angle α_a has since gotten the name "Yoneda angle", or α_{Yoneda}, and thus

$$\alpha_{Yoneda} \simeq \alpha_c. \tag{2.45}$$

The angle for total external reflection, α_c, is found by using Snell's law (Eq. (2.41)), approximating $\cos\alpha \simeq 1-\alpha^2/2$, and then setting β and very small cross-products equal to zero. Eq. (2.41) then becomes $\alpha_t^2 = \alpha_i^2 - 2\delta$. For total external reflection, $\alpha_t = 0$ and $\alpha_i = \alpha_c$, and consequently

$$\alpha_c = \sqrt{2\delta} \tag{2.46}$$

where δ was found to be

$$\delta = \frac{N_A e^2 \rho \lambda^2}{2\pi m_e c^2 A} f_a. \tag{2.47}$$

N_A is Avogadro's number, e and m_e the electronic charge and mass, ρ the mass density, λ the wavelength of the incident radiation, A the atomic mass, and f_a the atomic form factor for small scattering angles [42]. This result can be used for finding δ in Eq. (2.42), and the procedure for deriving this value will be described in the following section.

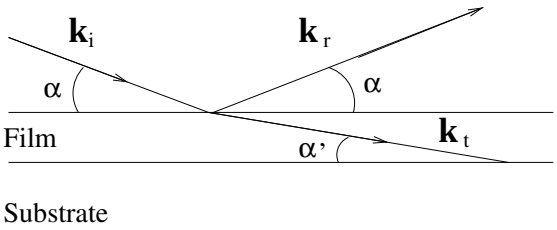

Figure 2.3: The incident beam with wave-vector $\mathbf{k}_i$ is refracted ($\mathbf{k}_t$) and reflected ($\mathbf{k}_r$) by the surface of the film. The incident and reflected angle is $\alpha_i = \alpha_r = \alpha$, and the refracted angle is $\alpha_t = \alpha'$. (The angles are exaggerated for clarity of illustration.)

2.3.2 Reflection, refraction and absorption of X-rays

2.3.2.1 Reflection and refraction

The refractive index of X-rays hitting a material depends on the parameters δ and β of the material. In this section, the procedure for finding these parameters, and consequently the refractive index, will derived.

Figure 2.3 shows an electromagnetic wave hitting an object and being reflected and refracted by the surface. The equation for the electromagnetic wave is given as

$$\mathbf{E}_j = A_j e^{i(\omega t - \mathbf{k}_j \cdot \mathbf{r})} \hat{\mathbf{e}}_y, \tag{2.48}$$

where the subscript $j = i, r, t$ corresponds to incoming wave, reflected wave and transmitted wave, respectively. The wave-vector for a scattered wave is generally denoted $\mathbf{k}_f$. Consider first the wave that is reflected specularly; its wave-vector is denoted $\mathbf{k}_r$.

Since the angle of the refracted wave is given by Snell's law, $\cos\alpha_t = \cos\alpha_i / n$

(Eq. (2.41)) where $n = n_f/n_{air}$, the next important step is to find the refractive index for the X-rays within a medium, n_f. The derivation of n_f is given below and it is partly based on Ref. [39].

The refractive index can be found by considering the classical model of a bound electron where the electron is exposed to three forces:

(i) the electric force: $\mathbf{F}_{el} = -e\mathbf{E}$ from the incident X-ray beam: $\mathbf{E} = \mathbf{E}_0 \exp(i\omega t)$

(ii) the restoring force: An electron bound harmonically to an atom will show resonance absorption at a frequency $\omega_0 = (k_F/m_e)^{1/2}$, where k_F is the force constant: $\mathbf{F}_r = -k_F\mathbf{r} = -m_e\omega_0^2\mathbf{r}$

(iii) the damping force: $\mathbf{F}_d = -\Gamma d\mathbf{r}/dt$, which is proportional to the velocity with a constant of proportionality, Γ. This force is, in this case, mostly due to the radiative loss of energy by the accelerated electrons, but also to photon absorption.

Since $\mathbf{F}_{tot} = m_e \cdot d^2\mathbf{r}/dt^2$, the equation of motion for the electron is given by

$$m_e\frac{d^2\mathbf{r}}{dt^2} + \Gamma\frac{d\mathbf{r}}{dt} + m_e\omega_0^2\mathbf{r} = -e\mathbf{E}_0 e^{i\omega t}. \tag{2.49}$$

The amplitude of this forced oscillator can be found by solving Eq. (2.49) for $\mathbf{r} = \mathbf{r}_0 e^{i\omega t}$, and first, by isolating $\mathbf{r}_0$,

$$\mathbf{r}_0 = -\frac{e\mathbf{E}_0}{m_e}\frac{1}{\left(\omega_0^2 - \omega^2 + i\frac{\Gamma}{m_e}\omega\right)}. \tag{2.50}$$

The eigenfrequency of bound electrons is in the order of 10^{15} s^{-1} ([39], p. 272), and the X-ray frequency $\omega = E/\hbar \sim 10^{18}$ s^{-1}. The damping constant is found by comparing to a classical mass-spring system, where $\Gamma/m \sim 2\omega_0$. Since $\omega \gg \omega_0$, the oscillating amplitude can be reduced to

$$\mathbf{r}_0 \simeq \frac{e\mathbf{E}_0}{m_e\omega^2}. \tag{2.51}$$

Consider next the dipole density caused by the uncoupled electrons of density ρ_e. Since the dipole moment of one electron is given by $\mathbf{p} = -e\mathbf{r}_0$, and assuming that the only contribution to the polarisation P of the medium comes from similar electrons [43], the total polarisation of the system is given by

$$\mathbf{P} = \rho_e\mathbf{p} = -\frac{\rho_e e^2\mathbf{E}_0}{m_e\omega^2}. \tag{2.52}$$

The electric displacement is given by [43]

$$\mathbf{D} = \epsilon_0\epsilon\mathbf{E}_0 = \epsilon_0\mathbf{E}_0 + \mathbf{P}, \tag{2.53}$$

and the dielectric constant for the medium is thus found to be [43]

$$\epsilon = 1 - \frac{\rho_e e^2}{m_e\omega^2\epsilon_0}. \tag{2.54}$$

The classical electron radius is given by $r_e = e^2/(4\pi\epsilon_0 m_e c^2)$, and the X-ray frequency $\omega = 2\pi c/\lambda$,

$$\epsilon = 1 - \frac{\rho_e r_e \lambda^2}{\pi}. \tag{2.55}$$

For finding the index of refraction, $n_f = \sqrt{\epsilon}$, the approximation $\sqrt{1+x} \simeq 1 + \frac{1}{2}x$ is used:

$$n_f \simeq 1 - \frac{\rho_e r_e \lambda^2}{2\pi}. \tag{2.56}$$

Using that $\rho_e = (N_A \rho f_a)/A$ where f_a is the atomic scattering factor, and that

$$A' = \frac{N_A r_e}{2\pi}, \tag{2.57}$$

where modern values from CODATA 2006 [44], and SI units, the value obtained is $A' = 2.7009 \cdot 10^{11}$ m/kg (note that this is slightly different value from Parratt's value: $A'(\text{Parratt}) = 2.7019 \cdot 10^{10}$ cm/g $= 2.7019 \cdot 10^{11}$ m/kg).

The refractive index of X-rays for a medium is then given by

$$n_f = 1 - \frac{A' \rho \lambda^2}{A} f_a. \tag{2.58}$$

Since

$$f_a = f_{a0} + f' + if'' \tag{2.59}$$

where f' and f'' are the anomalous correction factors, the refractive index becomes

$$n = 1 - \frac{A'\rho\lambda^2}{A}(f_{a0} + f') - \frac{A'\rho\lambda^2}{A}(if''). \tag{2.60}$$

From Eq. (2.42), and since $f_{a0} \simeq Z$, it is seen that δ and β can now be found by comparisons:

$$\delta = A'\rho\lambda^2\frac{Z + f'}{A} \quad \text{and} \quad \beta = A'\rho\lambda^2\frac{f''}{A}, \tag{2.61}$$

where Z and A is the atomic number and mass, respectively. For compound materials, δ and β can be estimated using [45]

$$\delta = A'\rho\lambda^2\frac{\sum_i n_i(Z_i + f_i')}{\sum_i n_i A_i} \quad \text{and} \quad \beta = A'\rho\lambda^2\frac{\sum_i n_i f_i''}{\sum_i n_i A_i}. \tag{2.62}$$

where n_i is the relative molar content of each constituent element.

In summary, for calculating the refracted angle within a film, first Eq. (2.62) is used for calculating δ and β, and the resulting values are then used in Eq. (2.42) for finding the refractive index n_f. Now the refracted angle α_t can be calculated using Snell's law, Eq. (2.41). The physical meaning of β will also be investigated in this section.

2.3.2.2 Absorption

As was briefly mentioned in Section 2.3.1, the parameter β is due to absorption of the X-rays within the sample. This absorption happens because the sample material attenuates the X-rays. In this section, the equations governing the absorption

are derived, and the concept of *penetration depth* of X-rays is introduced.

From Eq. (2.48), the equation for the refracted wave is given as

$$\mathbf{E}_t = A_t e^{i(\omega t - \mathbf{k}_t \cdot \mathbf{r})} \hat{\mathbf{e}}_y, \tag{2.63}$$

where

$$\mathbf{k}_t = nk \begin{bmatrix} \cos\alpha_t \\ \\ \sin\alpha_t \end{bmatrix} \qquad \text{and} \qquad \mathbf{r} = \begin{bmatrix} x \\ \\ -z. \end{bmatrix} \tag{2.64}$$

Writing out the dot product in Eq. (2.63), the transmitted wave becomes

$$E_t = A_t e^{i(\omega t - nk\cos\alpha_t x + nk\sin\alpha_t z))}. \tag{2.65}$$

In order to simplify the second term within the parenthesis, Snell's law is used; $n\cos\alpha_t = \cos\alpha_i$. Additionally, using the small-angle approximation ($\sin\alpha_t \simeq \alpha_t$) in the third term, the transmitted wave is now given by

$$E_t = A_t e^{i(\omega t - k\cos\alpha_i x + nk\alpha_t z)}. \tag{2.66}$$

The absorption is governed by the real part of $e^{ink\alpha_t z}$, and since $n\alpha_t$ is complex, it can be written as $n\alpha_t = a + ib$. Since $\alpha_t \approx \sin\alpha_t \approx k_{t,z}/k_t$ and $k_t = nk = (2\pi n)/\lambda$, we see that

$$n\alpha_t \approx \frac{\lambda}{2\pi} k_{t,z}. \tag{2.67}$$

Therefore,

$$a(\alpha) = \frac{\lambda}{2\pi}\Re(k_{t,z}) \quad \text{and} \quad b(\alpha) = \frac{\lambda}{2\pi}\Im(k_{t,z}). \tag{2.68}$$

It follows that the electric field is given by

$$E_t = A_t e^{i(\omega t - k\cos\alpha_i x + k(a+ib)z)} \tag{2.69}$$

$$= A_t e^{i(\omega t - k\cos\alpha_i x + kaz)} e^{-kbz}. \tag{2.70}$$

By taking the modulus squared of this electric field, the variation of the intensity $I(z)$ with depth into the material is given by

$$I(z) = E_t E_t^* \propto e^{-2kbz}. \tag{2.71}$$

The penetration depth Λ is defined as the depth where the intensity has fallen to $1/e$: $I(\Lambda) = I(0)/e$. Setting in for $z = \Lambda$ and $z = 0$; $I(\Lambda) = e^{-2kb\Lambda}$ and $I(0) = 1$, respectively. Now the penetration depth is found as

$$\Lambda = \frac{\lambda}{4\pi b(\alpha)} = \frac{1}{2\Im(k_{t,z})}. \tag{2.72}$$

Since $\alpha_t \simeq k_{t,z}/k_t = (\lambda k_{t,z})/(2\pi n)$, we get that $k_{t,z} = (2\pi n\alpha_t)/\lambda$. Because $n \approx 1$, we find that the penetration depth of the X-rays, Λ, can be approximated by

$$\Lambda \simeq \frac{\lambda}{4\pi\Im(\alpha_t)}. \tag{2.73}$$

In the proceeding sections, two different expressions for β have been shown; $\beta = (\lambda\mu)/(4\pi)$ (Eq. (2.43)), and $\beta = A'\rho\lambda^2(f''/A)$ (Eq. (2.61b)). The derivation of the latter was just shown in Section 2.3.2, and the derivation of the first is as follows: Consider the transmitted wave in Eq. (2.63). For a wave normal to the surface, the dot product becomes $\mathbf{k}_t \cdot \mathbf{r} = nkr_z$. This wave can now be described by

$$E_t = A_t e^{i(\omega t - nkr_z)}, \tag{2.74}$$

and therefore; $e^{-inkr_z} = e^{-i(1-\delta)kr_z} \cdot e^{-\beta kr_z}$, where the first factor is the phase factor and the second factor the amplitude factor. Since the amplitude attenuation of the wave behaves as $e^{-\mu z/2}$, by comparison it is found that $\beta k = \mu/2$, and therefore, by setting in for the wave-vector $k = 2\pi/\lambda$,

$$\beta = \frac{\lambda\mu}{4\pi} \tag{2.75}$$

which is indeed equal to Parratt's expression for β (Eq. (2.43) in [40]). This expression was commonly used in literature (see, for example, [46; 47; 48]), and it is useful when the linear absorption coefficient μ for the relevant material is known. On the other hand, if the anomalous correction factors (f' and f'') are known, for consistency it is better to use Eqs. (2.61) or (2.62) for calculating both

δ and β.

2.4 GISAXS

In 1979, Marra, Eisenberger and Cho proposed a new technique utilising X-ray diffraction in conjunction with total external reflection for studying ordered interfaces and surface phenomena [49]. This experiment can be considered as a precursor experiment for GISAXS. The first GISAXS experiment was performed as a *Ph.D.* project by Joanna Levine, and the first paper was published in 1989: "Grazing-Incidence Small-Angle X-Ray-Scattering - New Tool For Studying Thin-Film Growth" [31].

Grazing-Incidence Small-Angle X-ray Scattering (GISAXS) is a surface sensitive, non-destructive technique that is often used for the characterisation of micro- and nano-scale density correlations and shape analysis of objects at surfaces or at buried interfaces for various classes of materials such as ceramics, metals, semiconductors, polymers and soft matter. In the extreme case of a (theoretically) perfectly flat and featureless surface, all the incoming intensity is specularly reflected fulfilling the law of reflection from optics, $\alpha_i = \alpha_f$. In such case, the GISAXS experiment would not probe anything, and the two-dimensional detector image would only show the specular peak. The diffuse or off-specular scattering appears when any type of surface roughness, scattering entity or lateral contrast variation is present on the surface or inside a film. [50]

Since GISAXS is a reciprocal space technique, it has the advantage that there is

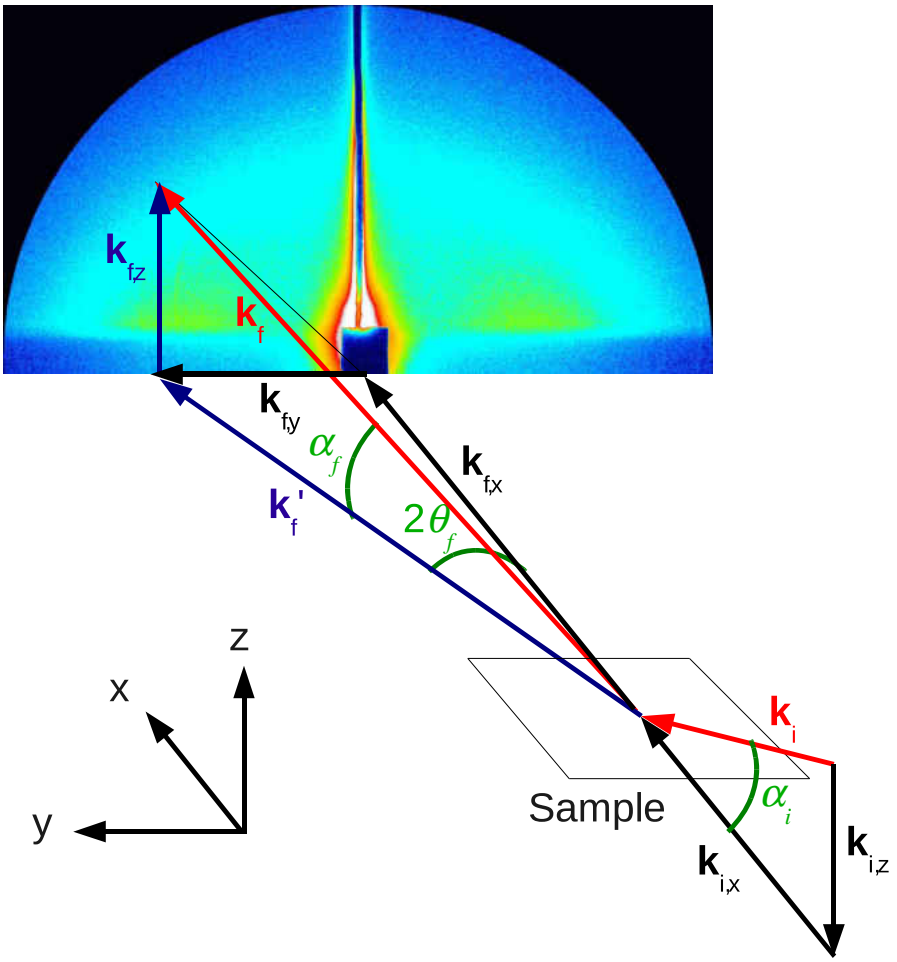

Figure 2.4: The principle of the GISAXS technique. The monochromatic X-ray beam hits the sample at an angle α_i relative to the sample plane. The beam is then reflected and scattered from the surface of the sample, and the direction of the scattered beam is described by α_f and $2\theta_f$.

a large number of scattering particles that contributes to the signal, and therefore better statistics are obtained than real space techniques can typically achieve.

A typical GISAXS experiment is illustrated in figure 2.4. The incoming beam is described by the wave-vector $\mathbf{k}_i$ at an angle α_i between it and the sample plane. The X-rays are scattered along $\mathbf{k}_f$ in the direction described by the angles $(2\theta_f, \alpha_f)$.

As already mentioned, the wave-vector transfer $\mathbf{q}$ is given by the difference

between the outgoing and the incoming wave-vectors. The wave-vector for the outgoing wave, $\mathbf{k}_f$, is found by evaluating the sines and cosines for the angles $2\theta_f$ and α_f, and similarly, the wave-vector for the incoming wave, $\mathbf{k}_i$, is found by the evaluation of the sine and cosine of α_i:

$$\mathbf{k}_i = k \begin{bmatrix} \cos(\alpha_i) \\ 0 \\ -\sin(\alpha_i) \end{bmatrix} \quad \text{and} \quad \mathbf{k}_f = k \begin{bmatrix} \cos(\alpha_f)\cos(2\theta_f) \\ \cos(\alpha_f)\sin(2\theta_f) \\ \sin(\alpha_f) \end{bmatrix}. \tag{2.76}$$

Since both of these waves propagate in air, the absolute value of the wave-vector is the same in both cases, and it has therefore been used that $|\mathbf{k}_i| = |\mathbf{k}_f| = k$. By adding up the vectors and setting $k = (2\pi)/\lambda$, the wave-vector transfer vector is obtained as

$$\mathbf{q} = \mathbf{k}_f - \mathbf{k}_i = \frac{2\pi}{\lambda} \begin{bmatrix} \cos(\alpha_f)\cos(2\theta_f) - \cos(\alpha_i) \\ \cos(\alpha_f)\sin(2\theta_f) \\ \sin(\alpha_f) + \sin(\alpha_i) \end{bmatrix}. \tag{2.77}$$

By evaluating Eq. 2.77 for small and constant α_f and $2\theta_f$, we see that the following approximation is valid:

$$q_y \approx \frac{4\pi}{\lambda}\sin(\theta_f), \tag{2.78}$$

which is recognised as the equation for the magnitude of the wave-vector trans-

fer vector, q, for small-angle scattering in transmission setup (see, for example, [31]). In the measured GISAXS patterns, then, the cuts taken parallel to the sample surface (in the y-direction in figure 2.4) can be treated as conventional SAXS patterns. However, using this procedure, only information about the horizontal direction in the sample can be obtained, and no conclusion on structures along the surface normal can be found.

2.4.1 Estimating optimal angles

As shown in Eqs. (2.73) and (2.41), the penetration depth of the probing X-ray beam depends on the incident angle, and thus the smaller the incident angle, the more surface sensitive the measurements are. Therefore, before starting a GISAXS experiment, it is important to know which probing depth is most important to the specific experiment and decide the incident angle accordingly. In order to calculate the best possible angle for the incident beam at a GISAXS experiment, it is useful to consider the *Fresnel reflectivity and transmittivity*. The reflected amplitude coefficient r for X-rays hitting a medium at small angles is given by [51]

$$r = \frac{A_r}{A_i} \simeq \frac{\alpha_i - \alpha_t}{\alpha_i + \alpha_t}, \tag{2.79}$$

where A_r and A_i is the amplitude of the reflected beam and the incoming beam respectively, and similarly, the transmitted amplitude coefficient is

$$t = \frac{A_t}{A_i} \simeq \frac{2\alpha_i}{\alpha_i + \alpha_t}, \tag{2.80}$$

where A_t is the amplitude of the refracted beam. The intensity reflectivity is given by

$$\mathcal{R}(\alpha) = rr^*. \tag{2.81}$$

In this case the transmitted intensities are not complementary to the reflected ones because the intensity is defined as the energy crossing unit area per second, and the cross-sectional area of the refracted beam is different from that of the incident beam [52].

The amplitude transmittivity is given by [51; 52; 53]

$$t = 1 + r, \tag{2.82}$$

and consequently, the intensity transmittivity:

$$\mathcal{T}(\alpha) = tt^*. \tag{2.83}$$

Figure 2.5 shows the theoretical intensity reflectivity and transmittivity for clean silicon and for a yttria-zirconia coating containing 4.17 mol% yttria, heated to 1000 °C, plotted for different incident angles. In order to improve the signal-to-noise ratio in a GISAXS experiment, a large value of $\mathcal{R}$ is desirable. From this figure it is seen that the optimal incident angle for an experiment is around the

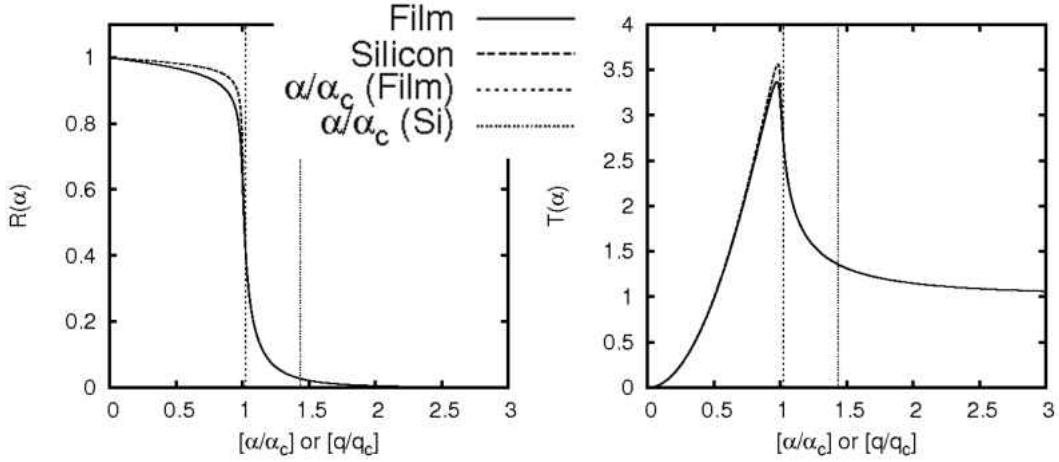

Figure 2.5: The theoretical intensity reflectivity (left panel) and transmittivity (right panel) calculated for clean silicon (dashed line) and for a ZrO_2-Y_2O_3 (4.17 mol% yttria) film heated to 1000 °C (full line) as function of incident angle. The two vertical lines indicate (from left to right) the incident angle used in our experiments divided by the critical angle for the film, and the incident angle divided by the critical angle for silicon, respectively.

critical angle. For $\alpha_i \approx \alpha_c$, information can be obtained only for the surface of the material. For the study of a film, we want some of the beam to penetrate the film; this happens when $\alpha_i > \alpha_c$. For $\alpha_i > 1.5 \cdot \alpha_c$, the beam hitting the detector has almost entirely been transmitted through the film, whilst for $\alpha_c < \alpha_i < 1.5 \cdot \alpha_c$, the signal hitting the detector is a combination of the initial reflection and transmission through the film.

2.4.2 Extra intensity at the critical angle; The Yoneda feature

In a GISAXS pattern, as for example the one illustrated in figure 2.4, the brightest line in the y-direction is situated at a certain exit angle, which has been found to be the critical angle of total external reflection, α_c. This feature is called the

Yoneda peak or *feature* after Y. Yoneda who was the person that first discovered this effect. However, Yoneda just discovered this effect; it was explained later, most famously by Vineyard [46] in 1982, and Sinha, Sirota and Garoff [54] in 1988. The angle of the Yoneda feature, *i.e.* the critical angle, is practically independent of the incident angle (Eq. (2.46)), and the physical origin for the Yoneda feature will be discussed in this section.

One of the best explanations so far is given by Renaud, Lazzari and Leroy in a review article from 2009 [39], where it is explained that it is necessary to use the appropriate model when the incident angle is small ($\alpha_i \approx \alpha_c$); the framework for this model is called *distorted wave Born approximation* (DWBA). Within DWBA, it is necessary to consider four different scattering events, as illustrated in figure 2.6, instead of just one - as was used in the simpler *Born Approximation* (BA), which is valid for larger incident angles ($\alpha_i \gg \alpha_c$). The Yoneda feature is found to be due to the interference effects between the four beams that are scattered from each irregularity or object on the sample surface (see figure 2.6). This is because at very small incident angles, in addition to a normal scattering event, there are the possibilities of first a reflection followed by scattering, or a reflection after the scattering, or reflection followed by scattering and a second reflection [50]. It is thus clear that the Yoneda peak only can be observed for surfaces having some degree of roughness; from a perfectly flat surface, only the specular reflected beam will be observed.

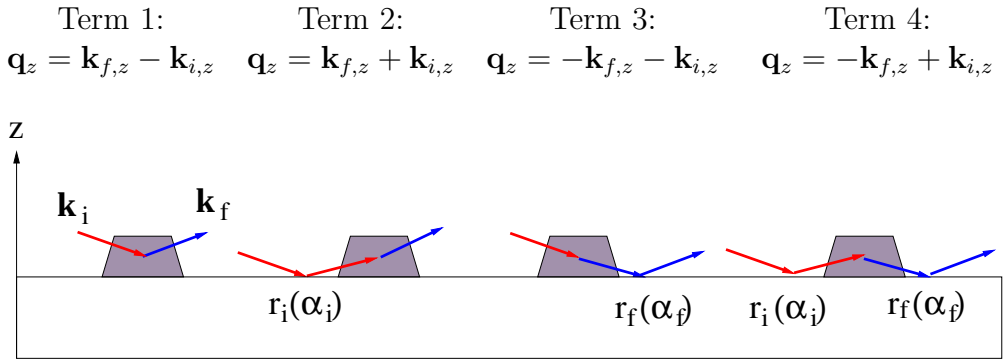

Figure 2.6: Diagram of interactions (not a geometrical representation) of the island scattering cross section in DWBA. Based on ([39], figure 41) and [55].

More accurately, the Yoneda peak was found to be due to:

(i) the sharp variation of the reflectivity $\mathcal{R}$ and of the phase shift of the reflected beam, close to the critical angle (see figure 2.5 (left panel) and ([39], figure 25)).

(ii) the involved Fourier transforms $\mathcal{F}(\mathbf{q}_\parallel, \pm k_{i,z}, \pm k_{f,z})$, where $\mathbf{q}_\parallel$ is the components of $\mathbf{q}$ parallel to the sample surface (*i.e.* $\mathbf{q}_\parallel = \mathbf{q}_x + \mathbf{q}_y$).

The differential cross-section of the scattering event is given in ([39], Eqs. (133-135)), where it is shown how $\mathcal{F}(\mathbf{q}_\parallel, \pm k_{i,z}, \pm k_{f,z})$ is built up of four terms, each term representing one of the different scattering events illustrated in figure 2.6:

$$\frac{\mathrm{d}\sigma}{\mathrm{d}\Omega} \propto |F(\mathbf{q}_\parallel, k_{f,z} - k_{i,z}) + r_i(\alpha_i)F(\mathbf{q}_\parallel, k_{f,z} + k_{i,z}) + r_f(\alpha_f)F(\mathbf{q}_\parallel, -k_{f,z} - k_{i,z}) + r_i(\alpha_i)r_f(\alpha_f)F(\mathbf{q}_\parallel, -k_{f,z} + k_{i,z})|^2 \qquad (2.84)$$

The patterns simulated using BA and DWBA were plotted in ([39], figure 42),

and from this figure it is observed that there is a peak at α_c when DWBA was used, but not when BA was used.

2.5 X-ray diffraction

As mentioned in Section 1.1.2, zirconia exists in three different phases; monoclinic, tetragonal and cubic. X-ray diffraction (XRD) is used to determine the phase of the YSZ samples and possible phase transitions; the relevant theory behind these investigations will be given in this section.

The reason why XRD is so useful for finding the crystal structure is, as briefly mentioned in Section 2.1, the Bragg reflections from the lattice planes. However, many types of crystal structures exist because there are 14 unique Bravais lattices (which describe the translational symmetry of the crystals) and 230 different space groups.

If the space group and the locations of the atoms within the unit cell are known, the angular positions of the Bragg peaks are known exactly. This makes it possible to distinguish different phases of the crystalline particles within the sample, by simulating the peak positions for the relevant phases, starting by using Bragg's law:

$$n\lambda = 2d \sin \theta_B. \qquad \text{(Eq. (2.1))}$$

For a specific reflection denoted by hkl,

$$\lambda = 2d_{hkl} \sin \theta_B. \tag{2.85}$$

The 100, 010 and 001 reflections can now easily be calculated for a cubic crystal, since $d_{100} = d_{010} = d_{001} = a$. The Bragg angle for a cubic crystal can thus be found by rearranging the equation above, which gives

$$2\theta_B = 2 \sin^{-1} \left(\frac{\lambda}{2a} \right). \tag{2.86}$$

Consequently, finding the position of the the Bragg angle is trivial as long as d_{hkl} is known. For example, for a cubic crystal, the d-spacing can be calculated by using ([56], page 21)

$$\frac{1}{d_{hkl}^2} = \frac{h^2 + k^2 + l^2}{a^2}. \tag{2.87}$$

From this equation it is observed that for the 100, 010 and 001 reflections, d_{hkl} becomes equal to a, as expected.

A method of calculating the q-value of the Bragg peaks can be found by combining Bragg's law (Eq. (2.1)) and the equation for finding q (Eq. (2.5)):

$$q = \frac{2\pi n}{d}. \tag{2.88}$$

When the position of the Bragg peak is known in q-space, and the wavelength is known, $2\theta_B$ can easily be calculated by using

$$2\theta_B = 2\sin^{-1}\left(\frac{q\lambda}{4\pi}\right). \tag{2.89}$$

Simplified example: Zr metal in a fcc lattice. In addition to being a simpler system than the ZrO_2-system in the space group $Fm\bar{3}m$, this is also a rather realistic example because as shown in figure 1.1, the simple cubic oxygen sublattice has a lattice parameter half of that of the zirconium fcc lattice. This means that, for example, the 200 reflection from the oxygen sublattice will end up having the same Bragg angle as a 100 reflection from the Zr fcc lattice. In this example, a lattice parameter was set to $a = 5.135$ Å because of previous results in other works, see for example [8].

a) For the 100, 010 or 001 reflections, $d_{100} = d_{010} = d_{001} = a$ and thus $q = (2\pi)/(5.135\text{ Å}) = 1.2236\text{ Å}^{-1}$. Consequently, for CuK$\alpha_1$ radiation ($\lambda = 1.5406$ Å), these reflections are all found at $2\theta_B = 17.25°$.

b) For the 111 reflection, $d_{111} = a/\sqrt{3} = 2.9647$ Å, and consequently, $q = 2.1193$ Å^{-1}. For CuKα_1 radiation, $2\theta_B = 31.12°$.

Following this pattern for different combinations of hkl makes it possible to calculate the position of all the Bragg peaks. However, the reality is not quite that simple - the *structure factor* F_{hkl} also needs to be considered.

2.5.1 Structure factor for a Bragg reflection

A discussion on the height and width of the Bragg peaks is also necessary. This is because in a "perfect measurement" of a large perfect crystal the peak width of the Bragg peak goes to zero whilst the amplitude goes to infinity. However, effects such as divergence of the X-ray beam causes the Bragg peak to become wider. The width of the Bragg peak is also related to the size of the crystals within the sample; larger crystals cause narrower Bragg peaks. In reality, therefore, the peaks are having a finite width, and consequently, the peak amplitudes are not infinite any longer. Now the intensity (*i.e.* the area under the curve) of the Bragg peaks are found to be proportional to the square of the structure factor F_{hkl} (see for example [51], page 144) [1]; $I(q) \propto |F_{hkl}|^2$. The structure factor is given by ([56], page 28 and 31)

$$F_{hkl} = \sum_n f_n e^{i\mathbf{q}\cdot\mathbf{r}_n} = \sum_n f_n e^{2\pi i(hx_n+ky_n+lz_n)} \tag{2.90}$$

where $\mathbf{r}_n = x_n\mathbf{a}_1 + y_n\mathbf{a}_2 + z_n\mathbf{a}_3$ is the basis vector. In Eq. (2.90), the first factor within the sum is the amplitude factor and the second factor is the phase, which is 0 or 1 depending on whether Bragg's law (Eq. (2.1)) is satisfied for this set of planes.

The derivation of F_{hkl} for a fcc crystal is given elsewhere ([56], p. 32), and is therefore not repeated here. Remember that if m is and integer, $e^{\pi i m} = (-1)^m$. We thus find that if hkl are all odd or all even, we get

[1] In XRD terminology, it is normal to use the letter F for denoting *structure factor*.

$$F_{hkl} = 4 \sum_{n/4} f_n e^{2\pi i(hx_n + ky_n + lz_n)} \tag{2.91}$$

and if hkl contain some odd and some even numbers, the structure factor becomes

$$F_{hkl} = 0. \tag{2.92}$$

This means that in an XRD pattern from a fcc crystal, all the reflections with mixed (*i.e.* both odd and even) indices are missing; these peaks are *systematic absent*.

By taking the complex conjugate of F_{hkl}, and for the case where all the atoms are identical such that $f_n = f_a$ for all the atoms in the crystal, we see that $F^*_{hkl} F_{hkl} = 4^2 f_a^2$. Recall that $f_a = f_{a0} + f' + if''$. This means that far from the absorption edges, $f_a \simeq f_{a0}$, where $f_{a0} \simeq Z$ ([56], p. 10). From this we see that if hkl are all odd or all even, $|F_{hkl}|^2 \approx 16 \cdot Z^2$. Table 2.1 shows an example on how different combinations of hkl, the calculated values for the Bragg reflections (q and/or 2θ) and $|F_{hkl}|^2$ can be tabulated. The process of filling in this type of table can of course be simplified by using a computer program, and this will be discussed in Section 6.3.

Reflection (hkl)	q [Å^{-1}]	2θ [°]	$\lvert F_{hkl}\rvert^2$
(100),(010),(111)	1.224	17.25	0
(111)	2.119	30.12	27906
etc.	...	...	...

Table 2.1: Calculating the possible reflections from Zr arranged in an fcc lattice.

Summary

In order to understand the GISAXS patterns, it is necessary to understand the physics of the X-ray beam from the time it hits the material, until it hits the detector. The behaviour of the principal X-ray beam is well-known from mature techniques such as X-ray reflectivity (XRR), and the scattering of the X-ray beam can be explained by small-angle scattering techniques for the energy- and angular ranges considered in our experiments.

The GISAXS signal originates from the scattering and reflection of the X-ray beam falling in at grazing angles by any type of surface roughness, scattering entity or lateral contrast variation present on the surface or buried inside a film at depths less than the penetration depth of the X-rays.

The scattered waves undergo distortion in the vertical direction due to refraction; however, refraction effects are negligible in the horizontal direction. By making cuts in the GISAXS pattern in the direction parallel to the sample at the critical angle, 1D-SAXS patterns can be obtained, which give information about the sample in the direction parallel to the surface, such as size of-, surface structure of- and average separation distance between scattering objects, without having to take refraction effects into account.

Chapter 3

Experimental methods

3.1 Introduction

Several methods for synthesising YSZ have previously been demonstrated [16; 57]. In this work the sol-gel method is used since this method offers the opportunity to produce a wide range of YSZ-based glasses and ceramics, as well as dip-coated substrates and YSZ ceramic fibers [14].

This chapter explains how our samples, *i.e.*, the ZrO_2-Y_2O_3 coated substrates, were prepared, and it also includes a description of the relevant X-ray scattering experimental set-ups.

3.2 Sample production

The samples were produced by first making a suitable sol, then applying it to the substrate by dip-coating, and then drying the coated layer. The details of the sol

production and dip-coating will be described in Section 3.2.2 and Section 3.2.3, respectively.

3.2.1 Substrate

3.2.1.1 Mica

For the SAXS experiment, substrates transparent to X-rays are needed, and mica was therefore chosen. Pieces of mica were bought from Rapid Electronics [58], and cut in two pieces of $\sim (25 \times 10)$ mm each.

3.2.1.2 Silicon

For the GISAXS experiments, silicon wafers (Si(100)) were used as substrates because they are flat enough for reflecting X-rays, and they can be heated to > 1000 °C without melting, although oxidation will occur. The wafers were cut into rectangles of $\sim (25 \times 10)$ mm before coating.

3.2.2 Coatings used as samples

Different doping levels of yttrium-to-zirconium was prepared by adding different amounts of yttrium nitrate corresponding to 2.04, 4.17, 8.70 and 19.1 mol% Y_2O_3; these samples are listed in Table 3.1. Table 3.2 shows which sol-recipes were used at which experiment.

The zirconia sols used for the SAXS and GISAXS experiments were prepared by mixing 10 ml zirconium(IV)propoxide ($Zr(OCH_2CH_2CH_3)_4$) (Sigma-Aldrich,

Sample name	n_{Zr} [mol]	n_Y [mol]	n_O [mol]	$\frac{n_{Y_2O_3}}{n_{Y_2O_3}+n_{ZrO_2}}$ [mol%]
Zr-Y-A	0.322	0.013	0.664	2.04
Zr-Y-B	0.311	0.027	0.662	4.17
Zr-Y-C	0.288	0.055	0.658	8.70
Zr-Y-D	0.239	0.113	0.648	19.1

Table 3.1: Relative molar content ($n_{Zr} + n_Y + n_O = 1$) of the different coatings, which are generally referred to as the "Zr-Y coatings".

Technique	*Coatings*	*Substrate*	*X-ray Energy* [eV]	*Heating* [°C]
SAXS	ZrO_2	mica	8000	*in situ*
	ZrO_2, A, B,Y_2O_3	mica	17800* & 16800	500
	ZrO_2, B,Y_2O_3	mica	17800* & 16800	700
XRD	ZrO_2	mica	8048	500, 700
GISAXS	A, B, D	Si(100)	10008	*in situ*
	ZrO_2 (4 layers)	Si(100)	10008	500
	ZrO_2	Si(100)	10000	*in situ*
XRD	ZrO_2	Si(100)	8048	500, 700, 900
XRD	A	Si(100)	8048	500, 700, 900
XRD	C	Si(100)	8048	500, 700, 900
XRD	D	Si(100)	8048	500, 700

Table 3.2: Overview of samples and techniques used. (*) The sample not containing any yttrium (*i.e.* the zirconia coating) was measured on using the indicated energy.

70 wt.% in 1-propanol), 10 ml isopropanol ($(CH_3)_2CHOH$), 2.5 ml acetylacetone ($CH_3COCH_2COCH_3$) and $\sim$ 0.5 ml acetic acid (CH_3COOH), and adding 5 ml isopropanol+water mixture (volume ratio 2:1). Yttria doping was obtained by crunching the grains of yttrium nitrate hexahydrate ($Y(NO_3)_3 \cdot 6H_2O$) (Sigma-Aldrich, 99.8% trace metals basis) by pestle and mortar and adding it to the isopropanol+water solution before it was mixed with the other solution. Different amounts of yttrium nitrate was used for different samples: 0.356, 0.743, 1.628 and 4.024 g for coating recipe A, B, C and D, respectively. The yttrium nitrate did

Figure 3.1: Samples were produced by dip-coating the substrate into the relevant sol, and this photo shows some of these sols. Left to right: zirconia containing yttria nanoparticles (not used), 2.04 mol% yttria (recipe A), 4.17 mol% (recipe B), 19.1 mol% (recipe D), and yttrium nitrate dissolved in water. Photo: Matt Gunn.

dissolve in the isopropanol+water solution, but stirring using a magnetic stirrer for some time was necessary. Eventually, after mixing all the ingredients and stirring, a clear sol was obtained from each of the recipes used; some of these are shown in Figure 3.1.

The water in the yttrium nitrate ($6 \cdot H_2O$) has not been taken into account when the water content was calculated simply because the exact amount of water is not critical in the case where the sol does not need to undergo bulk gelation - which is the case for the sols used for dip-coating. This is because when the film becomes thinner, the inorganic species are progressively concentrated, leading to aggregation, gelation, and final drying to form a type of a dry gel [59].

3.2.3 Dip-coating

Dip-coating is a controlled way of producing flat thin films from sols made by sol-gel technique. The thickness of the film can be controlled by varying the withdrawal velocity, the viscosity or the density of the sol [60].

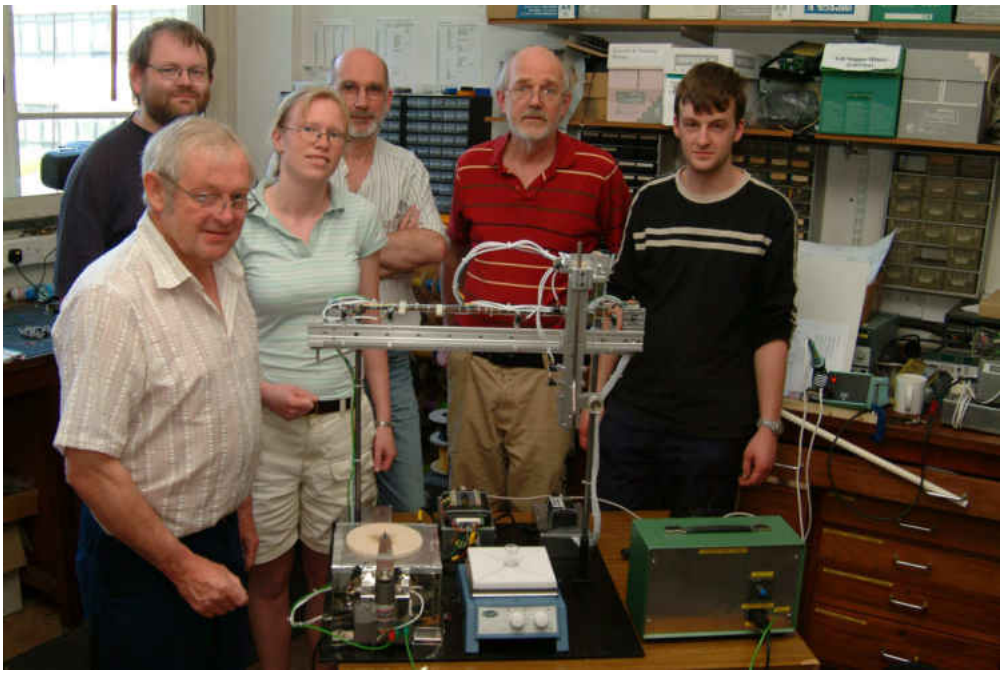

Figure 3.2: Most of the proud construction team test-running the dip-coating machine before departure to Daresbury. Front row: Dave Francis. Back row, from left to right: Rudi Winter, Kristin Høydalsvik, Clive Willson, Les Dean and Matt Gunn. Photo: Steve Fearn.

3.2.3.1 The dip-coating machine

A dip-coating machine were designed and build in the home institute, and it is shown in the figures 3.2 and 3.3.

The design of the dip-coater was developed together with Matt Gunn. Dave Francis and John Parry in the mechanical workshop built the machine after Gunn's drawings. The electronics was designed and developed by Les Dean and Dave Lewis. Matt Gunn also constructed the furnace (to the left hand side of the board in figure 3.2). The green box on the right hand side of the machine, is the control box to the furnace. The machine was run using LabVIEW, and the necessary routines were written by Clive Willson.

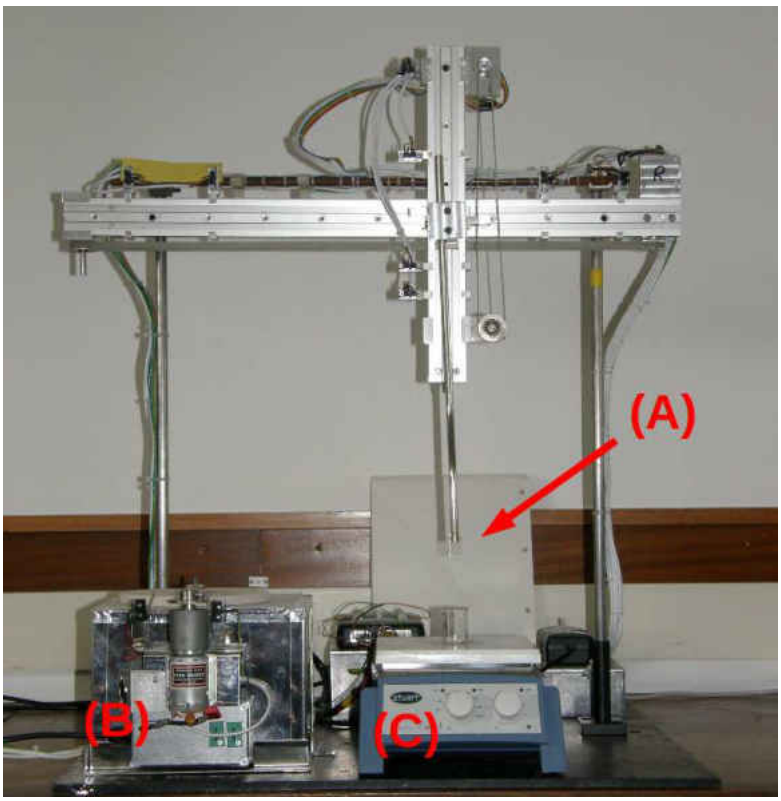

Figure 3.3: The dip-coating machine. The sample is attached to the rod (A). The box at (B) is the casing for a tube furnace, with a lid that moves when the sample is lowered down towards it. The beaker that contains the sol is situated on top of a hotplate which is labelled (C); this was cold during the dip-coating of these samples. In the back there are boxes for electronics, and USB cable to the computer (not shown). Photo: Richard Fallows.

The substrate is mounted on the end a metal rod. This was done by clamping the substrate between the rod and a metal piece, and tightened by using a screw. In figure 3.3, the substrate is placed in the measurement position (A), which is the position used whilst SAXS measurements are performed. The time at which the substrate remains in this position can be set in the software. When the machine is used for dip-coating samples, and not SAXS measurements, it is practical to set this time to zero. Next, the vertical movement downwards starts, and it stops when the substrate is well within the sol. Then the upwards motion starts, slowly and steadily as the withdrawal of the substrate from the liquid takes place. The velocity of the withdrawal is set in the software by adjusting the "withdrawal rate". After the dip-coated sample is well clear of the liquid, the velocity of the vertical motion is increased and then kept constant until the sample reaches the measurement position where it is kept for the amount of time set in the software. Now, if the furnace is excluded, downwards motion takes over, and so the cycle continues. On the other hand, if the furnace is included, the sample is now moved horizontally until it is above the furnace. Then the furnace lid opens, and the sample is moved down into the furnace where it remains for the amount of time which is set in the software. Then the sample is moved up again, the lid closes, and the sample is moved horizontally until it is above the beaker - and so the cycle continues.

The tube furnace within its box is shown in figure 3.3, labelled (B). A motor moves the lid on and off the opening of the furnace. Limit switches ensure that

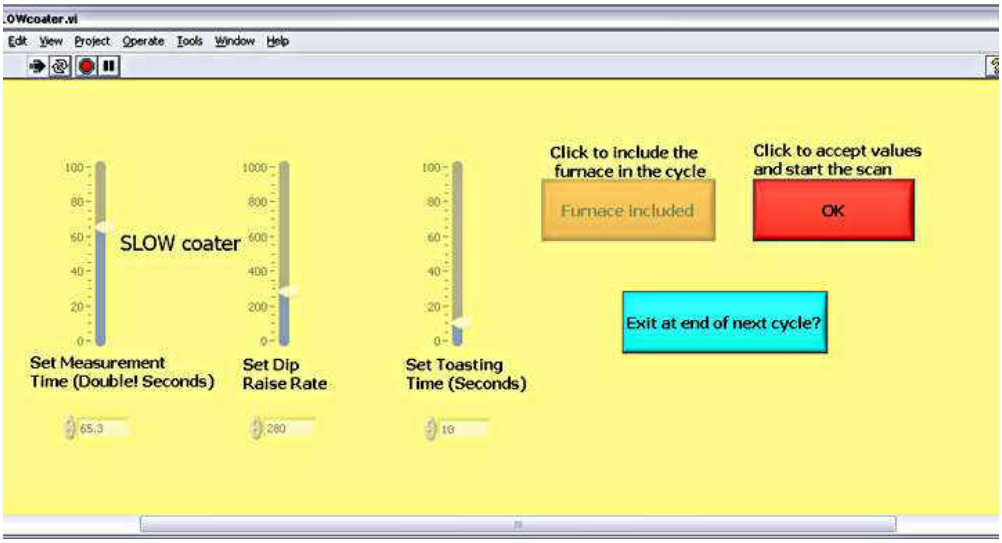

Figure 3.4: A screenshot of the LabVIEW control program. Bars on the left hand side of the screen: for adjusting relevant parameters (time in measurement position, rate of withdrawal and the time that the sample spends in the furnace). Buttons on the right hand side of the screen: selecting to include or exclude the furnace in the cycles (orange), saving values and getting ready to start the cycles (red), and start/stop (turquoise).

the furnace lid is only in the open position while the sample is actually inserted.

The hotplate underneath the beaker (labelled (C) in figure 3.3) was included in the design in case there is a need for warming the sol, but for the yttria-zirconia sols this was not necessary, and the hotplate is simply there in order to place the beaker in the correct height relative to the movement of the substrate.

The motors in the dip-coating machine are operated remotely by a LabVIEW control routine. A screenshot of this routine running is shown in figure 3.4. From the bars to the left side, different parameters can be adjusted, and the buttons to the right control the running of the machine.

The substrate is dipped into the relevant sol that is contained in a small beaker, and then withdrawn with constant speed (in all our experiments, this speed was

set to 8.1 cm/min $\approx$ 1.35 mm/s). After dip-coating the sample, it may be put down into the furnace next to it, and annealed at a set temperature between 300 °C and 700 °C. However, the samples for the GISAXS experiments were dried at 120 °C for $\sim$ 10 minutes in a separate furnace.

3.2.3.2 Dip-coating velocity

This section describes how the withdrawal velocity for the dip-coating was estimated. The thickness of the coating depends on, amongst other factors, the velocity of withdrawal. These velocities were measured using a stop watch and ruler, and the measurements were performed in a room with a stable temperature of 17 °C. The distance for the withdrawal motion was measured to be $s = (30 \pm 0.5)$ mm. Figure 3.5 shows the measured time during withdrawal as a function of number of cycles.

In the LabVIEW control program the rate for the withdrawal velocity was set to the same value for all the samples prepared. Using the measurements above,

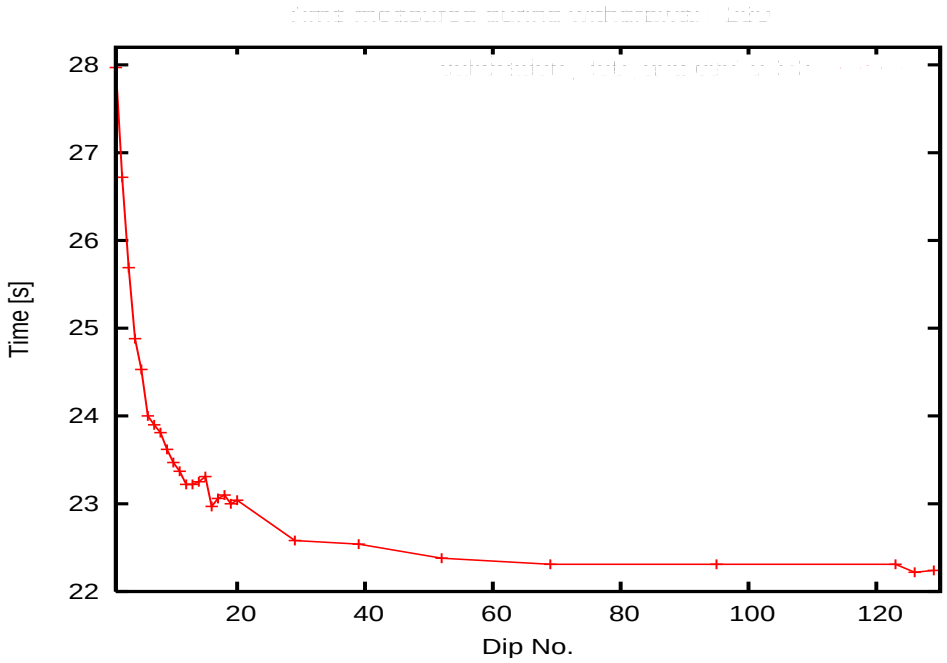

Figure 3.5: Time measured during withdrawal as function of dipping cycles for the dip-coating machine.

after the warm-up time the withdrawal velocity was found to be $v_{ws} = (1.35 \pm 0.03)$ mm/s.

The withdrawal velocity was found to be stable after a warm-up-time of 50 cycles. Consequently, it was found that for the withdrawal velocity rate used here, it was necessary to run the machine doing dipping cycles for approximately 50 minutes before the dip-coating can start in order to make the coatings as similar as possible. Doing this, the withdrawal velocity should be constant for the rest of the dips.

Synchrotron	*Beamline*	*D* [mm]	*X-ray energy* [eV]
BESSY II, Germany	7T-MPW-SAXS	3345	8000
Daresbury Laboratory, UK	6.2	3750	16800 & 17800

Table 3.3: Overview of the different SAXS measurements performed. *D* is the sample-detector distance. The BESSY II facility is hereafter called "Bessy".

3.3 Measurements

3.3.1 SAXS

A preliminary experiment for investigating the *in situ* heating behaviour of zirconia-coated mica was performed at Bessy and usable results were obtained (see Section 5.2.1 and Section 6.5.1). Further experiments for studying the changes in SAXS patterns in between dipping- and heating cycles were conducted at Daresbury some time later. The experimental details of both these experiment are described in this section; the details of the two beamlines used are listed in table 3.3, and the general set-up is illustrated in figure 3.6.

***In situ* heating:** This SAXS experiments were performed at the 7T-MPW-SAXS beamline at Bessy, using a two-dimensional position sensitive gas detector which has dimensions of 200 mm × 200 mm.

A preliminary experiment were performed on a piece of mica that was cut in two pieces, whereof one was put in a bath in a zirconia-sol for a week, and the other one were used for background measurements. The zirconia coated mica piece were dried in an oven at 120 °C for 1 hour, and afterwards a clear coating was

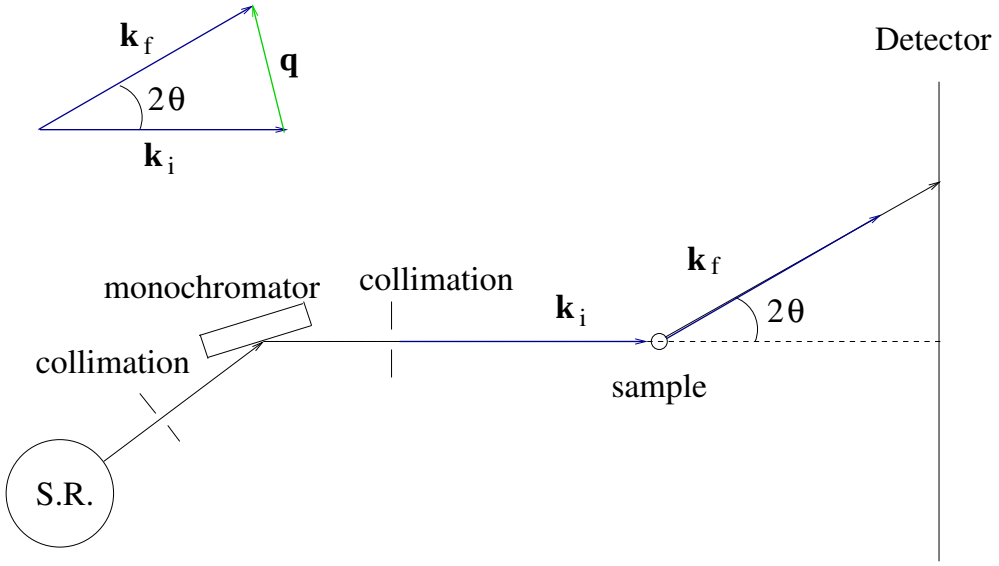

Figure 3.6: The general set-up for SAXS experiments. Synchrotron radiation (S. R.) is collimated and hits the monochromator. The monochromated light is collimated before hitting the sample (wave-vector $\mathbf{k}_i$) where the X-rays are scattered (wave-vector $\mathbf{k}_f$). The detector measures the intensity of the X-rays as function of distance from the centre. The wave-vector transfer $\mathbf{q}$ is proportional to the scattering angle 2θ, and for the small angles used here, $\mathbf{q}$ can be approximated to be parallel to the detector.

visible.

The first SAXS measurement on the zirconia coated mica piece was performed under ambient temperatures, then the sample was heated to 300 °C and another measurement was performed. The temperature was incrementally heated in steps of 50 degrees, with a new measurement performed at each temperature. The maximum temperature was 950 °C, and since the pattern was still changing, new measurements were taken for another 30 minutes, keeping the heating on such that the temperature remained 950 °C. Afterwards, background measurements were taken on the bare mica piece at different temperatures.

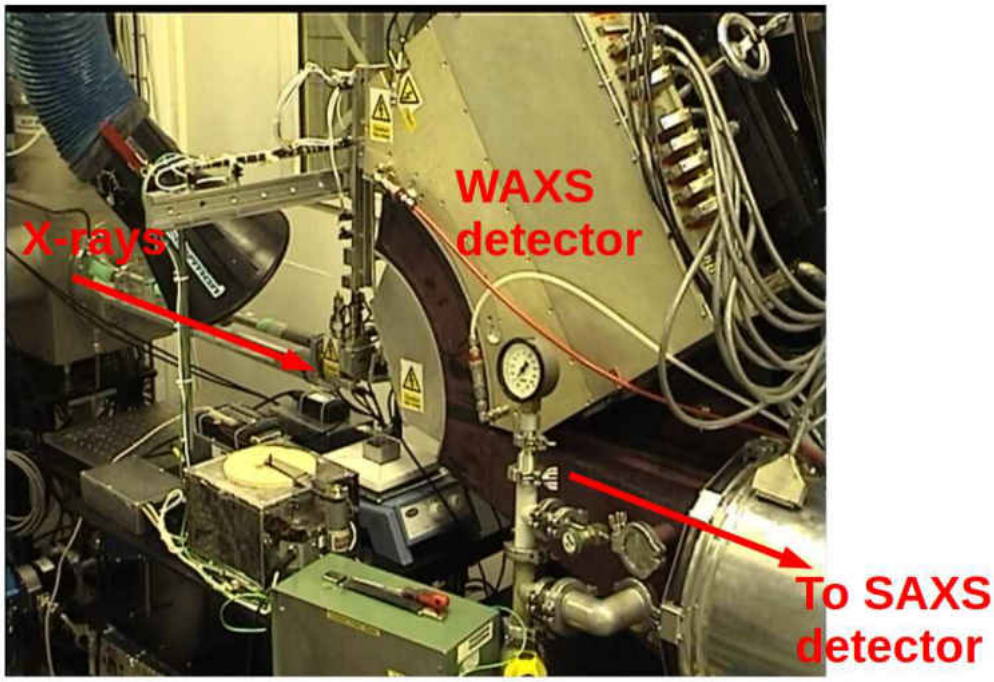

Figure 3.7: The dip-coater mounted in the experimental hutch. The beam comes in from the synchrotron and hits the sample which would be stationed in the measuring position. The transmitted and scattered beam continues down the tube, and hits the SAXS detector (not shown) a few metres away. A WAXS (Wide-Angle X-ray Scattering) detector is also used in order to simultaneously obtain the wide angle scattering signal.

***In situ* dip-coating:** The dip-coater was installed directly on the beamline at Daresbury, as shown in figure 3.7.

The dip-coater was controlled remotely by a LabVIEW program on a laptop computer outside the experimental hutch. First the furnace was heated to the desired temperature (500 or 700 °C). The measurement procedure is schematically illustrated in figure 3.8, and to start with the clean mica piece was driven into the measuring position, and a measurements was made. Next, the mica piece was dipped into the sol, withdrawn at a velocity of 1.35 mm/s, and driven back to the measuring position where a new measurement was made. Thereafter, the sample

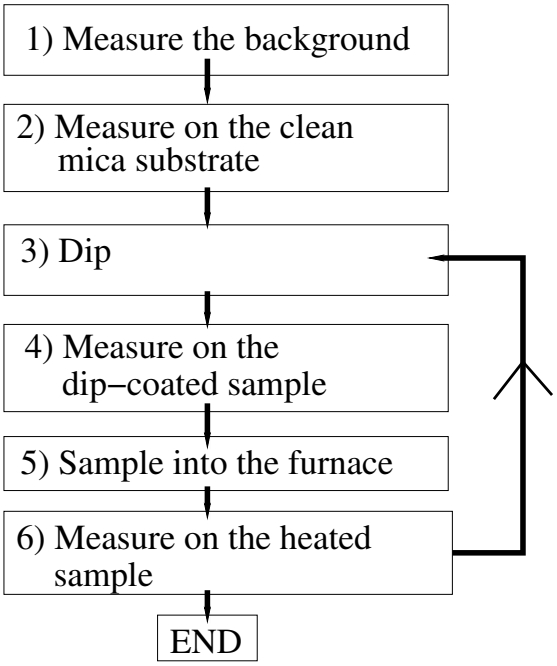

Figure 3.8: Figure illustrating the cycles of measuring, dipping and heating. Further description is given in the text.

was driven into the furnace where it stayed for 10 seconds, and then it was driven back to the measuring position where another measurement was made.

3.3.2 GISAXS

The GISAXS experiments were performed at the 7T-MPW-SAXS beamline at Bessy, Berlin, using a two-dimensional MarCCD (2048 × 2048) pixel detector. The X-ray energy was fixed to 10008 eV (λ = 0.12389 nm) and to 10000 eV (λ = 0.12398 nm) during the first and second GISAXS beamtime, respectively. The sample-detector distance was set to 2920 mm during the entire time for both beamtimes.

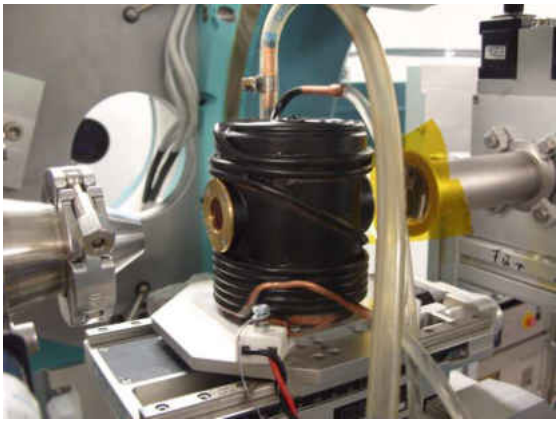

Figure 3.9: The GISAXS furnace installed at the beamline. The X-rays come in from the tube at the back (to the right in the photo), through the furnace windows and into the cone-shaped tube to the left in the photo. The sample is mounted inside the hood. The rubber tubes are for water cooling (the thin tube) and for letting in gas (the thick tube).

3.3.2.1 Furnace

A furnace for GISAXS experiments, shown in figure 3.9, was built in the institute's workshop; it consists of a circular hotplate with diameter 10 mm, and a copper hood with replaceable kapton windows. The furnace is water-cooled, and it is possible to run with an inert atmosphere within the hood. The temperature is measured using a thermocouple wired into the heating element, and it can be remotely controlled from the computer outside the hutch. The temperature can safely be set to 1000 °C in air.

3.3.2.2 Set-up

Figure 3.10 shows the experimental set-up for the GISAXS measurements; the centre beamstop was used to block the strong specular reflection of the incident beam and the direct beam, *i.e.* the part of the beam that does not hit the sample

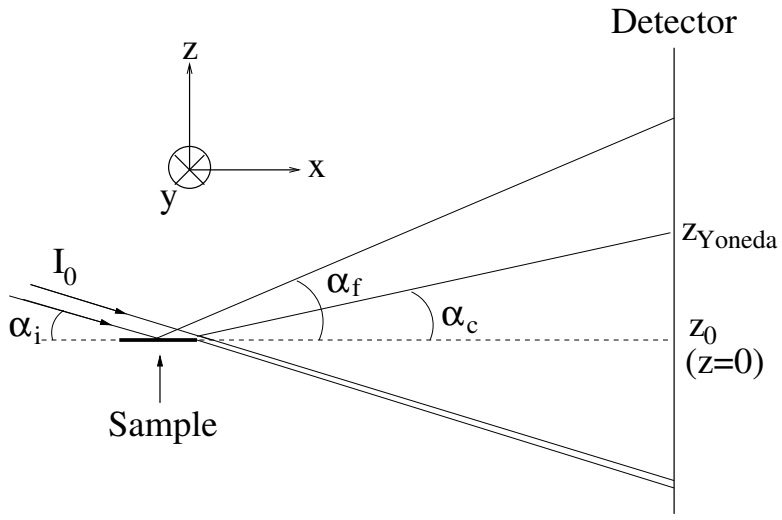

Figure 3.10: Schematic of the set-up for a GISAXS experiment: The beam is incident at an angle α_i, and some of the beam misses the sample and hits the detector further down, while the rest of the beam is reflected and scattered from the sample with exit angles α_f (along the z-axis) and $2\theta_f$ (along the y-axis). The reflected specular beam is omitted in the figure. The sample surface plane is indicated at $z_0 = z(\alpha_f = 0)$, and the Yoneda feature is observed at $z_{Yoneda} = z(\alpha_f = \alpha_c)$. (The angles are exaggerated for clarity of illustration.) [61]

and simply continues in a straight line.

The sample surface lies in the $(x, y, z = 0)$ plane, the incident angle α_i and the exit angle α_f lies in the $(x, y = 0, z)$ plane, and the horizontal scattering angle $2\theta_f$ lies in the $(x, y, z = D \tan \alpha_f)$ plane, where D is the sample-detector distance.

In the first GISAXS experiment, where the samples were the Zr-Y coatings, measurements at several incident angles were made first. Then the sample was heated using the GISAXS furnace, from 400 to 1000 °C, in steps of 50 degrees. The incident angle was fixed to 0.257°, and 10 measurements was taken at each measuring temperature, measured for 30 seconds at each. While keeping the measuring temperature at 1000 °C, the different incident angle measurements were repeated. The whole experiment was then repeated for the different Zr-Y

coatings and for a clean Si(100) wafer. During the second GISAXS experiment, where the relevant sample was a pure zirconia-coating, measurements at different angles were made using the same procedure as for the previous experiment, and the same heating programme was used. On the other hand, one suitably long measurement was taken at each temperature. The measuring time depended on the number of detector counts, and was typically 3-5 minutes.

3.3.2.3 Thermal expansion

The thermal expansion from the silicon wafer has been estimated using [62]

$$\frac{\Delta l}{l} = \int_{T_0}^{T} \alpha(T) dT \tag{3.1}$$

where $\alpha(T)$ was found using figure 4 in [62], for $T_0 = 300$ K to $T = 1273$ K. The thickness of the silicon wafer is ~ 300 μm, and the expansion for the silicon wafer, Δl, was then found to be about 1 μm. A change in height of the sample surface, does not change the angle between the reflected beam and the sample plane, and thus the reflected beam will be measured Δl higher on the detector. The pixel size is 79 μm, and the thermal expansion of the Si-wafer is significantly smaller than the pixel size of the detector. It is therefore a valid assumption to neglect the thermal expansion of the substrate in the interpretation of the GISAXS patterns.

The thickness of a coating decreases as densification take place during heating, and it was investigated by ellipsometry (see Section 6.2.2 for the ellipsometry results and for further discussions). The sample thickness was found to vary from

around 400 to 100 nm. This difference is of course also a lot smaller than the pixel size.

3.3.3 X-ray diffraction

The X-ray diffraction measurements were performed using a Bruker D8 Advance series 8 diffractometer in the theta-theta configuration and using a copper anode. Multilayer mirrors were used in order to produce a parallel beam and the spot was a few millimetres wide. A Vantec detector was used, which measures over 12° of 2θ space at once, and then scans over the rest of the desired 2θ space. The angular resolution was set to $\Delta 2\theta = 0.00716°$, and the sample rotation was turned off.

For the coatings prepared on mica substrates, the total measuring time for each sample was ~ 45 minutes, and for the coatings prepared on the Si-wafers, the total time measured was ~ 83 minutes for each.

Summary

Zirconia sols that contains none or various amounts of yttria doping were prepared. Substrates were dip-coated into the relevant sol, and the coatings containing yttria were labelled Zr-Y-A, Zr-Y-B, Zr-Y-C and Zr-Y-D depending on yttria concentration, which corresponds to 2.04, 4.17, 8.70 and 19.1 mol% yttria, respectively.

Since mica is mostly transparent to X-rays, pieces of mica were used as substrate for the SAXS measurements because these are done in transmission mode. For reflection mode, *i.e.* the GISAXS measurements, Si(100) wafers were used as

substrates since these are very flat and does not easily melt.

SAXS and GISAXS techniques were used for measuring the nano-structure of the coatings as the sample is dip-coated or incrementally heated *in situ*.

Additionally, *ex situ* XRD measurements were performed in order to gain information about the crystal structure for the coatings after annealing using different temperatures.

Chapter 4

Data analysis

4.1 Introduction

Our measurements were performed on two different beamlines and with multiple measurement geometries (*i.e.* SAXS and GISAXS). As a consequence of this, some of the experimental parameters cannot be considered to be identical. A simple example of such a parameter is the intensity of the incoming beam; as the stored electron current in the synchrotron is continuously decaying, the intensity of the incoming beam is not identical for all the measurements. Therefore, in order to perform any quantitative comparison of any two measurements, it is necessary to first normalise to the beam intensity.

In fact, there are several such factors which need to be taken into consideration and not necessarily the same factors for SAXS and GISAXS measurements. Therefore, the purpose of this chapter is to take a systematic look at the corrections

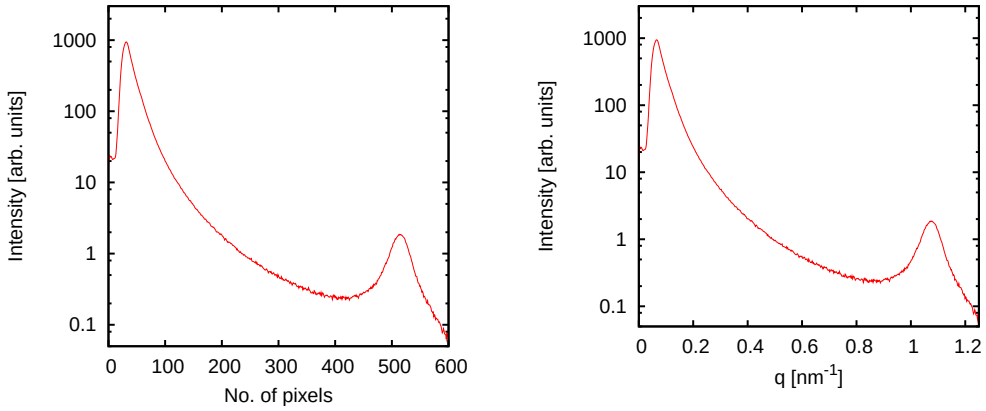

Figure 4.1: SAXS pattern from silver behenate (AgBeh) where the X-ray energy used was 8 keV and the sample-detector distance was 3345 mm. The left panel shows the intensity as a function of pixel number, and the right panel shows the new abscissa after it is converted to show q-values.

that are required for each technique used.

These corrections are summarised in table 4.1, and described in detail in the remaining part of this chapter. After these corrections are applied, it should be possible to compare the different plots within each *in situ* treatment programme quantitatively. Such SAXS pattern plots are shown in the same figure in Chapter 5, and the results are further discussed in Chapter 6.

4.1.1 Silver behenate calibration

In order to compare the results with the theory described in Chapter 2, the abscissa in the measured SAXS patterns needs to be converted to q-value instead of simply the pixel or channel number (see figure 4.1). The q-scaling can be done by directly applying Eq. (2.5);

$$q = \frac{4\pi}{\lambda} \sin\theta \quad \text{where} \quad 2\theta = \tan^{-1}\left(\frac{sN}{D}\right). \tag{4.1}$$

In Eq. (4.1), s is the pixel size, N is the pixel or channel number and D is the sample-detector distance.

Alternatively, the q-scaling can be found by using a calibrant. This is especially useful if the pixel size or the sample-detector distance is not accurately known. For the X-ray energy relevant here, silver behenate has been found to be a good candidate because it has a well-defined d-spacing of 58.380 Å [63].

A SAXS measurement on silver behenate is performed using the same sample-detector distance and X-ray energy as for the other measurements. If the measurement was performed using a 2D detector, the resulting pattern has to be radially averaged such that the 1D data can be readily plotted. Bragg peaks are now observed in the intensity *vs.* pixel number plot.

By setting $n = 1$ in Eq. 2.88 it is found that the first order SAXS peak will be situated at $q = 1.0763$ nm^{-1} (see figure 4.1), and this is then used for finding the q-scaling. Using this procedure, there is no need for explicitly refining the sample-detector distance.

4.2 General procedure for the data corrections

The procedures for correcting the data is different for the SAXS and GISAXS experiments. The procedures are however comparable and, in order to give a

simple overview, they are listed in table 4.1. Each step will be further explained in the following sections, as indicated in the right hand columns of the table.

Step No.	*Procedure*	*SAXS*	*GISAXS*
1	Image rotation		4.2.2.1
2	Normalise for measuring time and beam current	4.2.1.1	4.2.2.2
3	Radial averaging	4.2.1.2	
4	Transmission corrections	4.2.1.3	
5	Averaging		4.2.2.3
6	Vertical cuts		4.2.2.4
7	Horizontal cuts		4.2.2.5
8	Background correction	4.2.1.4	
9	Noise reduction	4.2.1.5	
10	q-scaling	4.2.1.6	4.2.2.6
11	α_f-scaling		4.2.2.7

Table 4.1: Table showing which data correction procedures that were applied to which experiment. Content in the SAXS and GISAXS column means that this correction is applied for that technique, and further explanations can be found in the section address given.

4.2.1 SAXS

4.2.1.1 Normalising

The beamcurrent varies, and the integration time of the measurement may vary; it is therefore necessary to normalise the measured data to the measured beam-current and the integration time.

For the data collected using the gas detector at beamline 7T-MPW-SAXS at Bessy, Berlin, the following procedure is used for the normalisation of the data. The corrected data, I_{corr}, becomes

$$I_{corr,i} \propto \frac{I_i}{I_{bc}t} \cdot \frac{1}{1 - t' \cdot (M/t)} \tag{4.2}$$

where I_i is the measured pixel intensity at pixel i, I_{bc} is the beamcurrent [mA], t is the measuring/integration time [s], $t' = 4.0 \cdot 10^{-6}$ s and M is the monitor counts. The second factor corrects for the dead-time of the detector.

There is also the possibility to use a CCD detector at this beamline; this detector was only used for the GISAXS experiment (see Section 4.2.2.2).

For the data collected using the one-dimensional Rapid quadrant detector at beamline 6.2 at Daresbury, England, the data were normalised using

$$I_{corr,i} \propto \frac{I_i}{I_{bc} \cdot t}, \tag{4.3}$$

where I_i is the value measured at channel i, I_{bc} is the beamcurrent and t is the measuring time.

4.2.1.2 Radial averaging

In order to proceed with the data analysis of the two-dimensional SAXS patterns, it is necessary to compute the radial average of these. This is done by first finding the beamcentre, using this position as the centre of a circle, and finding the average pixel value for each circle as the radius goes from zero to the maximum measured pixel number, divided by the circumference of the circle in order to normalise to the number of pixels that the circle extends over.

4.2.1.3 Transmission corrections

In a typical set-up for a SAXS experiment, there will always be a small signal due to background; *i.e.*, the signal from scattering of the X-rays by, for example, windows and other molecules between the exit of the beamline and the detector. This background signal can be measured, and it can be subtracted from the actual measurement. However, the sample will absorb some of the X-ray intensity, and in order to subtract the correct background intensity, the intensity from the actual measurement and the intensity from the background measurement need to be scaled accordingly relative to each other. This *transmission correction* will be described in this section, and afterwards the procedure for subtracting the background will be described.

The transmission correction is done by dividing the intensity in the sample measurement with the transmission for the sample τ_s,

$$S_i = \frac{I_{corr,i}}{\tau_s} \quad \text{where} \quad \tau_s = \frac{\tau_{s+b}}{\tau_b}. \tag{4.4}$$

In Eq. (4.4), τ_{s+b} is the measured transmission; *i.e.*, the transmission for both sample and background, and τ_b is the transmission for the background measurement.

First it is important to determine what the background actually is. Figure 4.2 shows measurements of the coated mica, the clean mica and the difference between the two, for the experiment performed at Bessy. The measurement taken at ambient temperature is shown in the left hand panel; here it is observed that the

contribution from the clean mica is small, and the curve where this contribution is subtracted is similar but having slightly lower intensity than the curve from the measurement on the coated mica. In this case it works well to use the clean mica as the background measurement.

On the other hand, using the mica measurement as background for the measurements at high temperature is problematic. An attempt was made to use mica as a part of the background signal (see figure 4.2, right hand panel), however, when this was used, the "corrected" measurement (after subtracting the background) are seen to contain physically unrealistic features at very low pixel numbers (*i.e.* small angles). Whilst the reason for this is not completely understood, a simple alternative is given below.

A measurement performed without any sample present can be used as *background measurement* ("B") since the only difference between this measurement and the actual measurement is that there is no sample in the furnace. The measurements for the coated mica will then be the *sample measurement* ("S"). In other words, for the SAXS measurements from Bessy, the background is given by

$$B_i = I_{corr,i}, \tag{4.5}$$

where $I_{corr,i}$ is the measurement performed when the furnace was empty, after correcting it for beamcurrent and measuring time.

In the dip-coating measurements performed at Daresbury, mica was also used

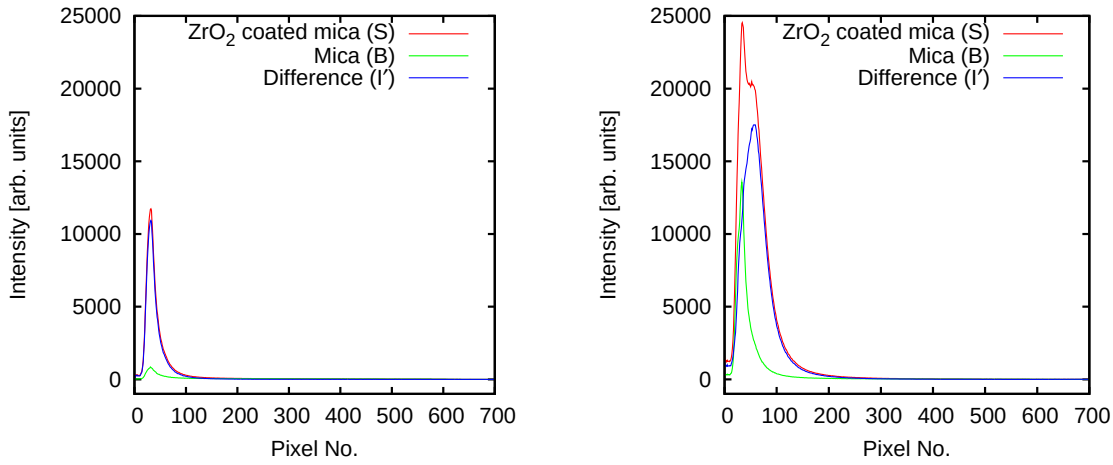

Figure 4.2: The comparisons of the contribution from the coated sample, the clean mica and the difference between the two. Left: Both the coated sample and the clean mica were cold when the measurements were performed. Right: Measurement number 4 for the coated sample after setting the furnace temperature to 950 °C, which is a typical measurement for the high temperature range. The mica was also heated to 950 °C when this measurement was performed.

as the substrate; for this experiment the mica- and the coating signal could be separated successfully, and thus the measurement on the clean mica was used as background; $\tau_b = \tau_{mica}$. For the SAXS data measured at Daresbury, the background measurement is simply given by Eq. (4.5), where in this case $I_{corr,i}$ is the normalised file for the clean mica measurements.

4.2.1.4 Background correction

In order to separate the signal from the scattering by the sample from the background contributions, such as scattering from air molecules or from the windows, it is desirable to subtract the background contributions. This can be done by

$$I_i' = S_i - B_i \tag{4.6}$$

for each pixel i where S_i and B_i are found from Eqs. (4.4) and (4.5), respectively. This procedure worked well for the *in situ* dip-coating experiment, however, it did not work for all the SAXS measurements in the *in situ* heating experiment, and an alternative procedure is described below.

For the *in situ* heating experiment at Bessy, the reason this procedure did not work is that $S_i < B_i$ for large q-values. The measurement on the empty furnace ("B") was taken after the sample measurements and the subsequent measurements on the clean mica, where both samples had been heated to 950 °C, and perhaps the reason for the increased intensity in "B" is that some of the experimental parameters, such as beamcurrent, changed too much within this time.

However, the intensities at the highest q-values could be compared for nearly all the measurements, since scattering from the sample was not detected at a range of q-values towards the highest values of q. Therefore, the average intensity for this range was compared for the sample- and the background measurements,

$$a = \frac{\bar{B}_{high-q}}{\bar{S}_{high-q}}, \tag{4.7}$$

and the intensities of the sample-measurement was scaled according to this result.

Figure 4.3 shows the values obtained for a, for the measurements where this was clear, and the lines fitted to these points. a is estimated from these fits, and used for the intensity scaling,

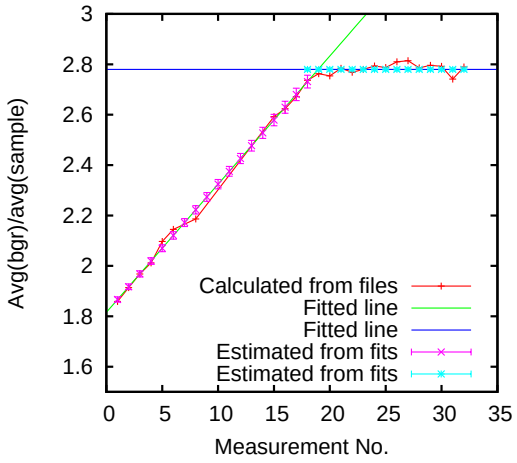

Figure 4.3: The red points are the calculated values for a using Eq. (4.7). The green and blue lines are the lines fitted to the red points. From these fits, the value used for a is found, and applied using Eq. (4.8).

$$S'_i = a \cdot S_i, \tag{4.8}$$

for each temperature measurement. Eq. (4.6) is now replaced with

$$I'_i = S'_i - B_i. \tag{4.9}$$

Figure 4.4 shows the same sample measurement as figure 4.2, but here the empty furnace measurement is used as background.

4.2.1.5 Noise reduction

Due to using the detector for an experiment that it is not optimised for, the signal-to-noise ratio in the data collected in Daresbury was not satisfactory; this is a common problem in experimental physics. On the other hand, the detector had many more channels than strictly necessary, and thus the position of two

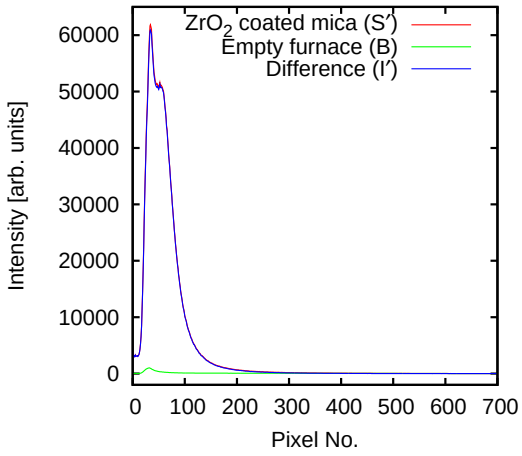

Figure 4.4: Measurement number 4 after setting the furnace temperature to 950 °C. This figure shows the contribution from the coated film, the empty furnace measurement and the difference between the two.

neighbouring channels differ by such a small angle that the difference in the measured signal count should be small, and thus any observed difference is mostly due to interchannel noise. A common way to solve this type of problem is to use a Fast Fourier Transform (FFT) filter, since by removing the high frequencies (which corresponds to the extremely small angular separations) is predominantly the noise which is removed, and hence the signal-to-noise ratio is significantly improved.

The filtering was performed by using a purpose-made C-program based on an FFT routine written by Dr. Rudolf Winter taken from Numerical Recipes in C [64]. In my program, the data is first Fourier transformed into the frequency domain, then the frequencies corresponding to unphysical interchannel noise were removed (the upper 50 %). Finally the filtered frequency domain data was inverse Fourier transformed to the real space domain. This data was then substituted for the unfiltered data.

The data collected in Bessy had a far higher signal-to-noise ratio, and no

significant improvement could be made by filtering.

4.2.1.6 q-scaling

The reason for q-scaling, as well as the general procedure, has already been discussed; see section 4.1.1. The aim of this section, however, is to describe how the q-scaling was specifically performed for the measurements in this work.

For the data collected at Bessy (the zirconia-coated mica experiment), the q-scaling was applied to the abscissa using the following procedure: As a calibration, silver behenate (see section 4.1.1) was used. The pixel number for the silver behenate peaks as function of calculated theoretical q-position was plotted and a straight line

$$N \equiv f(q) = a \cdot q + b \tag{4.10}$$

was fitted to the plotted points. In this case, b was found to be at zero. Now a can be determined. Since θ is very small, it is acceptable to use a linear approximation in Eq. (2.5):

$$q = \frac{4\pi}{\lambda} \sin\theta \approx \frac{4\pi}{\lambda}\theta \equiv a' \cdot N, \tag{4.11}$$

where $a' = 1/a = 2.089 \cdot 10^{-3}$ nm^{-1}/pix and N is the pixel number.

For the data collected at Daresbury (the dip-coating experiment), the q-scaling procedure was performed slightly different since $b \neq 0$ for these measurements

($b \approx -10$ channels):

$$x \equiv f(q) = a \cdot q + b. \tag{4.12}$$

where x is the channel number. Consequently,

$$q = \frac{x - b}{a} \tag{4.13}$$

$$q = \frac{4\pi}{\lambda} \sin\theta \approx \frac{4\pi}{\lambda}\theta \equiv \frac{N}{a}, \tag{4.14}$$

where in this case $N = x - b$, and $a \approx 221$ channels/nm^{-1}.

4.2.2 GISAXS

4.2.2.1 Image rotation

Figure 4.5 shows an example of one of the raw files from the GISAXS experiment, where the output files from the detector are 2048×2048 pixels tiff-files.

For ease of analysis, it is desirable that the vertical detector axis is corresponding to the sample normal. Although this is almost right, it is clear from the image that a small correction is needed. The image was therefore rotated by a small angle which was determined by geometrical considerations, *e.g.* reading off the vertical pixel value of the horizon on the outer left and right end of the picture, and calculating the difference Δz. Δy is the difference in horizontal pixel number, where the two pixels used should on be the same distance each from the mirror

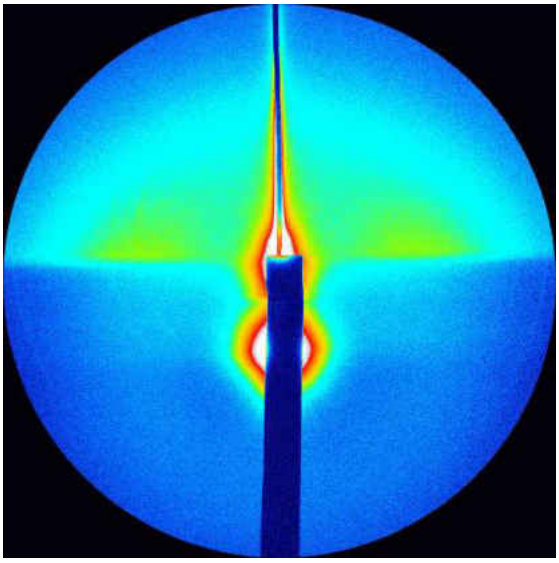

Figure 4.5: Raw image from coating B heated to 550 °C.

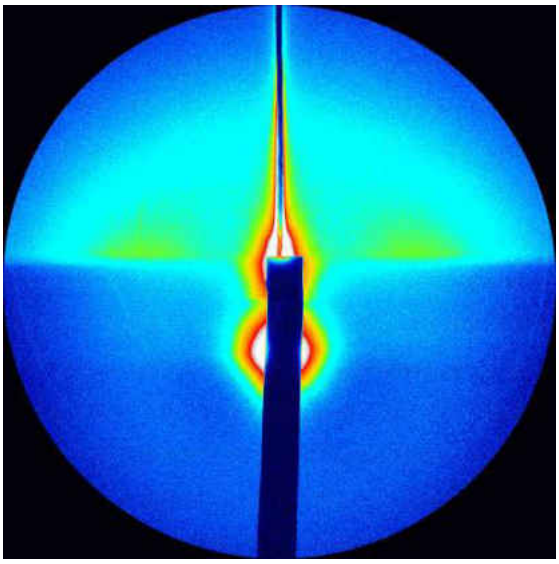

Figure 4.6: Raw image rotated (coating B heated to 550 °C).

axis. The rotation angle ν is found by using that $\tan\nu = \Delta z/\Delta y$, and figure 4.6 shows the raw image from figure 4.5 rotated by an angle ν such that the sample normal now coincides with the vertical detector axis.

4.2.2.2 Normalising

The data were collected using a MarCCD detector during this experiment. The rotated tiff-files are corrected, pixel by pixel, by:

$$I_i' = I_i \cdot \frac{t_{norm}}{t} \cdot \frac{I_{bc,norm}}{I_{bc}} \tag{4.15}$$

where I_{bc} is the beam current [mA], $I_{bc,norm} = 200$ mA, t is the measuring time [s] and $t_{norm} = 30$ s. Regarding possible efficiency variation across the the detector face, the beamline staff have performed initial tests and concluded that intensity variations is not necessary to correct for in the case of this CCD detector.

4.2.2.3 Averaging

For the measurements for which the measuring time was short, and we have several measurements for the same set-up, a few images are averaged to get better statistics. The patterns typically change slightly during the first few measurements after ramping up the heating. Therefore, to allow for equilibration, the average of the last five of ten measurements in total was calculated at each temperature,

$$I_{avg} = \frac{1}{5} \sum_{j=5}^{9} I'_{frame(j)}, \tag{4.16}$$

and this result was used for further analysis.

4.2.2.4 Vertical cuts

A vertical cut (normal to the sample plane) is taken from the input file at a specified pixel value, and the average of 4 pixel columns is calculated. The reason for why 4 pixel columns are used, is that a compromise between improved statistics and blurring due to too many pixel columns, was needed.

4.2.2.5 Horizontal cuts

The same procedure as for vertical cuts was used, only this time the cut direction is taken to be parallel to the sample surface.

4.2.2.6 q-scaling

Section 4.1.1 described the procedure for transforming pixel numbers to q-space. For small exit angles ($\alpha_f \approx 0$), the following approximation is valid for scaling the q_y axis of the horizontal cuts:

$$q_y = \frac{4\pi}{\lambda}\sin(\theta_f), \quad \text{where} \quad 2\theta_f = \tan^{-1}\left(\frac{s(y-y_0)}{D}\right). \tag{4.17}$$

$s = 79$ μm is the pixel size, $D = 2920$ mm is the sample-detector distance, y is the horizontal pixel coordinate and y_0 is the pixel number for the beamcentre in the horizontal direction. The cuts are typically taken at the critical angle, and since this angle is small, the relations above are still valid as q-scaling for the cut at this height which is labelled z_{Yoneda} (*cf.* figure 3.10).

This procedure was compared to measurements of the silver behenate calibrant

(see, for example, [63; 65]), and both methods gave the same result.

4.2.2.7 α_f-scaling

The scaling for the vertical cuts was found by

$$\alpha_f(z) = \tan^{-1}\left(\frac{s(z - z_0)}{D}\right), \tag{4.18}$$

where α_f is the exit angle between the scattered beam and the film, z is the pixel number in the vertical direction, and z_0 is the sample plane (see figure 3.10). z_0 was found by

$$z_0 = z_{Yoneda} - \frac{D}{s}\tan\alpha_c, \tag{4.19}$$

where α_c was calculated from Eqs. (2.46) and (2.62), and z_{Yoneda} is the pixel number of the Yoneda feature in the z-direction.

4.3 Other corrections for GISAXS?

In literature other corrections for GISAXS patterns are also mentioned. For example, Kutsch *et al.* emphasises that: "An important point in the data treatment of SAXS measurements in grazing incidence is the correction for absorption and refraction effects" [66].

Absorption corrections As discussed for the transmission SAXS measurements, the background intensity was subtracted in order to separate the signal

from the background and from the sample. But first, in order to subtract the correct amount, the absorption of the X-rays within the sample had to be accounted for (see section 4.2.1.3).

In GISAXS however, it is problematic to subtract the background. This is because of the reflection geometry, and especially because a coating has a different critical angle than the substrate. This means that the Yoneda feature is positioned differently on the detector relative to the sample horizon for a measurement of a coated substrate compared to the bare substrate. It is not trivial to account for such an effect.

On the other hand, it might not be necessary to subtract the background. This has indeed found to be the case when the scattering from the coating is large compared to scattering from the substrate. For the case where the substrate is very flat, there will be minimal scattering from the substrate. This is easily tested by a measurement of the clean substrate.

In our measurements, silicon (100) wafers were used as substrates. The scattering from these was found to be insignificant, and it was therefore assumed that it is not necessary to subtract the contribution from the Si-substrate in these measurements.

This discussion can be extended to air scattering between the end of the beamline and the flytube, as well as scattering from the windows in these devices. Previous measurements have shown this scattering to be insignificant, and it was therefore assumed that it is not necessary to subtract these background contribu-

tions.

When it comes to absorption within the sample, the situation is different; the X-rays are attenuated by the material, and this attenuation depends on the travel distance of the rays within the sample (see section 2.3.2.2). In theory, one can calculate the intensity reduction of the primary beam by using Fresnel's equations (see, for example, the equations within section 2.4.1) and that the intensity attenuation behaves as $e^{-\mu L}$ where μ is the linear X-ray attenuation coefficient and L is the pathlength. However, this is not especially useful for scattering experiments, where it is the scattering pattern that is of interest. In this case, problems arise because the position of the scattering centres within the sample is not exactly known. It is therefore difficult to calculate the length of the beampaths, and it is thus problematic to calculate the absorption of the scattered beam - although one approach is demonstrated in [66].

Before calculating these beam paths, it is worth investigating whether this absorption correction is significant or not. This of course depends on how large the absorption effect is, and whether the final 1D-SAXS pattern (after the reduction of the 2D GISAXS pattern) becomes distorted as a result of not applying this correction, *i.e.*, whether it is independent on $2\theta_f$.

In our case, the horizontal cuts are taken at the Yoneda feature, which means that the exit angle equals the critical angle of total external reflection. Recall from the section about the Yoneda feature (section 2.4.2), that this effect arises from the interference between the four beams that are scattered from each irregularity

or object on the sample surface. The connection between this enhanced intensity and sample absorption is not trivial.

However, intuitively it can be seen that absorption depends more on the angles normal to the sample than parallel to the sample. It is therefore a reasonable assumption that the absorption is independent on $2\theta_f$ for the small angles considered here, and that it is possible to use cuts parallel to the sample without any corrections for absorption (cuts normal to the sample would however need this correction).

Refraction corrections: The X-ray beam is refracted as it passes the coating-air interface, and in literature the measurements have commonly been corrected for refraction [66; 67; 68]. The reason this is not necessary here, is that our plots of the vertical cuts are plotted with the exit angle as abscissa, *i.e.*, the actual measured exit angle of the scattered beams. However, if q-scaling is to be used, it would be necessary to scale the q-value accordingly. This is because from a scattering event within a medium where the beam is scattered at a certain angle, refraction occurs as the beam exits the medium, and a slightly different scattering angle is measured. In order for the vertical plots to be informative, it is necessary to find the wave-vector transfer q as function of the actual scattering angle, and not the measured one.

Refraction corrections are only useful for extracting further information, such as the radius of gyration and Porod slope, in directions different to the direction parallel to the sample plane. For more details about refraction corrections, see for

example, [66].

Furthermore, in the case where the incident angle and the exit angle is close to the critical angle, it is necessary to employ DWBA due to interference effects; see figure 2.6 and Eq. (2.84). The most realistic approach to this problem is make a realistic model for the system and then simulate the scattering pattern (computer programs are already available on Internet, *e.g.* IsGISAXS [69]).

The kind of materials studied in this work only allows for restricted models, and spherically symmetric particles have been assumed. So far only plots along the direction parallel to the sample surface have been investigated. Of course, the shape of the particles are not necessarily spherical, and it would therefore also be interesting to obtain the radius of gyration and Porod slope from plots along other directions as well.

4.4 Quantification despite large changes in the GISAXS pattern

As shown in figure 4.7, the GISAXS pattern changes significantly during the *in situ* heating programme. This occurs because the film structure changes as the temperature increases. At the same time, the density increases, which in turn causes δ and β to increase (see Eq. (2.62)). According to Eq. (2.46), the critical angle for the film, α_c, will also increase, and consequently the Yoneda feature will be observed at higher exit angle α_f (Eq. (2.45)).

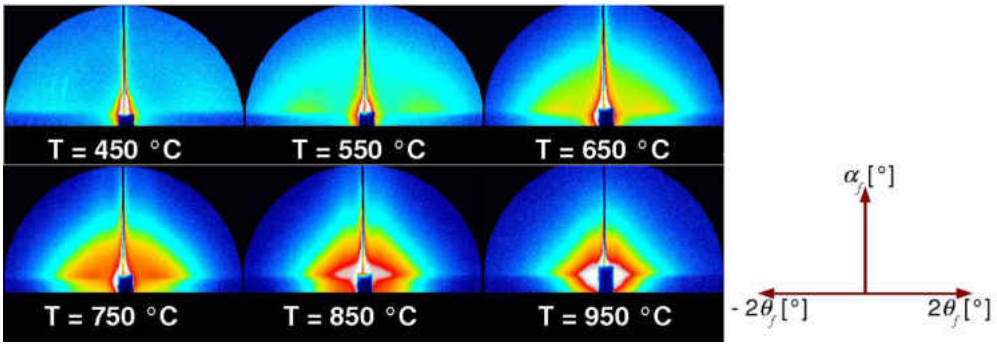

Figure 4.7: The GISAXS patterns for the Zr-Y-B coating taken at different temperatures are shown to the left, and the axes labels are shown to the right. Note that the pattern changes significantly as the sample is heated; from having distinct wings, via more powderlike patterns, and finally broadening along the y- and z-directions. A method of extracting horizontal 1D cuts such that the different measurements are quantitatively comparable was developed and is described in this chapter, and a suggested model of the sample development during heating is described in Section 6.5.3. [61]

Consequently, horizontal cuts cannot simply be taken at fixed detector channels; instead a method is needed that finds the appropriate horizontal cut for each measurement such that the information obtained from each is comparable. A procedure to achieve this was developed and is described as follows.

For example, figure 4.8 shows how the lines were selected for further 1D-SAXS analysis for sample B heated to 550 °C. As indicated in panel (A), a vertical cut (panel (B)) was taken at the same horizontal pixel value (width) for the entire heating process since the sample set-up does not change in the sideways direction. The main feature (above the horizon in panel (A) and (C)) is the Yoneda feature. The vertical cut needs to be taken far enough away from the central beamstop so that the diffusely reflected beam contributions do not interfere, and at the same time near enough to distinguish the Yoneda feature for all temperatures. When this pixel-value is selected, then the cuts are taken as shown in panel (A) and (B),

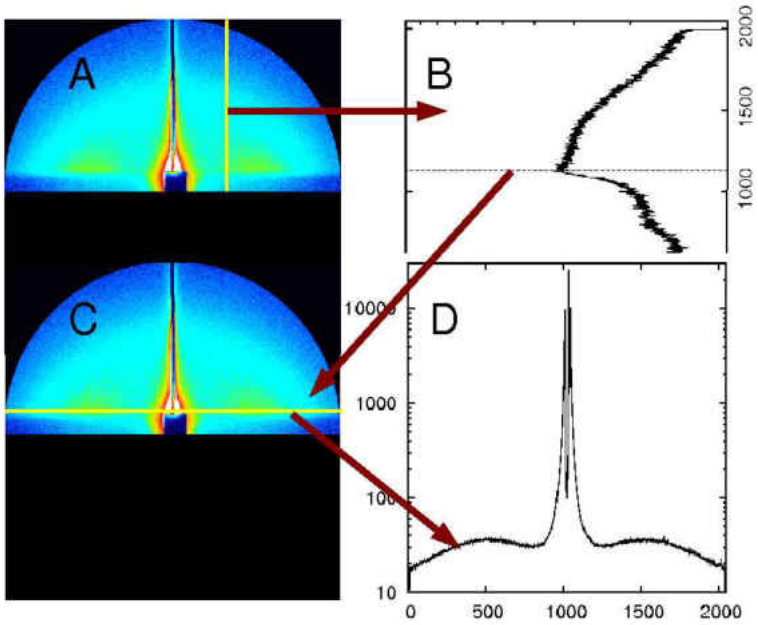

Figure 4.8: Figure indicating how the line was selected for further 1D analysis (Coating Zr-Y-B, 550 °C). [61]

following the procedure described in Section 4.2.2.4. From the vertical cuts, the position of the Yoneda feature is found (the maximum in the plot shown in panel (B)), and this is where the horizontal cuts are taken (panel (C)), as described in Section 4.2.2.5; this height is z_{Yoneda} in figure 3.10. The horizontal cut at the Yoneda height is shown in panel (D).

The line indicated in figure 4.8 (panel (A)), is the line selected for the vertical cuts for all the measurements of sample B, and the procedure for selecting the horizontal cuts was repeated for each temperature that was measured at. Now, the horizontal cuts gives SAXS patterns that can be analysed further with conventional SAXS analysis methods, and some of these cuts are shown in figure 4.9.

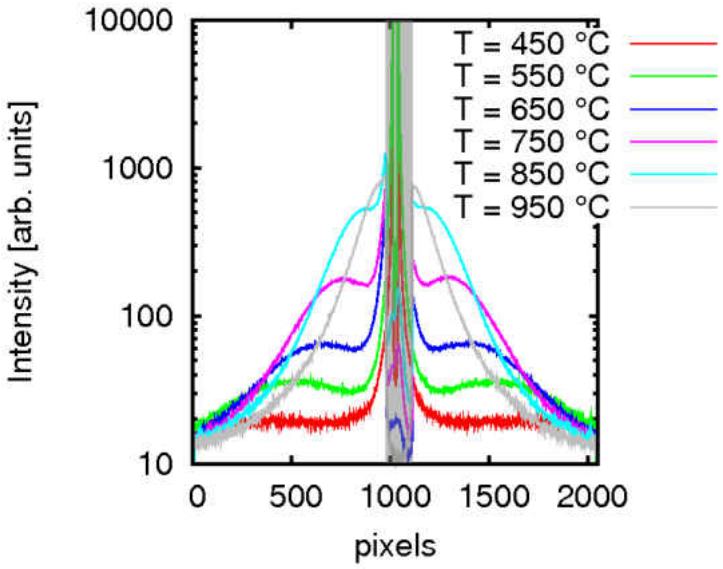

Figure 4.9: 1D horizontal cuts at the Yoneda feature for the different temperature measurements shown in figure 4.7. The shaded area corresponds to the beamstop. [61]

Summary

The GISAXS images were first rotated such that the horizon in the image coincides with the true horizon. For all measurements, including SAXS, the raw data were normalised to measuring time and incoming beam current.

For the SAXS measurements, the intensity of the resulting SAXS patterns were scaled in order to correct for absorption, and the relevant background measurement was subtracted. For the GISAXS images, 1D cuts were taken along the y-direction at the position of the Yoneda feature.

The resulting 1D patterns, both from the SAXS and the GISAXS experiments, then had the abscissa converted to show the q-value instead of the pixel/channel number. Now the resulting plots can be used for further quantitative investigations.

Chapter 5

Results

5.1 Introduction

Properties of the of dip-coated zirconia and yttria-doped zirconia sol-gel coatings, such as size, surface structure and distribution of particles, are likely to depend on yttria concentration and temperature. The aim of these experiments is thus to investigate these properties of the coatings during *in situ* treatment.

Small-angle scattering techniques are especially useful for *in situ* experiments because by using these techniques, measurements of high signal-to-noise ratio can be obtained whilst using short exposure times, which means that changes that happens to the structure of the sample over short time scales can be resolved. Moreover, these techniques can be used whilst exposing the sample to high temperature or pressure; this is for example relevant for studying thermal barrier coatings (TBCs) and catalysis reactions whilst exposing the sample to realistic

operating conditions. This is, in fact, a major advantage of X-ray techniques compared to, for example, transmission electron microscopy (TEM) which needs to be run under ambient conditions.

Furthermore, small angle scattering techniques are sensitive to nanometre scale electron density fluctuations; it is found to be a excellent technique for extracting information about the size of particles within the sample and their surface structure.

Measurements performed at different temperatures during the *in situ* heating programme are plotted together in order to show how the pattern changes for increasing temperatures. For the *in situ* dipping experiment, the pattern measured after different numbers of dips are plotted in the same figure, such that the effects of the dipping- and heating cycles can be studied. In order to study the effects of using different incident angles in the GISAXS experiment, patterns measured using different incident angles are also shown. X-ray diffractograms for the different samples heated to 500, 700 and 900 °C *ex situ* are also shown, such that the crystal structure may be investigated for these coatings.

For the *in situ* (GI)SAXS measurements, the most interesting feature to observe is the shoulder in the pattern, and how the position of this shoulder shifts. From Eq. (2.88), it was observed that the q-value at which the feature is positioned at and the correlation length d are inversely proportional. Since the radius of gyration is related to the correlation length, $R_g \sim d$ can be used as an approximation, which means that the shift of shoulder position gives information about

the development of the size of particles within the sample as the sample undergoes *in situ* treatment.

5.2 SAXS

5.2.1 *In situ* heating experiment

In the first SAXS experiment, the sample was prepared differently to the other experiments (see Section 3.3.1), and it is therefore considered as a *preliminary* experiment. The data was collected at Bessy, and some of the results are shown in figure 5.1. The reason for not plotting all the result is readability of the figure. The intermediate measurements follow the same trend as the ones that are plotted. At temperatures less than 700 °C, no obvious structure is observed. Between 700 and 950 °C the pattern changes significantly; a new shoulder appear at the high-q end, and it shifts towards low q-values. At 950 °C the pattern continues to change, and therefore the temperature was kept stable whilst several more measurements were performed. The shoulder kept creeping towards lower q-values, which indicates an increase in the size of the scattering objects.

A pronounced shoulder is an indication that it is necessary to apply a structure factor, which means that there is some degree of ordering of the scattering objects within the sample (see Section 2.2.2.3 and Appendix B). These results will be further discussed in Section 6.5.1.

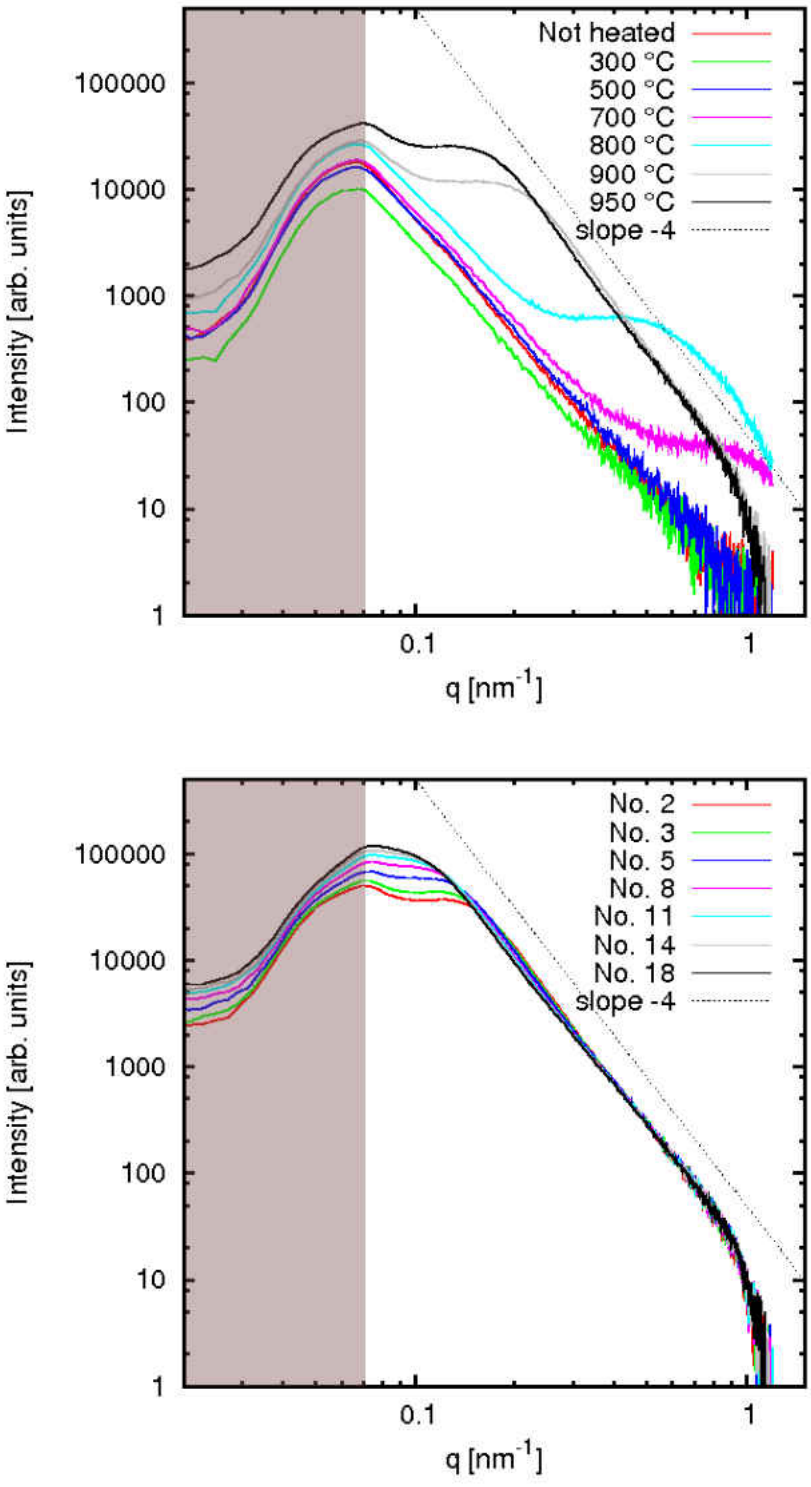

Figure 5.1: ZrO_2 coating on mica measured by SAXS during *in situ* heating. The shaded area is masked, fully or partly, by the beamstop. Upper panel: Incremental heating up to 950 °C. Bottom panel: Some of the results obtained after the temperature was fixed to 950 °C.

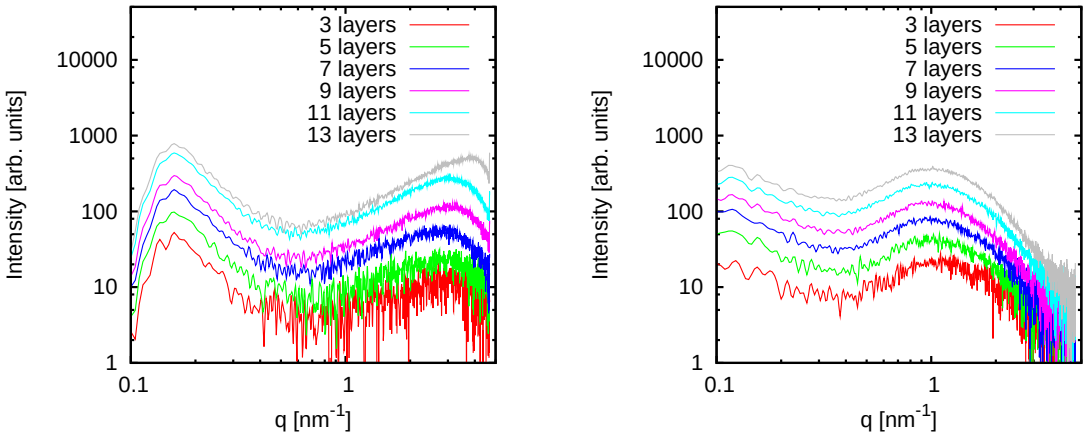

Figure 5.2: Figure showing the SAXS patterns after different numbers of dips, for the Zr-Y-B coating ($E = 16.8$ keV). Left: 500 °C. Right: 700 °C.

5.2.2 *In situ* dipping experiment

5.2.2.1 Different temperatures

The furnace was set to give an approximate constant temperature during the entire experiment for each sample. Sample B is the sample containing 4.17 mol% yttria, and for this sample measurements were performed when the furnace temperature was set to 500 and 700 °C, and the X-ray energy was fixed to 16.8 keV. These results are shown in figure 5.2, in the left and the right hand panel, respectively.

For both the experiments shown in figure 5.2, it is worth noting that the intensity have not been altered in any other way than the standard corrections described in Section 4.2.1. The scattering intensity really does increase significantly with increasing number of dips that is performed, *i.e.* number of layers.

Note that for the measurement performed with a furnace temperature of 500 °C (figure 5.2, left hand panel), the peak position is shifting towards *larger* q-values.

Possible reasons for this will be discussed in Section 6.5.2.1. In the measurement performed with a furnace temperature of 700 °C, however, the peak position remains at almost constant q-value (see figure 5.2, right hand panel).

5.2.2.2 Different coatings

In order to study the influence of yttria doping, a series of measurements were performed in which the yttria concentration of the coating was varied in a few steps between 0 to 100 %. Some of these results are shown in figure 5.3. The measurements for the zirconia coating (figure 5.3 (upper left)) was taken using the X-ray energy 17.8 keV, and the furnace temperature was set to 530 °C. For the other measurements, the X-ray energy was set to 16.8 keV, and the temperature to 500 °C. The result for the Zr-Y-A coating is shown in figure 5.3 (upper right), the result for the Zr-Y-B coating in figure 5.3 (bottom left) (and also in 5.2, left panel) and the result for the pure Y_2O_3 coating is shown in figure 5.3 (bottom right). Notice the difference in shape and position of the peak at the high-q end for the samples containing zirconia; the more yttria, the larger q-value this peak is positioned at, and the narrower the peaks are.

5.3 GISAXS

5.3.1 *In situ* heating experiments

As already mentioned for the SAXS experiments, properties of the of dip-coated zirconia and yttria-doped zirconia sol-gel coatings, such as size, surface structure

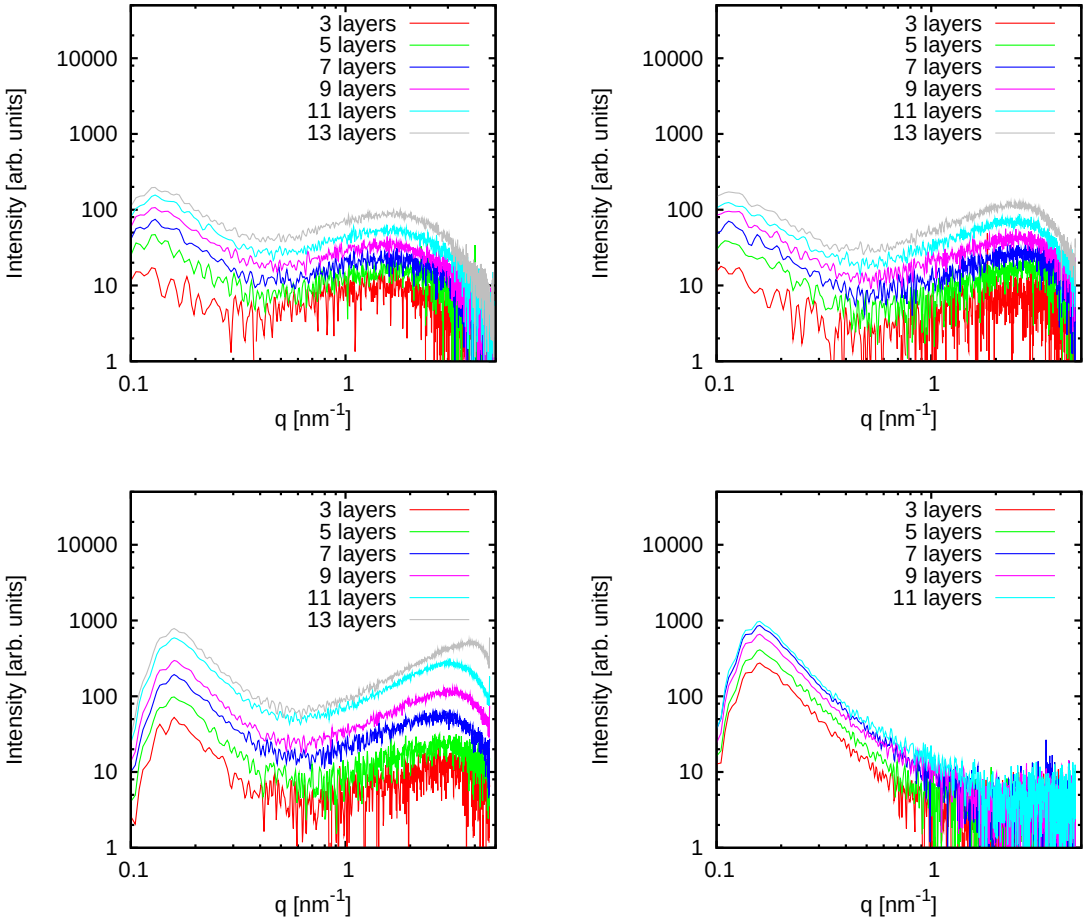

Figure 5.3: Comparison of the different yttria concentrations, when the furnace temperature was set to ≈ 500 °C. Recall that the different coatings are labelled Zr-Y-A, Zr-Y-B, Zr-Y-C and Zr-Y-D corresponding to increasing yttria content, which is 2.04, 4.17, 8.70 and 19.1 mol%, respectively (see Table 3.1). Upper left: ZrO_2. Upper right: Coating Zr-Y-A. Bottom left: Coating Zr-Y-B. Bottom right: the pure Y_2O_3 coating.

and distribution of particles, are likely to depend on temperature. Sintering and calcination of the coating material can also be expected. In order to study the various stages of these processes within the coating during heating, the samples were heated *in situ* as described in Section 3.3.2.2.

The result obtained for the Zr-Y-B coating (*i.e.* sample B) has already been shown in figure 4.7, where it was discussed that the two-dimensional (2D) GISAXS patterns change significantly during the heating programme. Cuts are extracted from these 2D patterns using the procedure illustrated in figure 4.8, and the results are shown in figure 5.4. The left hand panel shows the vertical cuts for the line indicated in figure 4.8 (A) with the abscissa scaled after Eq. (4.18). Note that the peak position for the vertical cuts (figure 5.4 (left panel)), *i.e.* the Yoneda peak, shifts slightly, from $\alpha_f \approx 0.21°$ to $0.25°$ as the sample is heated, which corresponds to the density increase from 3750 kg/m^3 to 5025 kg/m^3 [70]. The right hand panel of figure 5.4 shows the 1D horizontal cuts for the same measurements, at the cut indicated in figure 4.8 (C). In this figure it is observed that the position of the shoulder shifts towards lower q-values as the temperature was increased, which corresponds to an increase in the size of the scattering objects within this coating.

5.3.1.1 Different coatings

In order to study the effect of different yttria concentrations, the results for the zirconia sample from the second GISAXS beamtime, together with the results from the Zr-Y-A, Zr-Y-B and Zr-Y-D coatings from the first GISAXS beamtime, measured at 850 °C, are all plotted together in figure 5.5. The intensity scaling

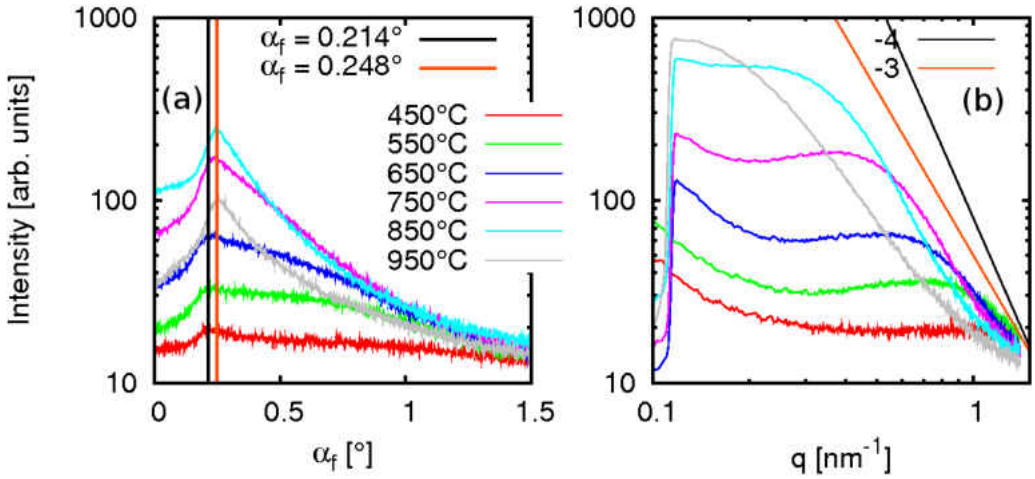

Figure 5.4: Coating Zr-Y-B heated *in situ* (incident angle, $\alpha_i = 0.257°$). (a) vertical cuts (taken as indicated in figure 4.8(A)). The peak is the Yoneda feature. (b) Horizontal cut at the Yoneda peak. The straight lines having slopes of -4 and -3 are put in as guides. [61]

is different between the samples and cannot be ascertained on an absolute scale because different fractions of the beam are captured by the sample. The position of the shoulder can, however, be compared; the position of the shoulder is very similar for coating Zr-Y-A and Zr-Y-B, whilst for coating Zr-Y-D and for the zirconia sample, the shoulder is positioned at larger q. At this temperature, then, the scattering objects within coating Zr-Y-A and Zr-Y-B are larger than the scattering objects within coating Zr-Y-D and the zirconia coating.

Zirconia Figure 5.6 shows shows a few of the GISAXS measurements for the zirconia coated silicon wafer which was heated *in situ*. From all of these measurements, a horizontal cut were taken at the Yoneda feature, and the result is shown in figure 5.7. It was noted that a sudden decrease in intensity happened around 700 °C. The reason for this plummeting of intensity is not completely clear. The

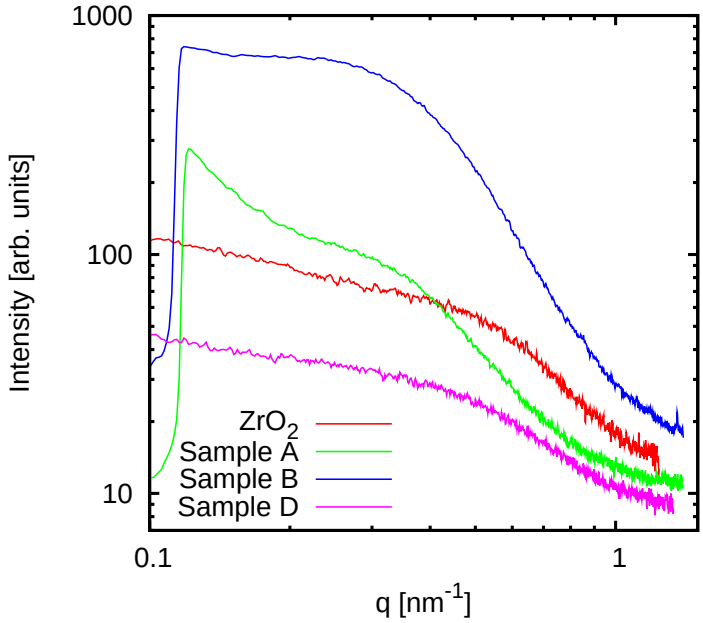

Figure 5.5: Comparison of the 1D horizontal cuts for the zirconia sample, and the zirconia-yttria samples containing different amounts of yttria; measured at 850 °C.

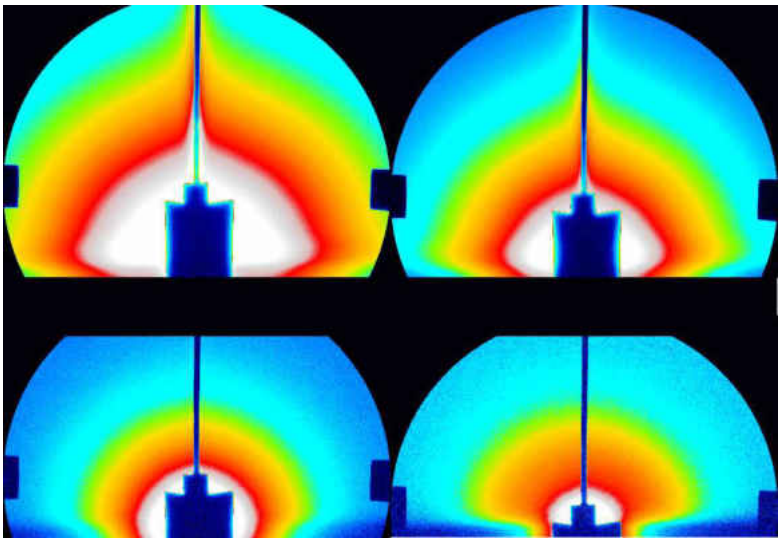

Figure 5.6: *In situ* heating measurements of the zirconia coating. From left to right, top to bottom: 650, 700, 750 and 800 °C.

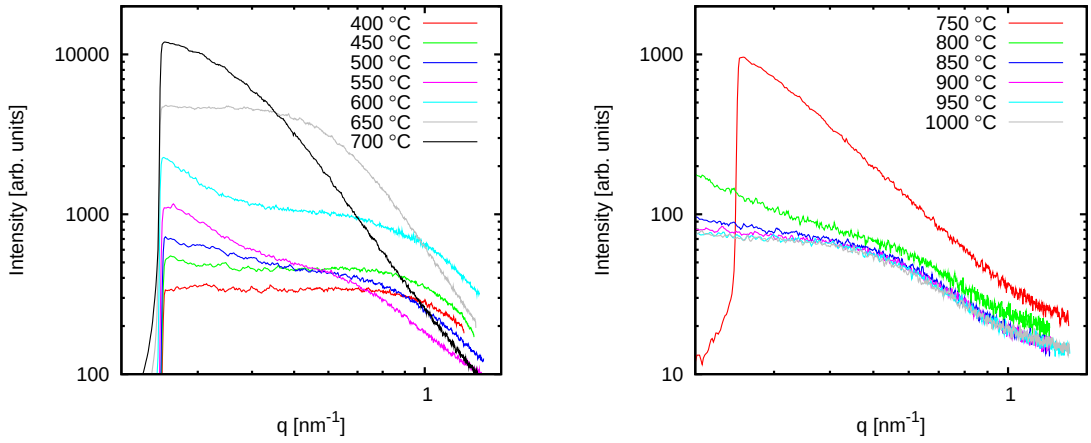

Figure 5.7: GISAXS measurements of the *in situ* heated zirconia coated Si(100). The intensity falls drastically between 700 and 750 °C, and therefore the plots of the measurements are split into two figures: The figure in the left hand panel shows the measurements for temperatures up to 700 °C, and the figure in the right hand panel is the plots for the 750 °C measurement and up. Notice that in the right hand figure the ordinate is one tenth of the ordinate of the left hand figure.

only experimental parameter which was altered was the angle δ:

In order to keep the detector count rate at a sensible level, the angle δ had to be adjusted. This is the angle (height) at which the detector (and consequently beamstop) is situated. Reducing the angle δ, as was needed to be done here, moves the detector and the beamstop down. This should not have any influence on the measured GISAXS patterns, so the differences in the GISAXS patterns around 700 °C is likely to origin from changes in the sample itself.

5.3.1.2 Different incident angles

In order to investigate the influence on the GISAXS patterns by using different incident angles for the incoming X-ray beam, several measurements were made on the same sample, but varying the incident angle. The sample was made by dipping

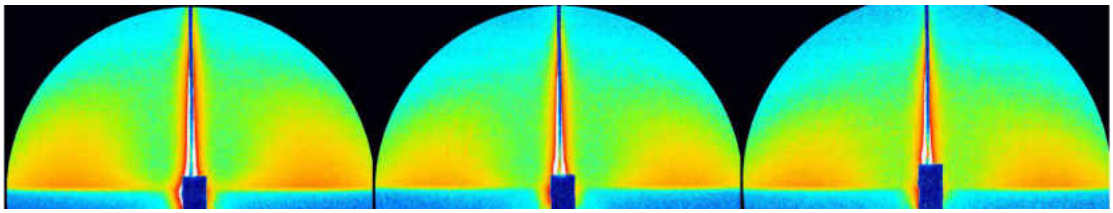

Figure 5.8: GISAXS measured at different incident angles, 0.258, 0.357 and 0.457 degrees, respectively, for zirconia coated silicon wafer (4 dips) heated to 500 °C *ex situ*.

a silicon wafer into the zirconia-sol four times, and dried in the furnace on the dip-coater machine at $\sim$ 120 °C for 60 seconds between each coating. Thereafter, it was heated to 500 °C in the lab furnace. The incident angle was varied for the GISAXS measurements of this sample, and these angles were: 0.257. 0.307, 0.357, 0.407 and 0.457 degrees.

It is useful to get an overview of how these angles relate to the critical angle. The critical angle calculated for this composition (ZrO_2), density (3800 kg/m^3) and X-ray energy (10 keV), is found to be $\alpha_c = 0.214°$ (Eqs. (2.46) and (2.62a)). For the smallest incident angle used, $\alpha_i/\alpha_c \approx 1.2$, and for the largest, $\alpha_i/\alpha_c \approx 2.1$. These values can be compared to figure 2.5, and it is observed that for the former a distinct proportion of the incoming beam is reflected, whilst for the latter nearly all of the incoming intensity is transmitted into the sample. A discussion about how to optimise the incident angles for probing the relevant sample depth was given in the last paragraph of Section 2.4.1.

Some of the resulting GISAXS patterns are shown in figure 5.8, and the horizontal cuts at the Yoneda angle are plotted in figure 5.9. The GISAXS patterns do not show any significant differences, and the only differences obvious in the

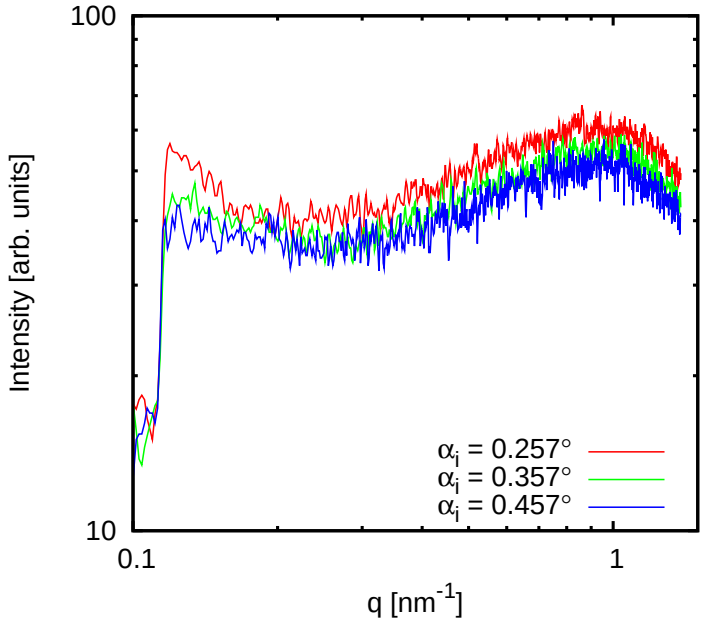

Figure 5.9: Cuts taken at the Yoneda angle, for the GISAXS measurements shown in figure 5.8.

1D-plots are the overall intensity and the extra intensity at low-q for the smallest incident angle. These results will be further discussed in Section 6.7.

5.4 X-ray diffraction

The crystal structure of the coatings can be investigated by performing X-ray diffraction measurements on the different samples at different temperatures. These measurements were performed as described in Section 3.3.3, and the resulting X-ray diffractograms are presented in this section. For investigating the crystal structure of the sample, the position of the Bragg peaks are important, and for just reading off these positions it is not necessary to subtract the background (*i.e.* the measurement of the clean substrate). Instead the background measurement

is shown together with the measurements of the coating present in order to distinguish which peaks originates from the substrate and from the sample. One of the main aims of the XRD measurements, was to look for phase transitions of the coating; these are typically well visible from the "raw" XRD data because different phases have different positions of Bragg peaks, or fewer or additional Bragg-peaks. Further discussions will be given in Section 6.3.

5.4.1 Coatings on mica

First, the crystal structure of the zirconia coating on the mica substrate was investigated; two different mica pieces have been coated with zirconia-sol and heated *ex situ*, one to 500 and one to 700 °C, respectively, and the X-ray diffractograms of these are shown in figure 5.10 (right panel). Figure 5.10 (left panel) shows the diffractogram of bare mica. It is here observed that the Bragg peaks originating from the coating in diffractogram from the measurement performed on the sample annealed at 500 °C has wider peaks than the diffractogram from the sample annealed at 700 °C. This is an indication of the crystalline domains being smaller when the sample is heated to 500 °C than when it is heated to 700 °C; this will be further discussed in Section 6.3.2.

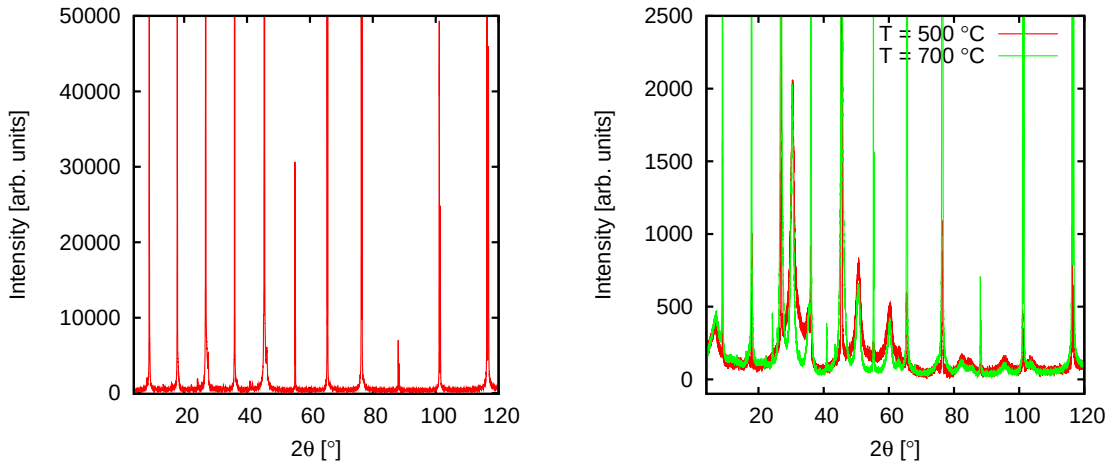

Figure 5.10: X-ray diffractograms. Left panel: bare mica. Right panel: two separate zirconia-sol coated mica pieces that have been heated *ex situ* to 500 and 700 °C, respectively.

5.4.2 Coatings on Si(100)

5.4.2.1 Comparing different coatings

In order to study the influence the yttria doping has on the crystal structure, diffractograms from the coatings containing varying amount of yttria, and dip-coated onto the silicon wafer, are plotted together.

The upper left panel in figure 5.11 shows the diffractogram of the clean silicon wafer. The other three panels show the diffractograms where the coated sample has been heated to different temperatures, 500, 700 and 900 °C, respectively. Each of these panels shows the different samples, such that differences can be compared for the relevant temperature.

By studying this figure (figure 5.11), it can be observed that the Bragg peaks originating from the coating (at $2\theta \approx 30, 35, 50, 60$ and $63°$) are wider the more yttria that is present in the coating. As previously mentioned, this width is an

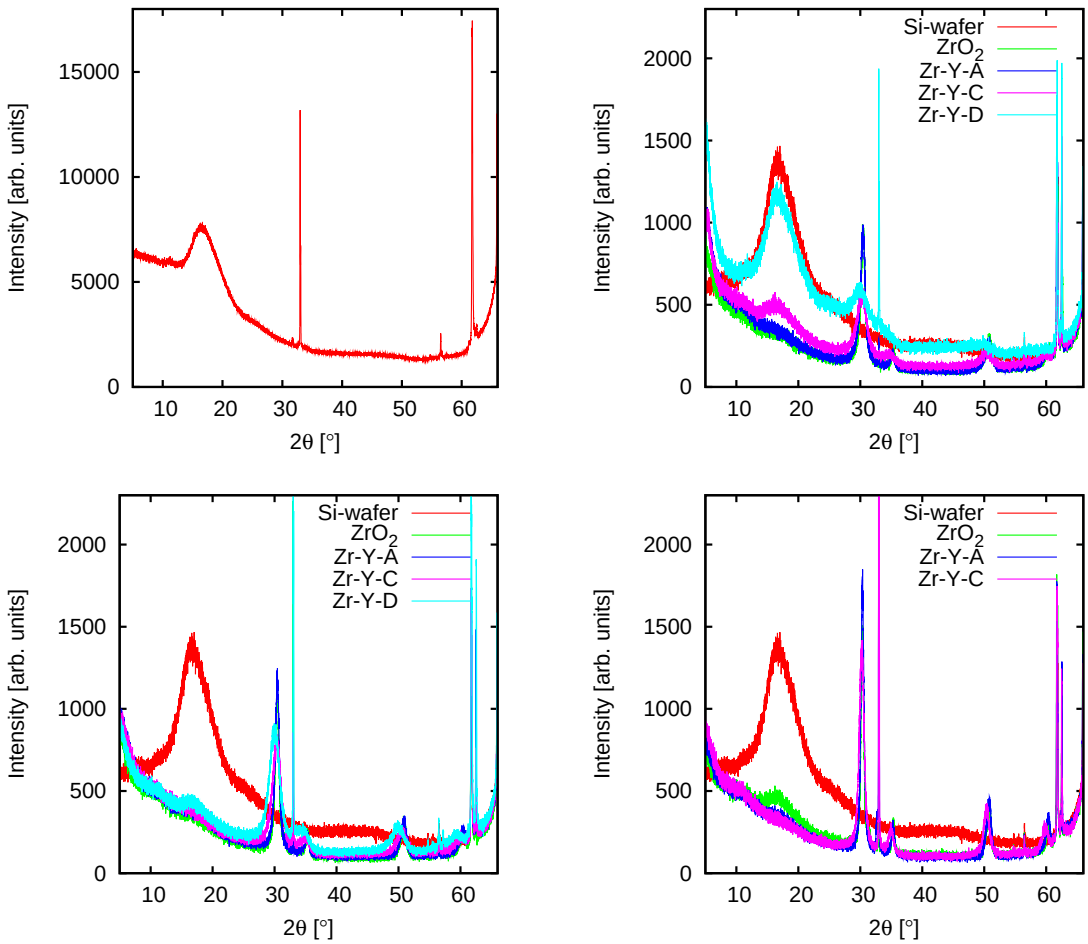

Figure 5.11: X-ray diffractograms. Upper left: Clean silicon wafer (not annealed). The remaining three panels shows samples which were annealed at 500 °C (upper right), 700 °C (bottom left) and 900 °C (bottom right) together with the diffractogram from the un-annealed silicon wafer.

indication on the size of the crystalline domains within the sample, so for the yttria concentrations investigated here, there seems to be a correlation between yttria content and size of the crystalline domains; the more yttria present, the smaller these domains are. These XRD results will be further discussed in Section 6.3.3.

5.4.2.2 Comparing different annealing temperatures

In order to compare the effect of different annealing temperatures for each sample, the diffractograms of the same sample, for different temperature, are shown in each panel of figure 5.12. It is here observed that the width of the Bragg peaks are smaller the higher temperature the sample has been annealed at. This is an indication of the crystals within the sample growing as the sample is heated; the connection between heat treatment and the size of the crystalline domains will be further discussed in Section 6.3.

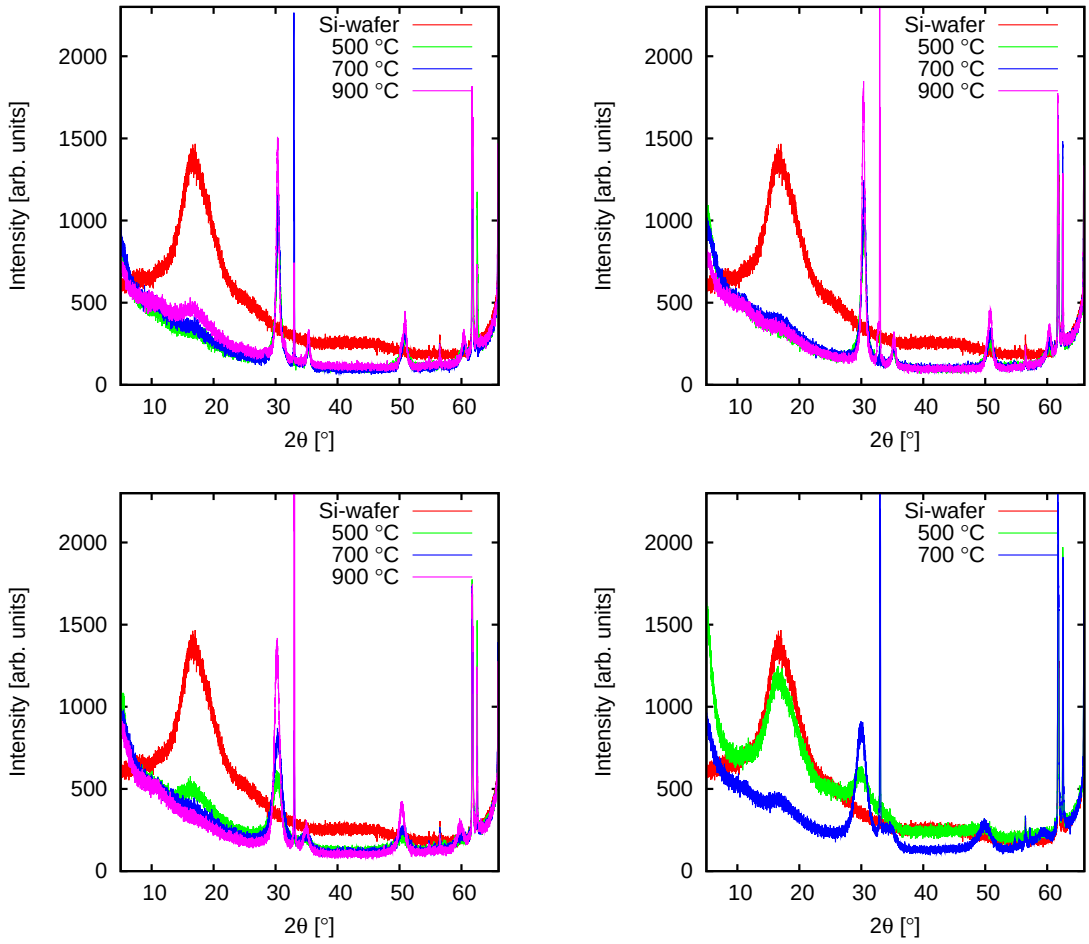

Figure 5.12: X-ray diffractograms of the bare and the coated Si(100)-wafers, where each panel shows the results from the different coatings: ZrO_2 (upper left), coating Zr-Y-A (upper right), coating Zr-Y-C (bottom left) and coating Zr-Y-D (bottom right). The effect of different annealing temperatures can now be investigated for each sample.

Summary

For the *in situ* dipping experiment, the 500 and the 700 °C measurements were showing distinctive differences; for the zirconia containing samples, the measurements at 500 °C show a distinct peak at the high-q end, where the position of this peak moves towards larger q-values as more dips are performed. The position and the width of this peak is different for the different samples.

For the measurements taken at 700 °C, not much is changing as the number of dips are increased. However, it is worth noting that since the intensities have not been scaled; the intensity does increase significantly as the number of dips increase.

For the *in situ* heating experiment, it was observed that for the pure zirconia samples, the pattern changed significantly in the temperature ranges
700 °C $\leq T \leq$ 900 °C and 550 °C $\leq T \leq$ 850 °C using SAXS and GISAXS, respectively. For the samples containing yttria, this change was found to be more gradual.

The XRD measurements do not show any crystal structure transitions, however, the Bragg peaks are found to be narrower as the annealing temperature is increased. This means that the crystalline domains increase in size with increased annealing temperature.

Chapter 6

Discussions

6.1 Introduction

In this chapter the results from the previous chapter are investigated and discussed in more detail, and useful information is extracted from these results; such as size, average separation distance and surface structure of the scattering objects. Furthermore, the crystal structure of the particles within the coatings, and the effect of yttria doping, are discussed. As expected, the *in situ* heating measurements are typically seen to produce rapidly changing patterns at each temperature, and it is not trivial to quantifiably compare these patterns. In order to do this, it is necessary to apply relevant models, and the application of such models are discussed here.

6.2 *In situ* heating

6.2.1 Thermal expansion coefficient of YSZ

The thermal expansion of the substrate and for the coatings was investigated in Section 3.3.2.3. It is now left to discuss the possible difference in thermal expansion for different yttria concentrations within the coatings.

Hayashi *et al.* published an interesting paper in 2005, titled "Thermal expansion coefficient of yttria stabilized zirconia for various yttria contents" [5], where they investigated the thermal expansion coefficient for the temperature range -170 to 603 °C using a push-rod type differential dilatometer and molecular dynamics simulations. This paper discusses which physical mechanism is the most important for the thermal expansion coefficient. For example, if the thermal expansion coefficient is dependent on the vacancies within the sample, then this would lead to a weaker binding energy within the system, and an *increased* thermal expansion coefficient for increasing yttria content. However, it seems like the bulk modulus is mainly responsible for the *observed decreased* thermal expansion coefficient as the yttria content is increased.

Hayashi *et al.* explains that as the yttria content is increased, an increased number of Y-O bonds are present in the sample. They Y-O distance is longer than the Zr-O distance ($\approx$ 0.23 and 0.21 nm, respectively), and this leads to an *increased lattice constant* within the YSZ crystal. However, due to displacement of oxygen ions towards the vacancies (recall figure 1.1), the Zr-O distance was

found to decrease with the increase of yttria. The authors further explain that the increase of binding energy due to decrease of Zr-O and Y-O distance is considered to be larger than the decrease of the binding energy due to the increase of oxygen vacancies. Furthermore, the decrease of the Zr-O and Y-O distances leads to an increase in the binding energy of YSZ with the increase of yttria concentration, and this results in decreasing thermal expansion coefficient.

6.2.2 Study the structural changes in the coatings

In situ experiments are very useful for studying the development of coatings during heating. As was shown in Chapter 5, the measured scattering patterns change significantly as the sample is heated, and this indicates that the sample itself is changing with increasing temperature.

The most obvious changes to the coating as it is heated, is expected to be the evaporation of organic residue from the sols, densification of the coating and the appearance of nanoscale crystals that grow as the temperature is increased. The latter assumption is a result that follows from the *in situ* heating SAXS experiment which showed the forming of a shoulder and a shift of this shoulder towards lower q-values for higher temperatures (figure 5.1). Such a shift corresponds to an increase in the size of scattering objects, and this growth may happen because the particles are agglomerating or because of Ostwald ripening.

Ostwald ripening A large number of small particles is energetically unfavourable because the energy of the system increases with surface area. This is because

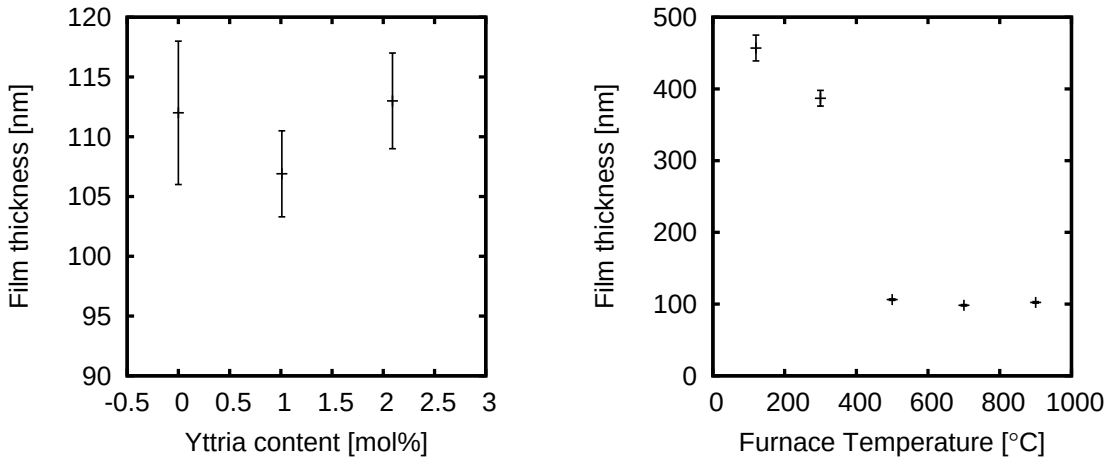

Figure 6.1: Thickness of coatings on Si(100) measured by ellipsometry. Left panel: the results for the samples containing different yttria contents (0 mol%: ZrO_2 coating, 2.04 mol%: coating A, 4.17 mol%: coating B) heated to 1000 °C. Right panel: five different zirconia coated Si-wafers heated one by one to different temperatures, and the plot shows the resulting film thickness for each.

molecules on the surface are energetically less stable than the ones in the interior of the particle. A reduction in the number of particles and increase in particle size, cause the overall energy of the system to decrease, and this situation is thus more favourable. Therefore, the dispersion coarsens or ripens ([71], p. 118), and this process is called Ostwald ripening after Wilhelm Ostwald who first explained it in 1896 [72]. The theory of Ostwald ripening is already thoroughly described elsewhere, see for example [71].

Densification As the film is heated it becomes denser; in order to investigate the film thickness as the sample is heated, the coated silicon wafers were studied by ellipsometry. The results for some of the coatings and firing temperatures are shown in figure 6.1. The film thickness was found to be almost independent of the

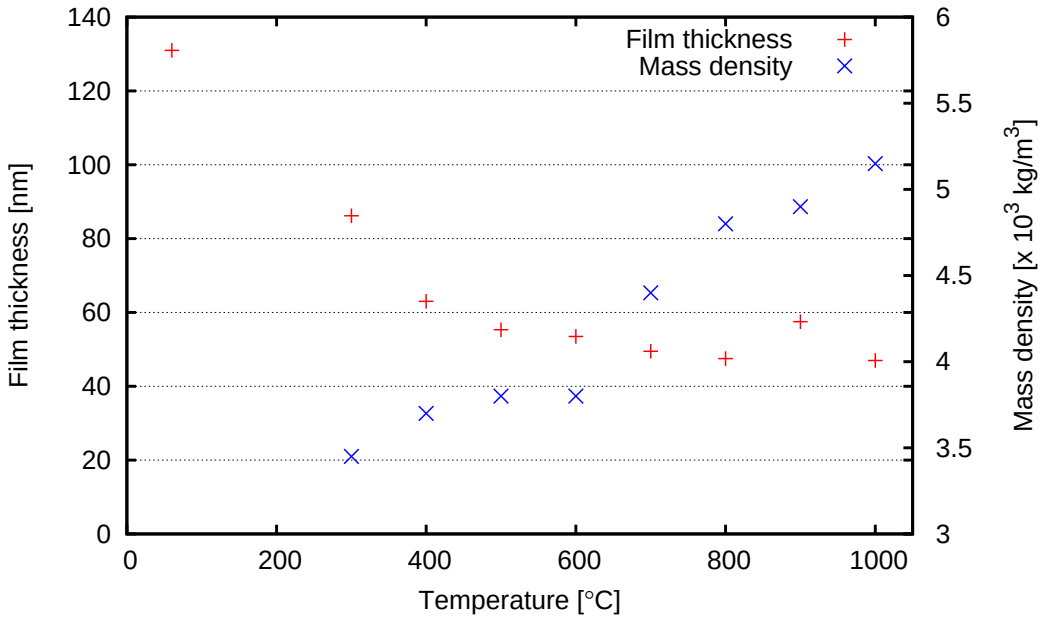

Figure 6.2: Firing temperature dependence of the thickness and mass density, as deduced from the X-ray reflectivity curves for a zirconia thin film on a sapphire wafer. Values obtained from [70].

yttria content, but strongly dependent on annealing temperature. This is because as the film becomes denser, it also becomes thinner.

The technique of X-ray reflectivity is very useful for determining the sample thickness, and also the mass density of the sample. The relevant mass density for each temperature was found by comparing with previous experiments conducted by Lenormand *et al.*[70] (see figure 6.2). These authors prepared zirconia films using similar methods to ours, and measured the thickness and mass density of the films as they were heated using X-ray reflectivity (XRR) measurements. The similarities worth mentioning in the comparison of Lenormand's results (figure 6.2) and ours (figure 6.1) is that at room temperature, the film is relatively thick, and then the film thickness decrease significantly in the area around 300-500 degrees.

After the temperature have reached 500 degrees, the thickness only decrease slowly. The rate at which the film thickness decrease, especially around 400 degrees, seems to be different in the two figures, and this is not surprising since the measurements were performed using different experimental techniques (X-ray reflectivity and ellipsometry) and since in the reflectivity experiment the sample was incrementally heated whilst in the ellipsometry experiment different samples (but with the same coating) were heated to different temperatures. This difference is not significant; the important message is that the film thickness decrease significantly in this temperature regime.

An assumption has now been made in that the mass densities obtained for the pure zirconia films can be used for the yttria-zirconia films, because the mass difference between yttrium- and zirconium atoms is small. For example, the mass difference between crystalline zirconia and sample C (19.1 mol% yttria) in crystalline form is less than 2 %. For the uncalcined films it would be even smaller because the film densities are lower than the density of the crystalline material.

Another point to mention is that no trends could be observed in the ellipsometry results for the film thickness of the different yttria concentration coatings (see figure 6.1 (left panel)). Since the mass density is related to the film thickness, we conclude that the different yttria concentrations have no significant influence on the mass density for these coatings.

Thermal analyses methods, such as thermogravimetric analysis (TGA) and differential scanning calorimetry (DSC), would also give useful information about

the sample as it is heated. These techniques have been employed by others, and for example, Chervin *et al.* measured TGA and DSC for zirconia aerogels. These authors found that the majority of the mass loss is below 400 °C, and it is mostly due to loss of water and residual organics. The remaining few percent mass loss (above 400 °C) is likely due to elimination of water as chemisorbed hydroxyl groups react to form additional M-O-M bonds [11].

6.2.2.1 Using GISAXS for studying these structural changes

When the temperature increases, the density also increase, which in turn cause δ and β to increase (see Eq. (2.62)). According to Eq. (2.46), the critical angle for the film, α_c, will also increase, and consequently the Yoneda feature will be observed at higher α_f (Eq. (2.45)). The surface of the film may become rougher, or islands may form and grow on the surface, although no cracking or delamination could be observed by eye as the temperature was increased. The novelty in this work is to be able to quantifiably analyse the GISAXS patterns despite the large changes in the GISAXS pattern due to changes to the sample, such as increasing Yoneda angle, changing surface roughness and increasing particle size.

From the expressions for δ and β (Eq. (2.62)), it is clear that knowing the mass density of the material is very useful for further analysis. The relevant mass densities are found in figure 6.2.

For example, for sample B heated to 1000 °C the film density is then $\rho = 5150$ kg/m^3 [70]. δ and β can now be calculated from Eq. (2.62) by setting $i = \{Zr\}, \{Y\}, \{O\}$ and n_i is taken from Table 3.1. The anomalous correction

factors, f' and f'', were found in Ref. [73] for $\lambda = 0.124$ nm; this is acceptable since the X-ray energy used here is far from any absorption edges. The results for this particular sample are found to be $\delta = 9.60 \cdot 10^{-6}$ and $\beta = 2.72 \cdot 10^{-7}$. The critical angle can now be found from Eq. (2.46), and for this sample it is $\alpha_c = 0.251°$. The film thickness was found from *ex situ* ellipsometry measurements, and these showed that the thickness of this film was $t = 113 \pm 4$ nm. The calculations mentioned above were performed using Octave [74], and the source code can be found in Appendix C.

During the heating experiment, the incident angle α_i was fixed to 0.257°. As seen in figure 4.7, the GISAXS patterns change significantly. The Yoneda feature moves slightly towards larger α_f as the sample is heated (see figure 5.4 (left panel)). The critical angle for the heated films has been calculated using Eq. (2.46), and for example, $\alpha_c(450°\text{C}) = 0.214°$ and $\alpha_c(950°\text{C}) = 0.248°$.

6.3 X-ray diffraction

As discussed in sections 2.1 and 2.5, crystals diffract X-rays because of the regular spacing between their lattice planes, and from the diffraction pattern, the crystal structure of the material can be determined. In this case, we are mostly interested in looking for phase transitions. In many cases, phase changes are obvious to see because the different phases cause a completely different diffraction pattern. In other cases, as for example elongation of the cubic unit cell to become tetragonal, the phase transitions may not be that obvious, we will discuss the reason for this

in this section, as well as discussing how to distinguish the monoclinic, tetragonal and cubic phases of zirconia.

In Section 2.5, an example was given about how to determine the positions of the Bragg peaks for a fcc arrangement of Zr-atoms. However, the material studied in this work is ZrO_2, and consequently the crystal structure of ZrO_2 will be used for the further simulations. The unit cell of the cubic phase was illustrated in figure 1.1, and it belongs to the space group $Fm\bar{3}m$ (No. 225). Tetragonal zirconia, however, belongs to the space group $P4_2/nmc$ (No. 137). The patterns for cubic and tetragonal zirconia are quite similar, but that for the monoclinic phase, space group $P2_1/c$ (No. 14), the pattern is completely different, see for example [8], and the monoclinic phase can thus be excluded as a candidate for the samples in this work. However, determining whether the crystal structure is cubic or tetragonal is a bit more complicated and further investigations are needed.

Recall how a table for the Bragg reflections was tabulated in table 2.1. This table is now continued, but this time using the "proper" crystal structure (space group $Fm\bar{3}m$ and $P4_2/nmc$). Of course it is more efficient to leave the calculations to the computer by now; here the Matlab program written by Dag W. Breiby called *simDiffraction* has been used [75]. The input for the computer program is the information about the crystal structure, and it is written in the format of a *cif*-file (crystallographic information framework), where the relevant coordinates and positions are taken from International Tables for Crystallography [76]. The following tables (Tables 6.1 and 6.1) were both generated using *simDiffraction*

Reflection (hkl)	q [Å^{-1}]	2θ [°]	$\lvert F_{hkl}\rvert^2$
(111)	2.119	30.12	27906
(002),(020),(200)	2.447	34.92	7659
(022),(202),(220)	3.461	50.21	11418
(113),(131),(311)	4.058	59.67	3887
(222)	4.239	62.62	1725

Table 6.1: Expected Bragg peaks from cubic zirconia (space group $Fm\bar{3}m$, No. 225) using lattice parameter a=5.135 Å.

Reflection (hkl)	q [Å^{-1}]	2θ [°]	$\lvert F_{hkl}\rvert^2$
(010),(100)	1.747	24.74	5671
(011),(101)	2.127	30.24	359680
(002)	2.427	34.63	193637
(110)	2.471	35.27	171944
(012),(102)	2.991	43.02	1556
(112)	3.464	50.26	105089
(020),(200)	3.495	50.73	106504
(120),(210)	3.907	57.24	315
(013),(103)	4.039	59.35	51453
(121),(211)	4.091	60.21	49240
(022),(202)	4.255	62.88	35360
(122),(212)	4.600	68.65	242

Table 6.2: Expected Bragg peaks from tetragonal zirconia (space group $P4_2/nmc$, No. 137) using lattice parameters $a = b = 3.596$ Å and $c = 5.177$ Å.

and the *cif*-file given in appendix D. The lattice parameters used here, were found in the literature; for cubic zirconia $a = 5.135$ Å [8], and for tetragonal zirconia $a = b = 3.596$ Å and $c = 5.177$ Å [77]. The wavelength used for the simulations was set to $\lambda = 1.5406$ Å (CuKα_1). Only the reflections where $F \neq 0$ are included in the table, and all the peaks between Bragg angle 0 and 70 degrees are listed.

SimDiffraction can also be used for plotting simulated XRD patterns, and the resulting patterns are shown in figure 6.3.

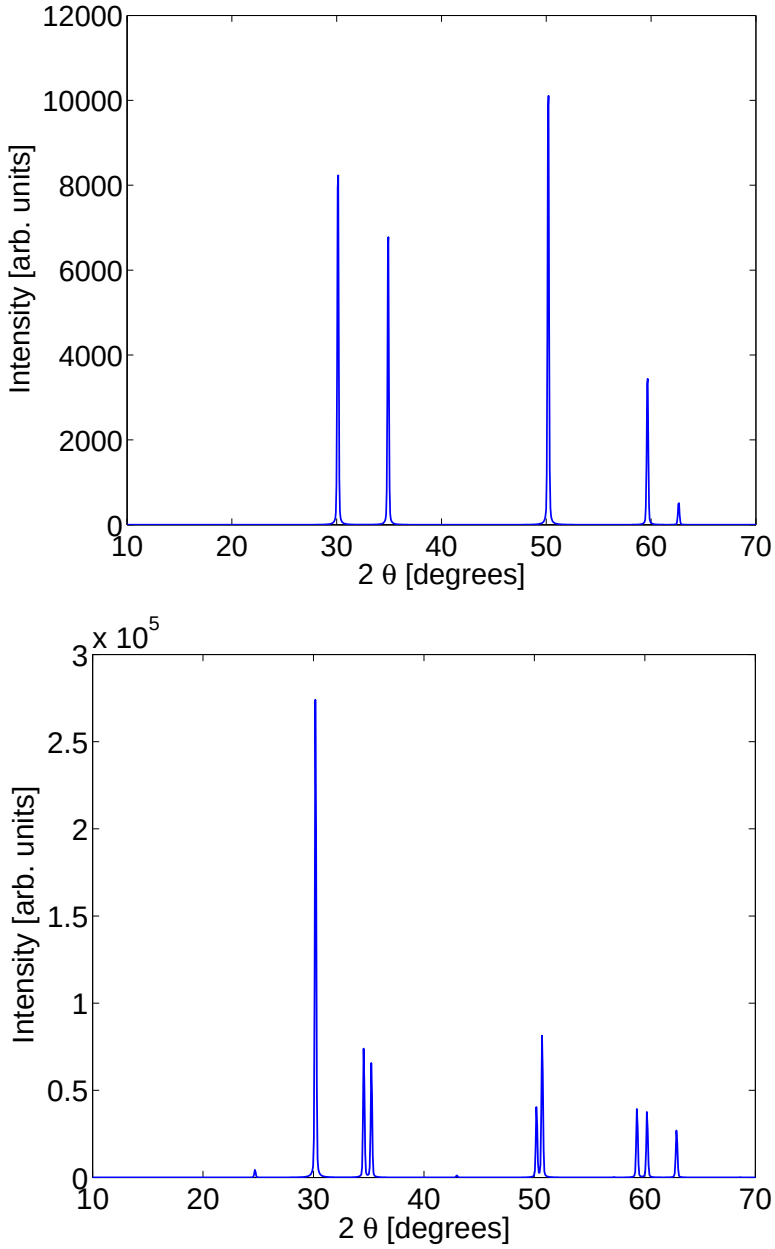

Figure 6.3: Simulated XRD patterns for zirconia. Top panel: Cubic zirconia, space group $Fm\bar{3}m$ (No. 225) with lattice parameter $a = 5.135$ Å. Bottom panel: Tetragonal zirconia, space group $P4_2/nmc$ (No. 137) with lattice parameters $a = b = 3.596$ Å and $c = 5.177$ Å.

6.3.1 Crystal structure

In order to study the crystal structure of the different samples and at different temperatures, the X-ray diffractograms shown in the figures 5.10, 5.11 and 5.12 were compared to the simulated diffraction patterns. However, care needs to be taken in the comparisons; if the crystalline particles within the sample are very small, the Bragg peaks will become wider, and in combination with experimental peak broadening, it may be that only one peak will be observed where theoretically a split peak would be expected.

For example, Chervin *et al.* measured XRD from zirconia aerogel calcined at 550 °C, and these authors found that: "The significant amount of peak broadening observed is due to the nanocrystalline nature of the calcined aerogel. The peak positions are in agreement with the reported reflections for cubic zirconia [...]. However, due to peak broadening and the similar peak positions for tetragonal ZrO_2, the diffraction pattern could also be indexed as tetragonal."

Other research groups have also discussed that it is difficult to distinguish whether the crystal structure of zirconia is cubic or tetragonal by XRD. If there are a small amount of tetragonal domains present amongst mostly cubic domains, XRD is not sensitive enough to pick up the signal from the tetragonal domains [83; 84; 11].

The calcium-fluorite structure that fits the space group $Fm\bar{3}m$ has long been taken as the correct model for cubic zirconia. However, the calcium-fluorite model has been modified because weak superlattice reflections and/or diffuse diffraction

were observed by electron diffraction, single crystal X-ray diffraction and neutron diffraction [15]. McClellan *et al.* found the modified space group to be $P\bar{4}3m$, where the oxygen sublattice of the cubic structure is distorted from $Fm\bar{3}m$, relative to the cation sublattice, by displacements along the [111] directions [82; 13]. But the exact structure of cubic YSZ is still much discussed [15].

6.3.2 Coating on mica

Consider the right hand panel of figure 5.10: First, select peaks that are due to the ZrO_2 coating, and not to the mica, and compare to figure 6.3. At first glance, the non-mica peaks in the measured pattern seem to fit well to the simulation for the cubic system (top panel). This zirconia coating is therefore interpreted as being mostly cubic for both the sample that was annealed at 500 °C and the sample that was annealed at 700 °C, but with the possibility of small tetragonal domains for reasons discussed in Section 6.3.1.

The peaks used for size determination are situated at $2\theta \simeq 30$, 50 and 60°. The instrumental broadening was estimated by fitting the individual mica peaks from the clean mica sample, and it was found to be practically independent of 2θ, and thus, $\beta_{instr} \simeq 0.0578$. The total line broadening observed is therefore the sum of the real and the instrumental line broadening; $\beta_{obs} = \beta + \beta_{instr}$, where β is the FWHM (full-width at half-maximum) value of the peak.

The size of the crystal particles were estimated, assuming cubic structure, using the Scherrer equation

$$t \approx \frac{K\lambda}{\beta \cos\theta_B}, \tag{6.1}$$

where K is a constant, depending on the shape of the crystallites. For example, Bragg derived a simplified derivation of the Scherrer equation where the crystallites were assumed to be platelets having p parallel diffraction planes; analogous to a stack of playing cards. Bragg's derivation results in $K = 0.89$ [78; 79], and this value was used in this work. λ is the wavelength of the X-rays, and for Cu Kα_1, $\lambda = 1.54056$ Å [80]. θ_B is the Bragg angle for the relevant peak, and β is the broadening of the diffraction line: $\beta = \beta_{obs} - \beta_{instr}$. β_{obs} and θ_B was found by curve fitting the relevant peak to a Lorentzian distribution function (if a Gaussian curve was used instead of Lorentzian, then the peak broadening should be calculated as $\beta^2 = \beta^2_{obs} - \beta^2_{instr}$ [81]). The average grain size is denoted by $\bar{t}$ (t is the depth of the "platelet", $t = p \cdot d$). Finally, the average of t found for the different peaks were averaged, and the result is; $\bar{t} = 6.34$ and $\bar{t} = 7.93$ nm for the sample that was heated to 500 and 700 °C, respectively, when the value of K was assumed to be 0.89.

6.3.3 Coating on Si(100)

Next, the samples prepared for the GISAXS experiment were investigated, and these diffractograms were shown in figure 5.11 and figure 5.12. Consider figure 5.11 first; none of the split peaks predicted for the tetragonal phase can be distinguished. However, the discussion in Section 6.3.1 still valid, it is here assumed

Temperature [°C]	ZrO_2	Zr-Y-A	Zr-Y-C	Zr-Y-D
500	9.70	8.46	3.72	1.79
700	11.6	10.4	4.07	4.20
900	16.3	14.5	8.48	-

Table 6.3: Crystal size ($\bar{t}$) in nm for the coatings on Si(100)-wafers annealed at different temperatures (*ex situ* measurements) estimated by Scherrer analysis. As expected, the crystal size increase with increased temperature. Interestingly, the crystal size generally decreases with increased yttria doping.

that this structure is mostly cubic, and this structure was found to be independent of temperature for the range 500 °C $\leq T \leq$ 900 °C. Figure 5.12 shows the temperature dependence of each sample. Again, none of the split peaks from a tetragonal structure are observed, and this mostly cubic structure is observed independent of yttria doping (for the samples investigated here).

Scherrer analysis was applied to these diffractograms; the peaks situated at $2\theta \simeq 30$, 35, 50 and 60° were used and the average value was taken from the result for the individual peaks. The results are listed in table 6.3.

An investigation of the lattice parameter would be interesting because the result would lead to better understanding of the effect that yttria doping is having on the crystal structure. In the case where the zirconia or yttria-doped zirconia coating has a cubic structure (the calcium-fluorite structure), the cell parameter a can easily be calculated from the measured data.

First, Eq. (2.87) is rearranged to isolate a

$$a = d_{hkl}\sqrt{h^2 + k^2 + l^2}, \tag{6.2}$$

Temperature [°C]	ZrO_2	Zr-Y-A	Zr-Y-C	Zr-Y-D
500	5.078	5.087	5.134	X
700	5.079	5.080	5.113	5.156
900	5.083	5.087	5.122	X

Table 6.4: The cell parameter a calculated from the XRD measurements, assuming the unit cell is cubic. Notice increased lattice parameter a for increased yttria content.

and Eq. (2.85) is rearranged to isolate d_{hkl}

$$d_{hkl} = \frac{\lambda}{2 \cdot \sin \theta_B}. \tag{6.3}$$

This result is used to substitute for d_{hkl} in Eq. (6.2). The lattice constant of a cubic crystal can thus be found by using that

$$a = \frac{\lambda}{2 \cdot \sin \theta_B} \sqrt{h^2 + k^2 + l^2}. \tag{6.4}$$

In the case of these XRD measurements, a was first calculated individually for the peaks situated at $2\theta \simeq 30$, 35, 50 and 60°, which in the case of a cubic crystal are the (111), (200), (220) and (311) reflections, respectively, and then the average of these values was calculated. This was repeated for each temperature and for different yttria concentrations. The result is shown in table 6.4, and it is interesting to note that the lattice parameter generally *increases* with increased yttria content, whilst any changes due to firing temperature is practically insignificant.

This means that our results agree with the results of Hayashi *et al.* (see Section 6.2.1); these authors found an increase in the lattice constant for increased yttria content in the YSZ, and this was explained by the increase of Y-O

bond lengths; since the Y-O distance (0.23 nm) is longer than the Zr-O distance (0.21 nm) [5]. These longer bond-lengths will result in a more disordered crystalline lattice within the samples containing more yttria.

6.4 Curve-fitting procedures

In order to get quantitative results out of the SAXS and GISAXS patterns, it is necessary to introduce curve-fitting procedures for the data. In this section it is discussed which model is most appropriate to these measurements, how to fit the model to the data and the validity of the models.

6.4.1 Guinier plots

One of the simplest curve-fitting methods is the procedure where the Guinier plots (log (I) *vs.* q^2) are used, and the procedure is described as follows: From Guinier's approximation given in Eq. (2.30) it is seen that

$$I(q) \propto \exp\left(-\frac{q^2 R_g^2}{3}\right), \tag{6.5}$$

and by taking the logarithm:

$$\log I = -\frac{q^2 R_g^2}{3 \ln 10} + C. \tag{6.6}$$

The slope of a $\log I$ *vs.* q^2 plot, a, is then

$$a = \frac{R_g^2}{3 \ln 10}. \tag{6.7}$$

By rearranging:

$$R_g = \sqrt{3a \ln 10}. \tag{6.8}$$

The radius of gyration can be found by plotting the SAXS pattern as a log (I) *vs.* q^2 plot and extracting the slope, a, of straight sections. This type of plot is called a Guinier plot.

6.4.1.1 Validity of Guinier's approximation

Guinier and Fournet (Ref. [19], p.128) show that for spherical objects, Guinier's approximation is only relevant when $qR_g \lesssim 1.3$. In the following it is investigated how large effect this limit has on the results.

Recall that the scattering intensity for dispersively packed particles is proportional to the particle form factor

$$I(q, r) = AF^2(q, r), \tag{6.9}$$

where A is the amplitude at $q = 0$ and the form factor $F(q, r)$ for a spherical particle of radius R is given by

$$F(q, R) = 3\frac{\sin(qR) - qR\cos(qR)}{(qR)^3}. \tag{6.10}$$

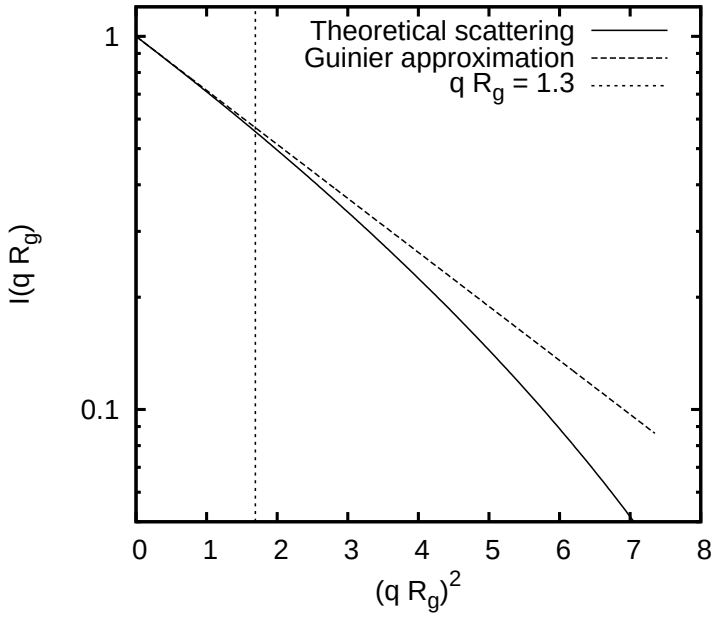

Figure 6.4: Figure illustrating the difference between the Guinier approximation (Eq. (6.12)) and the simulated SAXS curve from Eq. (6.11). The reason for why the Guinier approximation is only valid for $qR_g \lesssim 1.3$ (for spheres) is nicely illustrated in this figure.

Consequently, the simulated SAXS curve is then

$$I(q) = A\left(3\frac{\sin(qR) - qR\cos(qR)}{(qR)^3}\right)^2. \tag{6.11}$$

In order to illustrate the discrepancy between Guinier's approximation and the theoretical scattering pattern, a figure that shows $\log I(q)$ *vs.* $(qR_g)^2$ would be helpful. Since $R_g^2 = (3/5)R^2$ for spherical particles, $qR_g = \sqrt{(3/5)}qR$. The resulting curve is plotted as a solid line in figure 6.4.

The Guinier approximation is shown in figure 6.4 as the dashed line. This line is calculated for a scattering object using

$$I(q) = A \exp\left(-\frac{q^2 R_g^2}{3}\right) \tag{6.12}$$

where A again is the amplitude at $q = 0$.

In the results from the measurements discussed in this thesis, it was found that $q_{shoulder} R_g$ was commonly around 2, but may be as large as 3. Note that the ordinate in figure 6.4 is logarithmic; for example, for $qR_g = 3$, the difference in $I(qR_g)$ (and therefore the slope) is 281 %. For $qR_g = 2$, the difference is smaller: $\Delta I(qR_g) = 17.4$ %. However, from figure 6.4 it can be observed that the slope a from the Guinier plot always will have a lower value than the slope from the simulated scattering curve. From Eq. (6.8) it is then obvious that the radius of gyration obtained from the Guinier plots will always have a smaller value, or similar value, to the "real" value. By using the Guinier plots, a lower limit to the particle size can be obtained.

6.4.2 Beaucage's unified model

Another method of obtaining the particle size, is by using Beaucage's unified model as explained in Section 2.2.3, and applying it to the 1D patterns. This model is written as

$$I(q) = S(q) \cdot [G \exp(-q^2 R_g^2/3) + B\{[\mathrm{erf}(qR_g/\sqrt{6})]^3/q\}^P] \tag{6.13}$$

for one structural level. A structure factor $S(q)$, is needed in order to account

for interference effects from more densely packed particles (see Section 2.2.2.3).

The first term within the square parenthesis in Eq. (6.13) is labelled as the Guinier term, and the second term the Porod term.

6.4.3 Modelling the data

A system containing spherical particles can be modelled using Eq. (6.11) and implementing the log-normal particle size distribution (Eq. (2.18); this was illustrated in figure 2.2). The simulated curve can then be compared with the data.

For the first measurement performed at 950 °C on the zirconia-coated mica (the Bessy SAXS experiment) the radius of gyration obtained from the unified model analysis was found to be $R_g = 12.61$ nm ($R = 16.28$ nm if spherical particles). This value for R was used in Eq. (6.11) and plotted using different values for σ. For example, $\sigma = 0.37$ was found to give a reasonable fitting curve for $q > q_{shoulder}$; this simulation is shown in figure 6.5.

The lower intensity in the measured curve than in the simulated curve for $q < q_{shoulder}$ can be explained by the interference effects from more densely packed particles, and can be corrected for using a structure factor, such as Eq. (2.36).

6.4.4 Comparing models

Guinier's approximation has also been applied to the measurement discussed in figure 6.5 (not shown), even though $q_{shoulder}R_g > 1.3$, with the result $R_g = 10.78$ nm ($R = 13.91$ nm if spherical particles). It was noted that a straight line does indeed

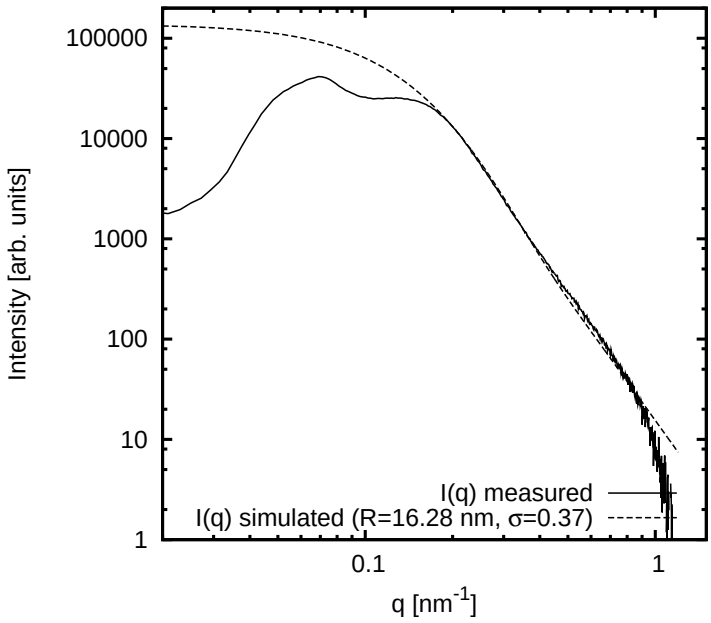

Figure 6.5: Full line: Zirconia-coated mica (SAXS, Bessy), 950 °C, No. 1. Dashed line: Eq. (6.11) using a log-normal size distribution (Eq. (2.18)) with $R_{median} = 16.28$ nm ($R_g = 12.61$ nm), $\sigma = 0.37$ and $\mu = \ln R + \sigma^2$.

fit the data for a short range at low q-values, but since qR_g is outside the allowed regime, this slope is not directly correlated with R_g as indicated in Eq. (6.8).

Because of its restrictions, the Guinier approximation is not a good method for accurately obtaining the particle sizes. On the other hand, the unified model does not have such restrictions; it is valid for the entire q-range, and it gives realistic values for R_g compared to the simulated SAXS pattern for spherical particles.

In conclusion, the unified model is a better model for small-angle scattering patterns. However, it can be tricky to apply and therefore Guinier's approximation is useful for finding the lower limit of the particle sizes, and thus mapping the trends in, for example, *in situ* experiments.

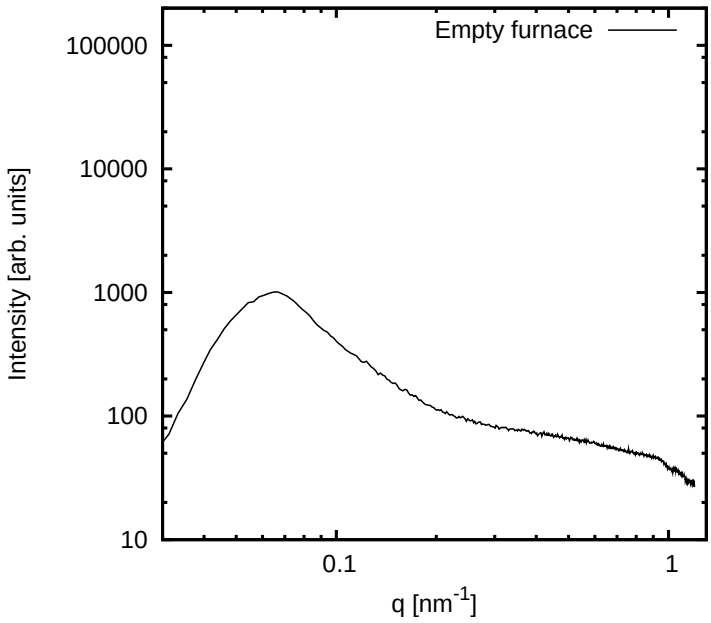

Figure 6.6: The background measurement for the experiment where the zirconia coated mica was heated. This is the measurement of the empty furnace. Notice the shoulder at $q = 0.94$ nm^{-1}.

6.5 Fitting models to the data

6.5.1 SAXS: Zirconia on mica, *in situ* heating

The data from the experiment performed at Bessy, where a piece of mica was coated with zirconia-sol, and heated *in situ*, was analysed using the procedure described in Section 4.2.1, and Beaucage's unified model was fitted to the resulting patterns.

A background measurement of the empty furnace was also performed, and the result is shown in figure 6.6. In this figure a shoulder is observed at $q = 0.94$ nm^{-1}. Therefore, for the measurements where the sample is present, after the subtraction of the background data, a shoulder is observed around $q = 0.94$ nm^{-1}. Conse-

Subset	Temperature [°C]	Levels	$S(q)$	Fit range label	Fit range (q) [nm^{-1}]
I	≤ 650	1	1	a	0.1-1
	700		1	b	0.1-0.3
II	750-800	2	Eq. (2.36)		0.1-1
III	850	1	Eq. (2.36)	a	0.18-1
	900-950			b	0.12-1
	950			c	0.1-1

Table 6.5: Table summing up how the unified model (as Eq. (6.13)) was used for the zirconia coated mica sample, for different temperature ranges.

quently, this feature does not originate from a scattering particle, but from the background subtraction.

The basics of the unified model was explained in Section 2.2.3. As the sample was heated, large changes in the scattering pattern was observed between 700 and 900 °C. Different subsets of the unified model needed to be employed in order to get as good results as possible; these subsets are listed in table 6.5. The term *subset* here means the rules for how different fitting parameters and constraints were applied, such as number of structural levels to be used, whether the structure factor S should be one or using Eq. (2.36), and the fit-range on the q-axis that should be used. For example, for the measurements taken for at 750 °C and higher, the structure factor was needed in the form of Eq. (2.36), in order for the model to fit the data.

Optimally, there should be an overlap between the neighbouring subsets (as for example, fitting subset (II) to the 700 °C data), in order to ensure continuity. However, for this experiment, the changes was so large in the temperature range 700 and 900 °C, that the data for these measurements could not be fitted by any

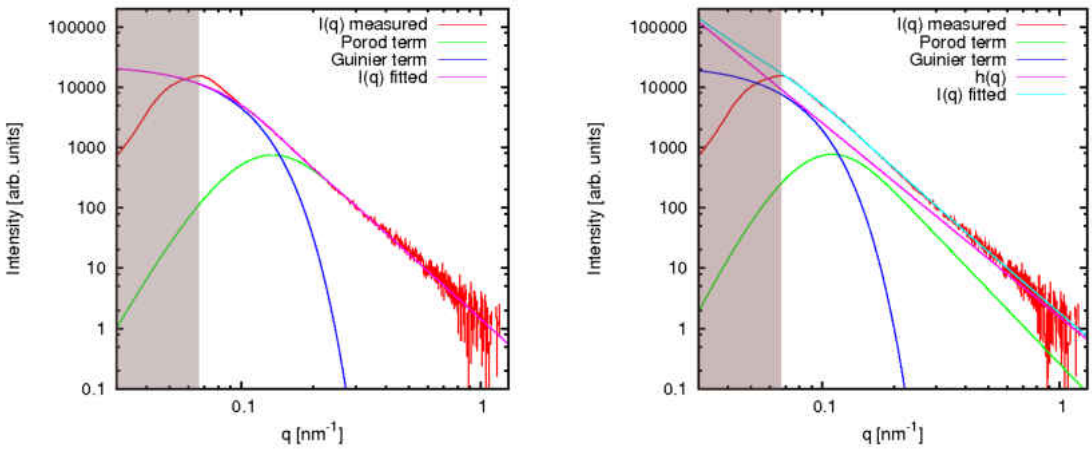

Figure 6.7: Left: The unified model (subset I-a) fitted to the SAXS pattern measured when the zirconia coated mica was heated to 450 °C. Right: Introducing a term to correct for the extra intensity at low q-values. The shaded area corresponds to the detector area behind the beamstop.

other subset. Only the first measurement at 950 °C was fitted by both (III-b) and (III-c). In the following, examples are given on how each subset was used in order to obtain quantitative results from the data set.

As an example, figure 6.7 illustrates how subset (I) of the unified model was applied to the data from the 450 °C measurement. This subset was only fitted to the data at the range 0.1 nm^{-1} $\leq q \leq$ 1 nm^{-1}. However, some extra intensity at low q-values is observed, and this is likely to be the contribution from larger particles. But because the beamstop is shading for any intensity at lower q, not enough data is obtained in this region in order to get information about the particle size of these.

6.5.1.1 Adapting the unified model for limited q-range.

As mentioned in section 2.2.3, fitting the measured data for the entire q-range is possible in theory. Our measurements only extends over a limited q-range, and suitable adaptions to the unified model are needed. By writing out Eq. (2.40) for two structural levels ($n = 2$)

$$\begin{aligned} I(q) \quad &= G_0 \exp(-q^2 R_{g,0}^2/3) + B_0 \exp(-q^2 R_{g,1}^2/3) \times \{[\mathrm{erf}(qR_{g,0}/\sqrt{6})]^3/q\}^{P_0} \\ &+ G_1 \exp(-q^2 R_{g,1}^2/3) + B_1 \exp(-q^2 R_{g,2}^2/3) \times \{[\mathrm{erf}(qR_{g,1}/\sqrt{6})]^3/q\}^{P_1} \end{aligned} \tag{6.14}$$

and consider the largest structural level first, I_0, for the case where $R_{g,1}$ is small and $R_{g,0}$ large:

$$\lim_{R_{g,1}\to 0} I_0(q) = G_0 \exp(-q^2 R_{g,0}^2/3) + B_0\{[\mathrm{erf}(qR_{g,0}/\sqrt{6})]^3/q\}^{P_0} \tag{6.15}$$

and

$$\lim_{R_{g,0}\to large} I_0(q) = 0 + B_0\{1/q\}^{P_0} = B_0 q^{-P_0}. \tag{6.16}$$

The measurements where this extra intensity at low q-values are observed, can thus be described by

$$I(q) \approx B_0 q^{-P_0} + G_1 \exp(-q^2 R_{g,1}^2/3) + B_1\{[\mathrm{erf}(qR_{g,1}/\sqrt{6})]^3/q\}^{P_1}. \qquad (6.17)$$

The right hand panel of figure 6.7 shows this equation fitted to the data by letting B_0, P_0, G_1, $R_{g,1}$, B_1 and P_1 float. Unfortunately, this is not a good fit, as the fitting uncertainty for each parameter is rather large. For example, $R_{g,1} = (27.4 \pm 2.2)$ nm (8 %) and $P_1 = (4.1 \pm 0.6)$ (15 %), and the corresponding values obtained from using subset (I-a) are $R_{g,1} = (22.3 \pm 0.1)$ nm (0.45 %) and $P_1 = (3.59 \pm 0.02)$ (0.69 %). It appears that using Eq. (6.17) for the fitting procedure produce overdetermined fits, and is therefore not a suitable method; this is why subset (I) has been chosen for fitting to the data at this temperature range.

Subset (II) (see table 6.5) is used for fitting to the measurements where the signal from two types of particles are present, and information can be extracted for both types. A structure factor (Eq. (2.36)) had to be included for the smaller particle type. For example, the data for the measurement taken at 750 °C, and subset (II) fitted to this data, is shown in figure 6.8. The relevant parameters extracted from this fit is listed in table 6.6, in the top row ($0.1\ \mathrm{nm}^{-1} \leq q \leq 1\ \mathrm{nm}^{-1}$). The uncertainties of the fit parameters are relative large, and therefore each structural level was investigated individually for a restricted q-range in order to compare the methods. The results obtained by fitting only one structural level, *i.e.*, using the procedure of subset (I), in the range $0.1\ \mathrm{nm}^{-1} \leq q \leq 0.3\ \mathrm{nm}^{-1}$, is

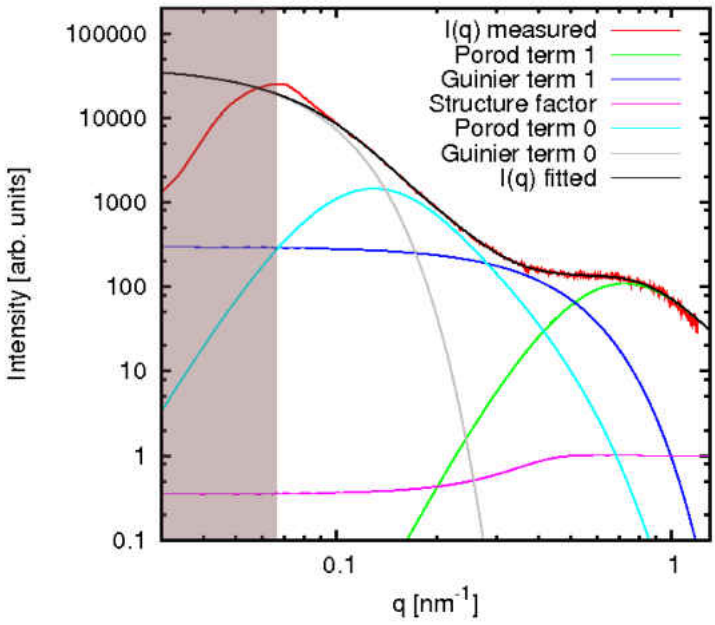

Figure 6.8: The unified model (subset II) fitted to the SAXS pattern measured when the zirconia coated mica was heated to 750 °C.

			Structural level 1		*Structural level 2*	
	q-range [nm^{-1}]		$R_{g,1}$	P_1	$R_{g,2}$	P_2
Subset (II)	0.1-1	value	22.7 nm	3.40	4.15 nm	3.82
		uncertainty (abs.)	0.2 nm	0.23	0.38 nm	1.45
		uncertainty (rel.)	1 %	7 %	9 %	38 %
Subset (I)	0.1-0.3	value	22.3 nm	3.36		
		uncertainty (abs.)	0.3 nm	0.07		
		uncertainty (rel.)	1 %	2 %		
	0.4-1.19	value			4.13 nm	4.31
		uncertainty (abs.)			0.02 nm	0.07
		uncertainty (rel.)			0.4 %	2 %

Table 6.6: Table listing the resulting values from fitting the unified model to the measurement taken at 750 °C.

listed in the middle row of table 6.6; for the the range 0.4 nm$^{-1} \leq q \leq$ 1.19 nm^{-1} the resulting values are listed in the bottom row of this table.

The values obtained for P_1, $R_{g,1}$, P_2 and $R_{g,2}$ were found to be similar for both methods. However, the uncertainty for the fitting values are larger by using sub-

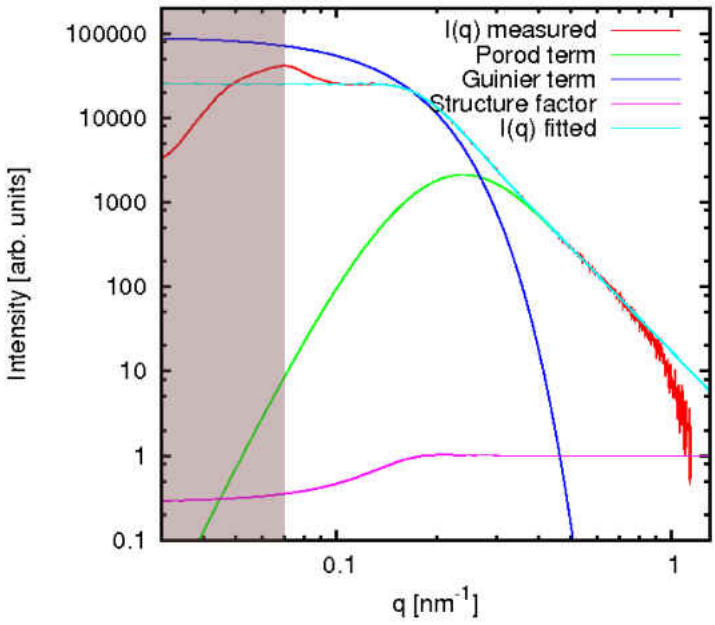

Figure 6.9: The unified model (subset III-a) fitted to the first measurement of the SAXS pattern after the zirconia coated mica was heated to 950 °C. The shoulder at the high-q end originates from the background subtraction (see figure 6.6).

set (II). Subset (II) is anyway used for this temperature range because the entire q-range may be fitted, instead of splitting up the fitting ranges. In the case of this experiment, the extra intensity at low q-values was not included in the fit - using the same arguments as for subset (I), *i.e.*, the entire q-range was not fitted, but most of it, excluding the extra intensity at low q-values.

Subset (III) (see table 6.5) is used for fitting to the measurements where information from only one particle type can be obtained. In order to get the model fit to the data, a structure factor was included (Eq. (2.36)). An example of this subset used on the data is shown in figure 6.9 for the first measurement taken at 950 °C (*cf.* figure 6.5). Also in this measurement, extra intensity is observed at

low q-values. This was again excluded, for reasons already discussed.

All of the different temperature measurements were fitted to the unified equation using one of the three subsets defined in table 6.5. The results obtained for the radii of gyration is plotted in figure 6.10, and the results for the Porod slope is plotted in figure 6.11.

At low temperatures one structural level is observed, and the radius of gyration for this type of particle remains relatively constant at around 25 nm, and it disappears at $\sim$ 800 °C. At 750 °C, another smaller type of particle appears. This particle type grows as the sample is heated further, and it continues to grow as the temperature is kept constant at 950 °C (measurement No. 15 and onwards), although for the last few measurements the particle growth appears to have stopped.

For the temperatures up to and including 700 °C, $P_1 \lesssim 4$. This means that the surface structure of the scattering objects remain relatively smooth. For the measurement taken at 750 °C, the Porod slope of the small emerging particle type was very difficult to fit, since the shoulder corresponding to this particle type is positioned at the high-q end of the pattern, and not enough of the straight slope necessary to determine the Porod slope appeared on the pattern. For the measurements taken at temperatures above 750 °C, the Porod slope first appear to be rather steep, but these may also be explained by that not enough data are obtained at the high-q end of the pattern.

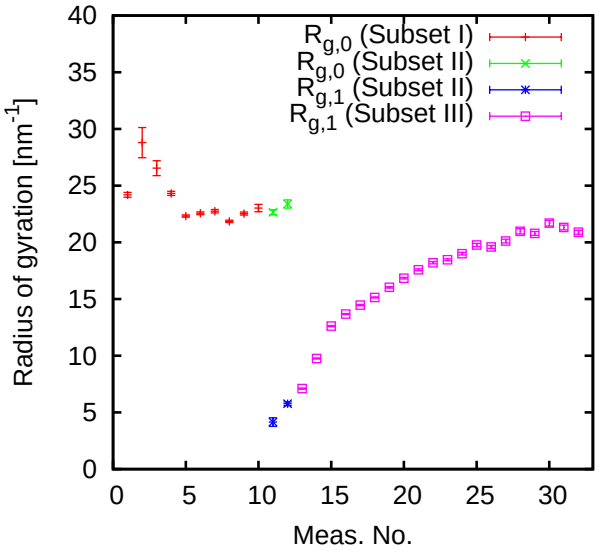

T [°C]	*Meas. No.*
Ambient	1
300	2
350	3
400	4
450	5
500	6
550	7
600	8
650	9
700	10
750	11
800	12
850	13
900	14
950	≥15

Figure 6.10: Radius of gyration obtained from the SAXS measurements on the *in situ* heated zirconia coated mica.

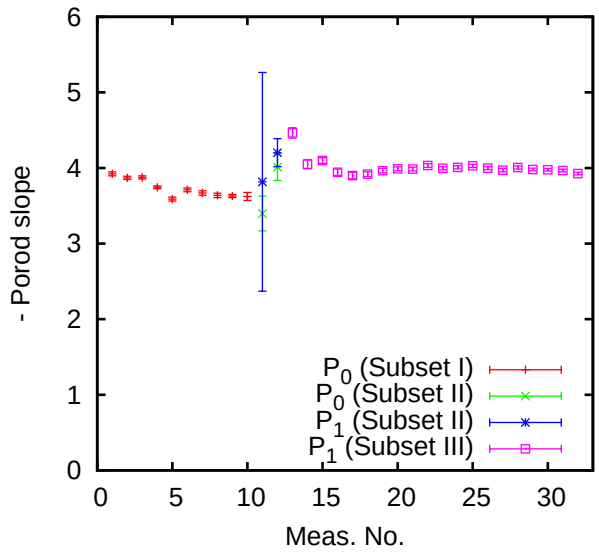

T [°C]	*Meas. No.*
Ambient	1
300	2
350	3
400	4
450	5
500	6
550	7
600	8
650	9
700	10
750	11
800	12
850	13
900	14
950	≥15

Figure 6.11: Porod slopes obtained from the same measurements as in figure 6.10. The surface structure of the particles is smooth at $T \leq 700$ °C and $T \geq 900$ °C. For the interval in between, the Porod slope could not be accurately determined, and thus no certain information is obtained for the surface structure of the particles in this temperature range.

As this particle type continue to grow, more and more of the Porod slope is revealed, and for the temperature 950 °C and above, a Porod slope very close to -4 is found. This means that the surface structure of the particles in this temperature range is smooth.

6.5.2 SAXS: *in situ* dip-coating experiment

For some industrial purposes it is important that coatings either do not contain pores, or contains a well-defined fraction of pores. Unless special chemical precursors have been used in addition to alcohol during the gelation stage, the gel itself will often crack and crumble as the network shrinks [18]. This cracking will lead to pores, which remains when the heat treatment of the sample is started. After cycles of dipping and heating has been performed, the samples look as they are porous. The evolution of the pores during calcination is not clear, and investigating these is one of the aims for this experiment.

We are suggesting that the formation and evolution of pores as dipping-and-heating cycles are performed can be studied by SAXS in an *in situ* dipping experiment. In addition to study the pore evolution, the more general aim of this experiment is to obtain a better understanding the nano-scale structural changes during dipping and heating cycles.

6.5.2.1 Different annealing temperatures

Coating B: 700 °C The SAXS patterns were corrected as explained in Chapter 4, and the unified model was fitted to the resulting curves. The q-range was restricted such that the pattern showed a linear slope at low-q and one feature corresponding to the small-angle scattering from one structural level. This feature is very distinct in these measurements, which means that the scattered beams from the scattering objects within the sample interferes, and therefore a structure factor is needed to correct for this. The discussion in section 6.5.1.1 is valid here, and thus the unified model is given by Eq. (6.18), where the subscripts indicate which structural level it applies to:

$$\begin{aligned} I(q) \quad &= B_0 q^{-P_0} \\ &+ S_1(q) \times \left(G_1 \exp(-q^2 R_{g,1}^2/3) + B_1 \{[\mathrm{erf}(qR_{g,1}/\sqrt{6})]^3/q\}^{P_1} \right). \end{aligned} \tag{6.18}$$

The unified model (Eq. (6.18), with $S(q)$ from Eq. (2.36)) was fitted to the measured data, and an example is shown in figure 6.12. The values for G_1, B_1, $R_{g,1}$, P_1 *etc.* obtained from these fits are shown in figure 6.13.

The figures in the top panel of figure 6.13, are showing the values obtained for G_1 and B_1 as function of *No. of dips*. In both cases these values increase significantly with increased number of dips. The relationship between these results

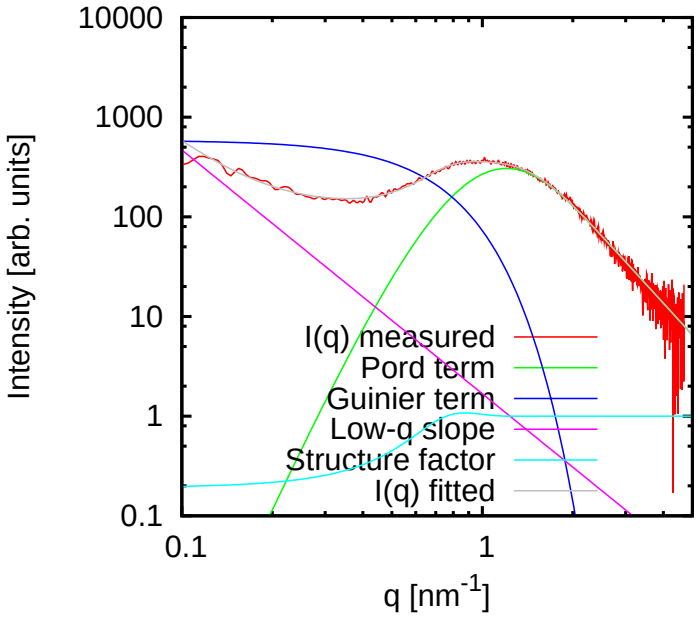

Figure 6.12: Illustration on how the unified model is used on the SAXS measurement taken on coating B at 700 °C (13 dips).

and the number of dips is therefore of interest; we wish to determine the functions $G_1(x)$ and $B_1(x)$ where x denotes *No. of dips*.

For $G_1(x)$, the power law

$$G(x) = A \cdot x^b + C \tag{6.19}$$

was found to give the best fit to the experimental data, and this is shown in figure 6.13, top left panel. Recall Eq. (2.38),

$$G = N_p V_p^2 \rho_e^2 = N_p n_e^2, \tag{Eq. (2.38)}$$

where N_p is the number of scattering particles in the measured volume, V_p is the volume of a scattering particle, and $\rho_e = n_e/V_p$ is the electron density. n_e is

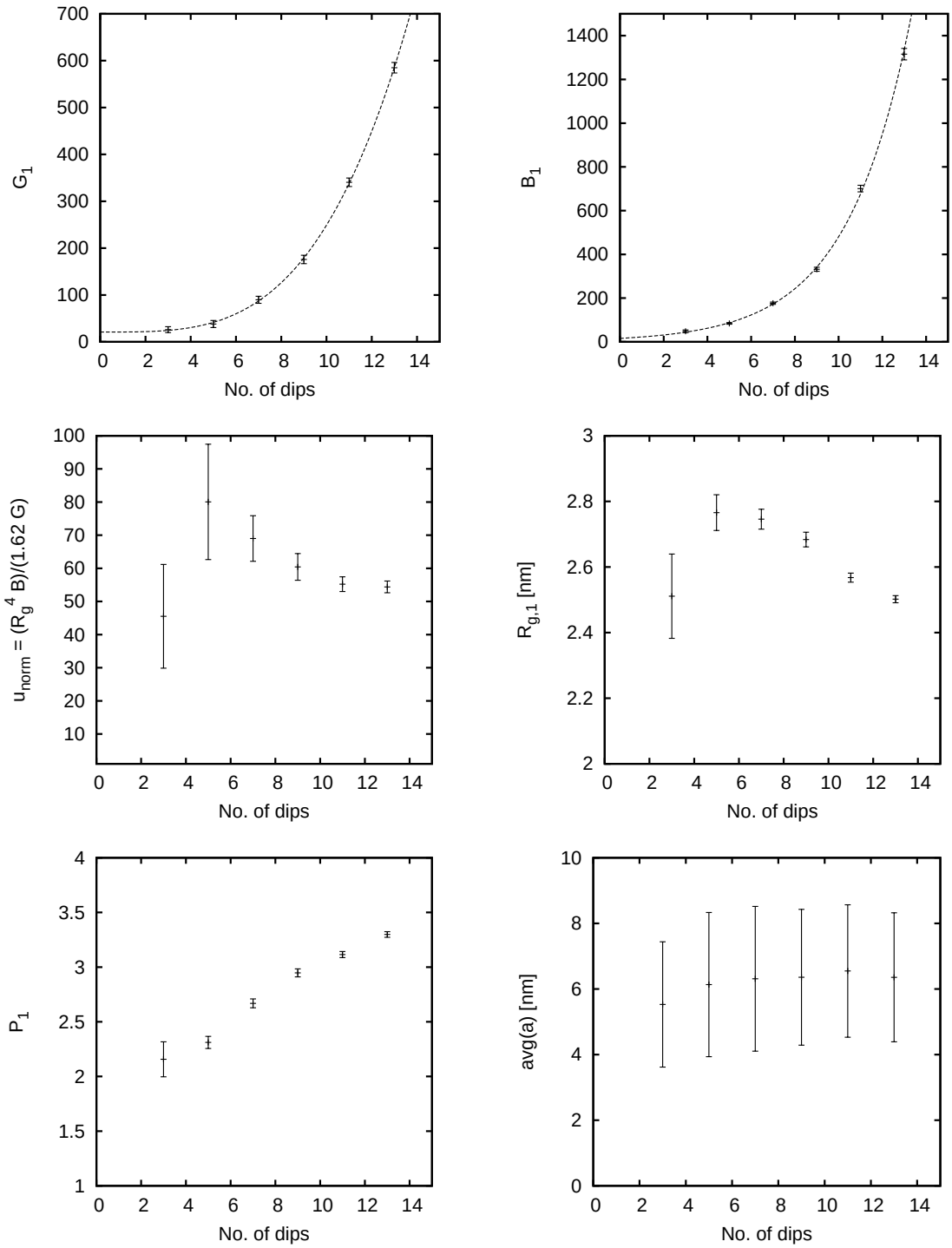

Figure 6.13: Figure showing how the different fit parameters vary with the number of dips, for the measurements on the Zr-Y-B coating. The error bars (except for in the bottom right panel) are the fitting uncertainties. Top panel: The prefactors G_1 and B_1 in the unified equation (Eq. (6.18)). Middle panel u_{norm} (described in text) and radius of gyration ($R_{g,1}$). Bottom panel: Porod slope (-P_1) and average separation distance between scattering objects ($\bar{a}$) where the plotted error-bars in the last panel are the value found for w (see Eq. (2.36)).

the number of electrons in the scattering particle.

The question is now which parameters G depends on. From the SAXS measurements (see figure 5.2 (right panel) and figure 6.13 (middle right)), a nearly constant value of $R_{g,1}$ is obtained. Since

$$R_{g,1} \approx const. \Rightarrow V_p \approx const.$$

and G is thus practically independent of V_p. The electron density within the particles ρ_e can also be approximated to be constant;

$$\rho_e \approx const.$$

By implementing this into Eq. (2.38), the behaviour of $G(x)$ is found to be

$$G(x) \propto N_p. \tag{6.20}$$

Consequently, the observed value G_1 will follow the behaviour of N_p, the number of scattering particles. N_p as a function of dip-coated layers, can be calculated as shown below. The first line originates by using that $G(x) \propto N_p$ (Eq. (6.20)) and $G(x) = A \cdot x^b + C$ (Eq. (6.19)).

$$N_p(x) \propto A \cdot x^b + C \tag{6.21}$$

$$= k \cdot (A \cdot x^b + C) \tag{6.22}$$

$$= k \cdot A \cdot x^b + C' \tag{6.23}$$

where k is a constant of proportionality, and $C' = k \cdot C$. By moving C' to the left hand side of the equal sign,

$$N_p(x) - C' = k \cdot A \cdot x^b \tag{6.24}$$

$$N_p(x) - C' \propto x^b. \tag{6.25}$$

And by moving C' back to the right hand side of the equal sign, the following result is obtained;

$$N_p(x) \propto x^b + C'. \tag{6.26}$$

Consequently, the number of scattering particles increases with a power of b for the number of dips. This can be explained by each dip taking up more of the sol than the previous one.

Next, the discussion above is repeated for B_1. For $B_1(x)$, the exponential function,

$$B(x) = A \cdot \exp(b \cdot x), \tag{6.27}$$

was found to give the best fit to the experimental data, and this is shown in figure 6.13, top right panel. The value of B_1 consequently increase exponentially with the number of dips.

Recall Eq. (2.39),

$$B = 2\pi N_p \rho_e^2 S_p, \tag{Eq. (2.39)}$$

where S_p is the surface area for the particle. Since an exponential fitted the B_1-values best, whilst a power law fitted the G_1-values best, it was concluded that there is something else that varies with the number of layers for B_1 than just N_p (as was found for G_1). Combining Eqs. (2.38) and (2.39), it is found that B and G are related by

$$B = 2\pi \frac{S_p}{V_p^2} G. \tag{6.28}$$

A changing surface-to-volume ratio for these scattering pattern will cause G_1 and B_1 to vary with different rates. Since G_1 and B_1 were found to follow slightly different trends; power law and exponential increase, respectively, the surface-to-volume ratio does indeed change with the number of dips.

By investigating the surface-to-volume ratio, additional information can be

obtained about the particles within the sample, for example the roughness of the particle surface (see [27]). But first, a discussion on how the surface-to-volume ratio can be found from SAXS patterns is needed.

In order to investigate the behaviour of the surface-to-volume ratio, Eq. (6.28) is rearranged to

$$\frac{S_p}{V_p^2} = \frac{B_i(x)}{2\pi G_i(x)} \equiv u(x). \tag{6.29}$$

This means that $u(x)$ is the value found for $B_i/(2\pi G_i)$ as a function of dipping layers, where i indicates the structural level ($i = 1$ was used in the discussion above). For example, if the scattering objects are assumed to be smooth spheres with radius R, surface area $S_p = 4\pi R^2$ and volume $V_p = (4/3)\pi R^3$ [27],

$$u_{sphere} = \frac{9}{4\pi R^4} = \frac{1}{2\pi}\frac{81}{50R_g^4} = \frac{1.62}{2\pi R_g^4} \tag{6.30}$$

The measured value of u, can be found by using that

$$u_{meas} = \frac{B}{2\pi G} \tag{6.31}$$

(from Eq. (6.29)). These values can be normalised to u_{sphere},

$$u_{norm} = \frac{u_{meas}}{u_{sphere}} = \frac{R_g^4 B}{1.62G}, \tag{6.32}$$

and the result is plotted in figure 6.13 (middle left hand panel). The meaning of the values of u_{norm} is discussed in [27], and a table of calculated values are

Distribution	u_{norm}
Monodisperse spheres	1.00
Block distribution	1.41
Intercept Porod/Guinier	3
Log-normal self-preserving continuum regime	4.93
Log-normal self-preserving free-molecular regime	5.56
Log-normal (spheres)	$\exp(12\sigma^2)$
Most probable	8.70
Debye-Bucche function	9.88

Table 6.7: The value of u_{norm} calculated for different particle distributions. Note that all numbers are less than 10. The values in this table is from [27] and for further details see this paper and references therein.

shown in table 6.7.

The values found for u_{norm} in our experiment (figure 6.13, middle left hand panel), are noticeably larger than the values in table 6.7. From Eqs. (6.29), (6.31) and (6.32), we see that a large values of u_{norm} means that the scattering particles are having a large surface area compared to the volume.

The radius of gyration obtained from the fits are shown in figure 6.13 (middle right hand panel). These values for R_g seems to roughly follow trend of the u_{norm}-values. This makes sense, since large values of u_{norm} correspond to particles that are having large surface area. It is therefore not surprising that the values for R_g follows u_{norm} in this case.

Figure 6.13 (bottom left hand panel) shows the Porod slopes obtained in the fits. Most of the measured Porod slopes are having values between -2 and -3, and these values are to be expected if the particles are mass fractals (see Section 2.2.2.2). Since the fitted value of P is increasing for the increasing numbers of layers, this tells us that the surface structure of the scattering particles are

becoming smoother with increasing number of layers.

Figure 6.13 (bottom right hand panel) shows the average separation distance between scattering particles, $\bar{a}$, as it was obtained from fitting the unified equation (Eq. (6.13)) with structure factor from Eq. (2.36) to the data. The plotted error-bars are the value obtained for w from the curve-fits (see Eq. (2.36)).

Coating B: 500 °C The result of this experiment was shown in figure 5.2 (left panel). A straight slope is observed at low q-values, which corresponds to a particle type that is too large for extracting information about the particle size. At the high q-end, however, a very distinct feature is observed. This peak is too sharp be a small-angle scattering peak; it has more similarities with a broad Bragg peak. None of the models for small-angle scattering fits these data, and another model is needed.

The hypothesis for this system, is a gradual transition of these coatings from a polymer structure based on a hydrocarbon backbone to one with a Zr-O-Zr backbone. At 500 °C many of the organic chain molecules will probably have evaporated, but some of these are left in the porous low-density zirconia-"polymer".

The strongest scatterers in this system are still yttrium- and zirconium atoms, and the hydrocarbon backbone can probably be ignored at first. The large peak at high q-values could be the correlation from the distribution of the yttrium- and zirconium atoms, spaced out by polymer chain molecules and pores.

The correlation length of the yttrium- and zirconium atoms can be found by considering Eq. (2.88) for $n = 1$ (*i.e.* the first order peak):

$$d_{corr} = \frac{2\pi}{q}. \tag{6.33}$$

The peak is for example positioned at $q = 4$ nm^{-1} for the measurement on a thick coating and the corresponding correlation length is thus $d_{corr} = 1.6$ nm.

The next step is to estimate the size of the precursor molecules and the subsequent packing density, and test if the result is in accordance with the result for the correlation length obtained above. The discussion below is only carried out for zirconium, for the Zr-Y-{A,B} solutions, as the yttrium atoms cannot be distinguished from zirconium atoms, and since there are so few yttrium atoms in the solution compared to zirconium atoms.

A rough estimate of the size of the precursor molecule ($Zr(OCH_2CH_2CH_3)_4$) was made using the bond lengths, C-H: 0.11, C-C: 0.15, C-O: 0.14 [85] and Zr-O: 0.21 nm [5]. The bond angles were estimated to be 105° at the O-atom (because of the lone electron pairs on the oxygen atom), and 110° at the C-atom because this angle will be close to the tetrahedral angle. This gives a resulting molecule size of 1.24 nm. The network is thus less dense than densely packed precursor molecules, and consequently, additional spacers are caused by porosity and/or organic chain molecules.

Figure 6.14 (left panel) shows the position of the peak as function of number of dips. Apart from the first point, which was not possible to determine with any accuracy, the peak is positioned at increasing q-value as the number of dips increase. The correlation length for each of these points was calculated using

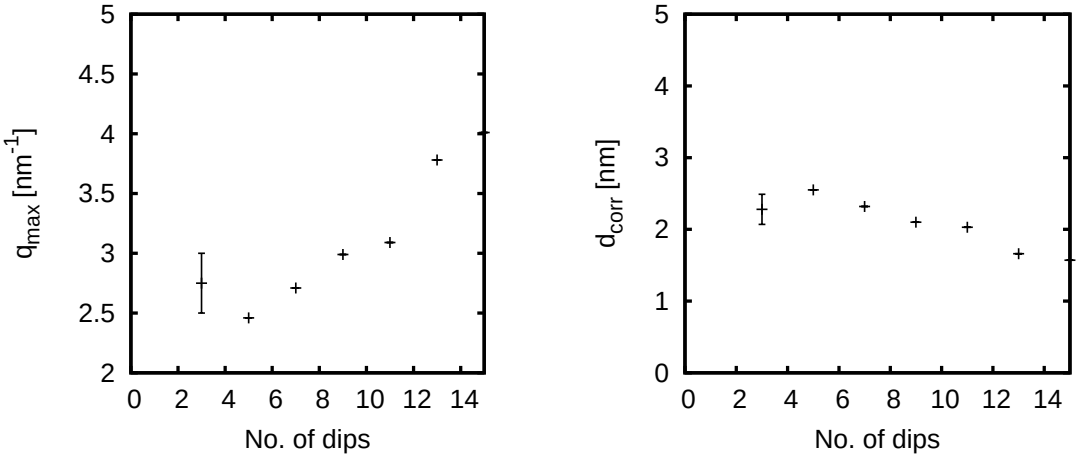

Figure 6.14: *In situ* dip-coating experiment for coating B, at furnace temperature 500 °C. Left panel: peak position plotted as function of dips. Right panel: Correlation length calculated using Eq. (6.33) plotted as function of dips.

Eq. (6.33), and the result is shown in figure 6.14 (right panel).

An initial hypothesis may be that the decreasing correlation length could be interpreted as decreasing porosity as the number of dips increases. However, the fact that more sol stuck to the substrate/sample than for the previous dip (see Eq. (6.26)) also needs to be taken into account. Another consideration is that different amounts of precursor molecules have probably undergone the gelation reactions as the number of dips increases, and then a different averaged correlation length would be measured. This means that the porosity is not directly correlated with the correlation length, and the initial hypothesis is not correct. Consequently, the chemical reactions for the dipping-and-heating cycle need to be investigated.

The sol was produced as described in section 3.2.2, and it is liquid, *i.e.*, not gelled, when the dip-coating is performed. The gelation process takes place when the sol is deposited on the substrate, and the solvents evaporate as the substrate

is withdrawn from the sol.

Recall the sol-gel theory in Section 1.2, and especially Eqs. (1.1) and (1.2), which indicate how the network is formed from the precursors. The important number here is the distance between Zr-atoms. In the reaction in Eq. (1.2) it is seen that the Zr-atoms are bound by an intermediate oxygen atom: Zr - O - Zr. The angle at the oxygen atom is $\approx 105°$, and the Zr - O bond length is 0.21 nm. Using these values in the law of cosines, the distance between two Zr-atoms becomes 0.33 nm, and for a dense ZrO_2 ceramic this would be the case.

For the polymer case considered here, the system has gelled and formed a network, but it has still not condensed into the ZrO_2 ceramic. The organic residue, or the pores remaining after these molecules have evaporated, prevents the Zr-atoms from stacking as closely as they otherwise would, and this supports the hypothesis about the porous low-density zirconia-"polymer" proposed in the beginning of this section.

From figure 6.14 (right panel) it was found that the correlation length decreases slightly with number of dipping-and-heating cycles. This may either be because more of the precursor molecules have undergone these reactions, or because the coating has become less porous. Since the porosity is not directly correlated with the correlation length, a quantitative result for the porosity can therefore not be obtained.

In summary, for the coatings heated to 500 °C, the broad Bragg peak indicates a semi-regular network of the Zr- or Y-atoms. The correlation distance found from

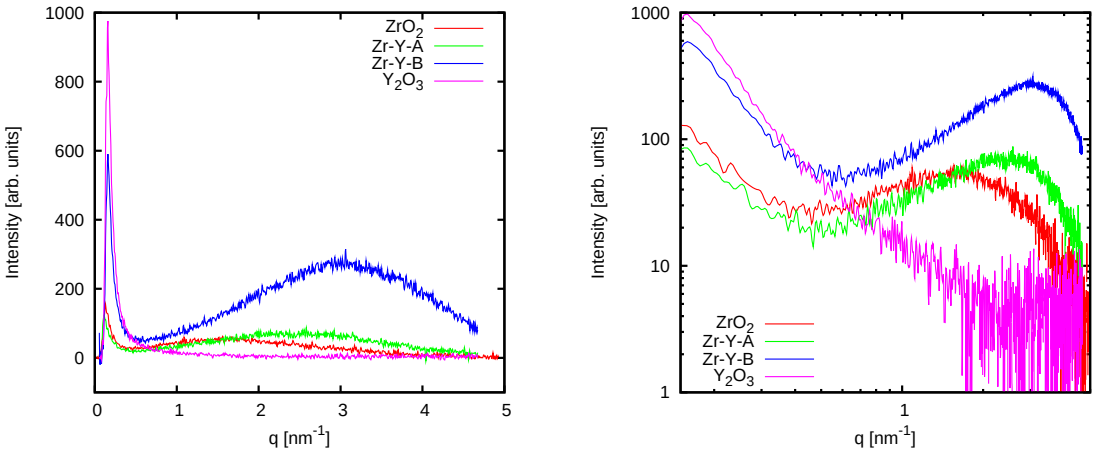

Figure 6.15: SAXS pattern after 11 dips for the sols containing different amount of yttrium. Left: linear scaling. Right: logarithmic scaling.

the measurements is around 1.6 nm which is clearly longer than the theoretical Zr - O - Zr distance (for a dense ZrO_2 ceramic). The Zr- or Y-atoms are therefore positioned further apart by all the remaining organic chain molecules and/or porosity in the coating.

6.5.2.2 Different coatings on mica

The results for the experiments for the coatings containing different yttria concentration and heated to ≈ 500 °C, was shown in figure 5.3. In order to compare these results, the measurement for 11 dips for each of the samples are plotted together in figure 6.15. This figure shows the zirconia-sol coating have a wide Bragg peak, which correspond to a semi-regular ordering of the Zr-atoms in the polymer network. As yttrium is added, the maximum of this peak moves towards larger q-values, and gets more pronounced.

The peak in figure 6.15 is interesting because it is not clear why the metal ions

would have a well-defined spacing. The shift of the peak position towards larger q-values and the increased intensity for increased yttria content indicates that the distribution of Zr- and Y-atoms becomes more ordered and that the correlation length decreases. For the coating that consists entirely of yttria-sol, no structure or small-angle scattering features are observed, which means that no ordering or any scattering particles in the observable range are present.

From the discussion in Section 6.5.2.1, it may follow that for the yttrium-doped coatings, more of the gelation process has taken place. The higher yttrium doping level (except for the pure Y_2O_3-coating), the smaller correlation length, and therefore more of the gelation process have taken place.

6.5.3 GISAXS: Coating B on silicon, *in situ* heating

The GISAXS patterns were corrected as explained in Chapter 4, and the unified model was fitted to the resulting curves. In this case the q-range is restricted such that the pattern shows a linear slope at low-q and one shoulder corresponding to the small-angle scattering from one structural level. The discussion in Section 6.5.1.1 is valid here, and thus the unified model is given by Eq. (6.34), where the subscripts indicate which structural level it applies to:

$$I(q) = B_0 q^{-P_0} + S_1(q) \times \left(G_1 \exp(-q^2 R_{g,1}^2/3) + B_1 \{[\mathrm{erf}(qR_{g,1}/\sqrt{6})]^3/q\}^{P_1} \right) + C. \quad (6.34)$$

The first term describes the low-q behaviour (level 0), with prefactor B_0, and where P_0 is the slope of this line when plotted on a log (I) *vs.* log (q) plot. The second term describes the next structural level (level 1): the first term within the parentheses is the Guinier term and the last term is the Porod term, with prefactors G_1 and B_1, respectively. $R_{g,1}$ is the median radius of gyration; it gives information about the size of the scattering particles at level 1. P_1 is the Porod slope for the same level, giving information about the roughness of the particle surfaces. C is a constant background contribution. The reason for introducing C here as a fit parameter, is that for the GISAXS experiments the background could not be measured accurately, but it is known that there is a constant background contribution present in the measured GISAXS patterns [61].

For sample B, the background parameter C could not be resolved properly for the lowest temperatures. For sample A, however, the value of C was successfully obtained from the fits for most of the temperature range. The value obtained for C was plotted as a function of T (in figure 6.16), and it was found to follow a linear trend with a low slope. This fitted line was used for estimating $C(T)$ for

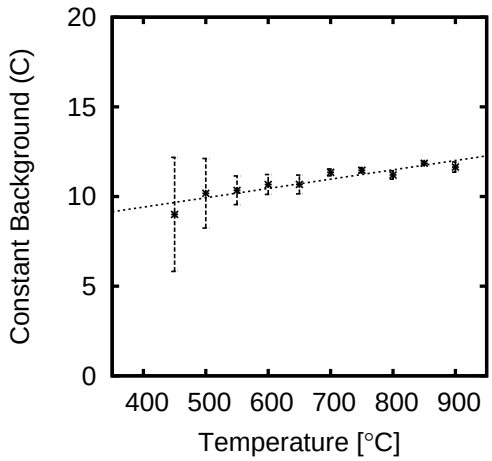

Figure 6.16: Fitted value for the constant background, C, for sample A. The straight line is described by $C(T) = 0.00519 \cdot T + 7.33$. [61]

sample B, where it has been assumed that the slope of $C(T)$ is the same for both samples.

Eq. (6.34) was fitted to all measurements for the different temperatures on sample B. Since the changes of the system are significant, the same model does not apply adequately to the whole experiment. Therefore, appropriate subsets for different (and overlapping) regimes are used (see Table 6.8) instead of one unique model that would be overdetermined for part of the series of data sets. The overlap in regimes is to ensure continuity between the subsets. The reason for different fit ranges is that the beamstop covered a wider region of q for the second and third temperature regime. Moreover, including $S(q)$ as Eq. (2.36) for the first regime produced overdetermined fits. The constant background parameter C could be fitted for the third temperature regime because there is a sufficiently long flat region at high-q, and therefore C has been included as a fit parameter in this regime. [61]

Regime	Temperature [°C]	Fit range (q) [nm^{-1}]	$S(q)$	Background (C)
1^{st}	400-550	0.027-1.38	1	$C(T) = 0.00519 \cdot T + 3.77$
2^{nd}	550-750	0.12-1.38	Eq. (2.36)	$C(T) = 0.00519 \cdot T + 3.77$
3^{rd}	750-1000	0.12-1.38	Eq. (2.36)	Fitted

Table 6.8: Table summing up how the unified model (Eq. (6.34)) was used for the Zr-Y-B coating for the different temperature ranges.

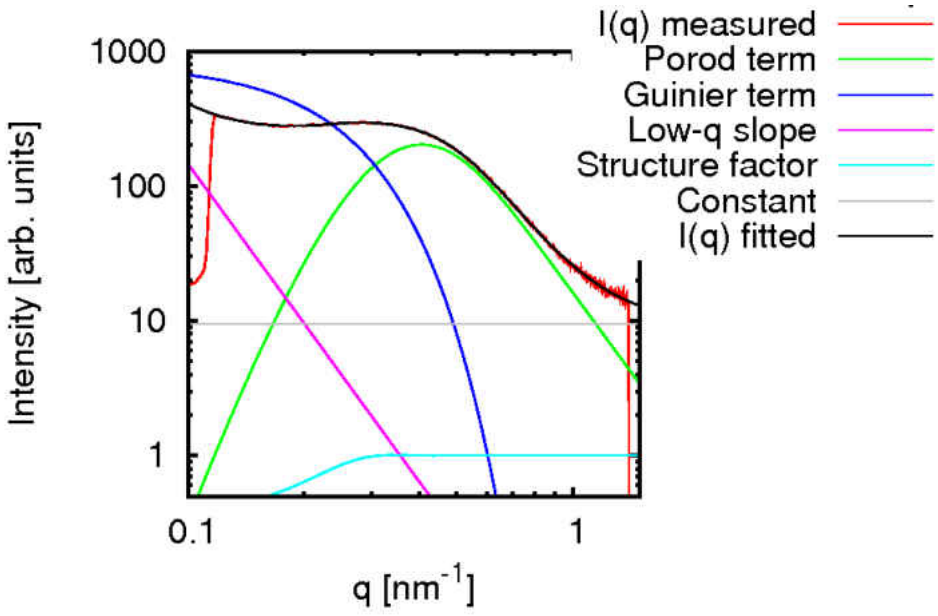

Figure 6.17: Illustration on how the unified model (Eq. (6.34)) was fitted to the GISAXS data taken at 800 °C, using the subset for the third temperature regime. All the parameters were fitted simultaneously.

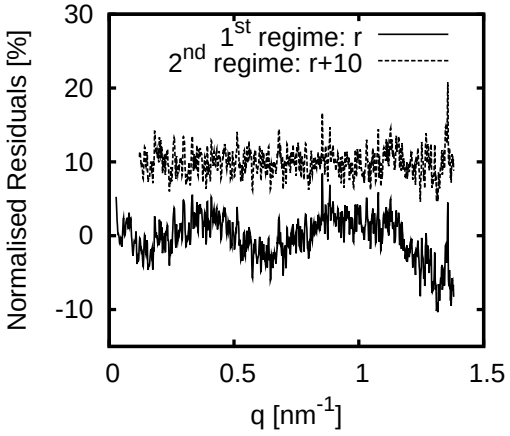

Figure 6.18: The normalised residuals, r, calculated for the first and second fit regime procedures, for the measurement performed at 550 °C. [61]

An example on the application of the unified model is shown in Figure 6.17. These data were measured at 800 °C, and the subset for the third temperature regime was used. This means that the unified model takes the form

$$I(q) = B_0 q^{-P_0} + S_1(q) \times \left(G_1 \exp(-q^2 R_{g,1}^2/3) + B_1 \{[\mathrm{erf}(qR_{g,1}/\sqrt{6})]^3/q\}^{P_1} \right) + C \qquad \text{(Eq. (6.34))}$$

where

$$S(q) = \frac{1 - \exp(-2w^2q^2)}{1 - 2\exp(-w^2q^2)\cos(q\bar{a}) + \exp(-2w^2q^2)}, \qquad \text{(Eq. (2.36))}$$

and it was fitted to the q-range from 0.12 and 1.38 nm^{-1} whilst all the parameters, $B_0, P_0, w, \bar{a}, G_1, R_{g,1}, B_1, P_1$ and C, were allowed to float.

As previously mentioned, different subsets of the unified model had to be used for different temperatures. In the example above, the subset for the third temperature regime was found to give the best fit. Indeed, for all the temperatures between 750 and 1000 °C, this subset was found to give the best fit result. For the measurement taken at 750 °C, it was found that both the subsets for the second and the third temperature regime could be used. The subset of the second regime was then used for temperatures between 550 and 750 °C.

If in doubt on which subset that will be the most appropriate, the different subsets can be tested by plotting the normalised residuals. For example, for the measurement performed at 550 °C, the appropriate subset could not easily be determined by looking at the fits, and consequently, the normalised residuals of the the first and second subset from the measured data were plotted in figure 6.18. From this figure it is clear that the second subset fits the data better, and this fit is shown in figure 6.19. For the temperatures below 550 °C, however, the first subset was found to give the best results.

Figure 6.20 shows the resulting radii of gyration, $R_{g,1}$ (a), Porod slopes, $-P_1$ (b), and average distances between scattering objects, $\bar{a}$ (c), for sample B. The increase in radius of gyration tells us that the size of the scattering particles increases as the sample is heated. As already mentioned, the Porod slope gives information about the surface structure of the particles; see Section 2.2.2.2 for a reminder. For the temperatures up to and including 550 °C, the Porod slope is between -1 and -3, which corresponds to the particles being mass fractals. The

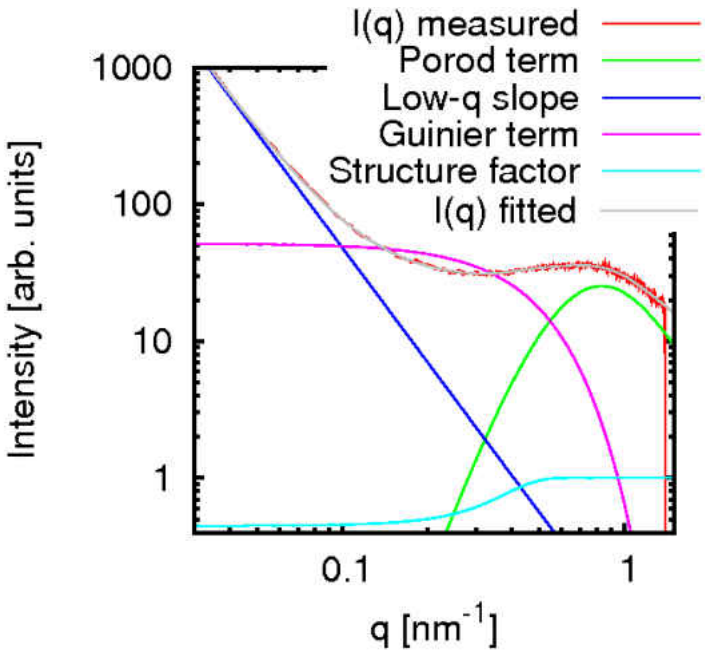

Figure 6.19: Illustration on how the unified model (Eq. (6.34)) was fitted to the GISAXS data taken at 550 °C. Here the subset for the second temperature regime was used. [61]

discrepancy at 550 °C is explained by the fact that the first fitting regime did not fit especially well (as was shown in figure 6.18). Then the Porod slope continue to change as the sample is heated; for example, $P_1 = 3.38$ at 600 °C and $P_1 = 3.89$ at 800 °C, which is the maximum value of P_1. Thereafter, the value of P_1 decrease, and at 900 °C, $P_1 = 3.62$. This means that in the interval 600 °C $\leq T \leq$ 900 °C, $3 \leq P_1 \leq 4$, which corresponds to the particles being surface fractals. The value of P_1 continues to decrease with further heating, to $P_1 = 2.35$ (at 1000 °C), indicating a rougher surface structure once more (mass fractals).

The increase in the value for $\bar{a}$ means that the scattering particles are positioned further apart for higher temperatures, and since the particle size is also increasing, this suggests that the particles are undergoing Ostwald ripening.

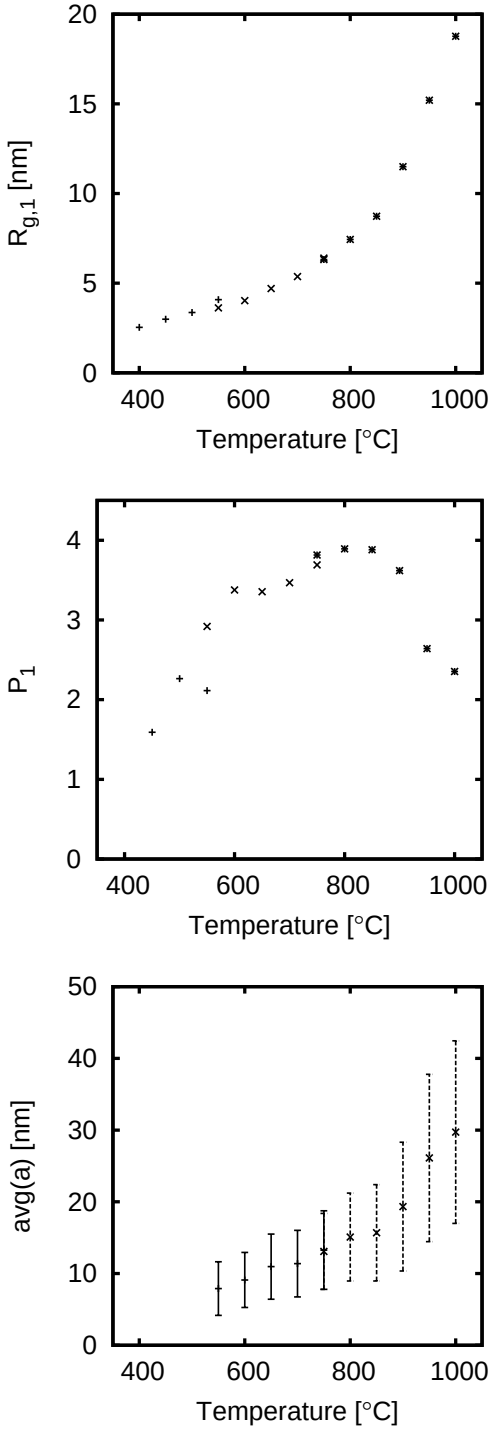

Figure 6.20: The unified model applied to the measurements at different temperatures for the Zr-Y-B coating. The different symbols represent the different fitting regimes. (Top panel) Radius of gyration ($R_{g,1}$). (Middle panel) Porod slope ($-P_1$). (Bottom panel) Average separation distance $\bar{a}$ between scattering objects (see Eq. (2.36)). Note that the bars are the value obtained for w (see Eq. (2.36)). [61]

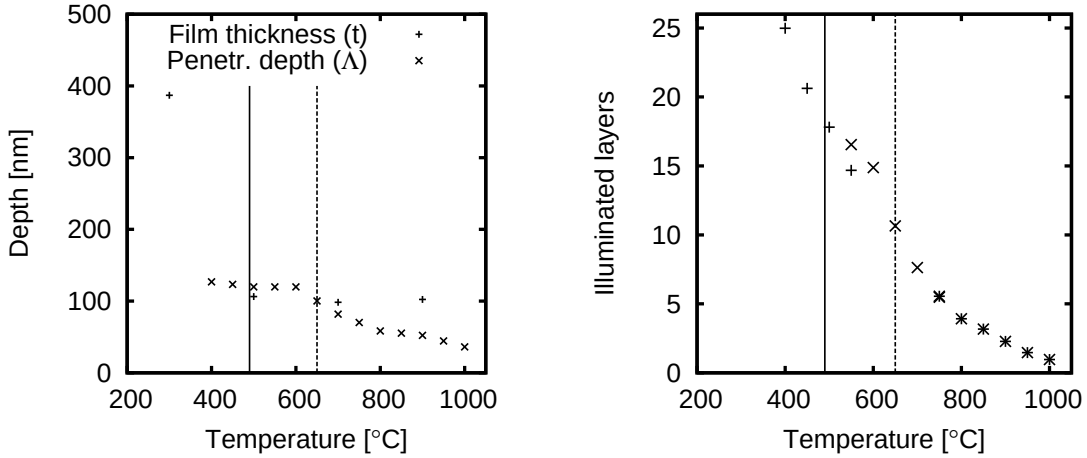

Figure 6.21: Left: The theoretically calculated penetration depth Λ for coating B, and the film thickness t of a similarly prepared film measured by *ex situ* ellipsometry. For the region 490 °C $\leq T \leq$ 650 °C (vertical lines in both panels), the penetration depth is larger than the film thickness. Right: Estimated number of illuminated layers of particles for the different temperatures: $\Lambda/(2R_g)$. The different symbols refer to the different fitting regimes. [61]

The penetration depth, Λ, and also the film thickness decrease as the film is heated. In order to show how large the illuminated fraction of the film is, the film thickness, measured from ellipsometry, and Λ, estimated from Eq. (2.73), are plotted in figure 6.21(a). Figure 6.21(b) is an estimate of the number of layers of particles within the penetration depth: $\Lambda/(2R_g)$.

In figure 4.7, the appearance of small "wings" in the panel corresponding to the 550 °C measurement, is characteristic of a 2D component in the scattering pattern. However, figure 6.21 illustrates that the measured signal extends from a sufficient depth such that it should appear to be 3 dimensional. Therefore, we conclude that a layer of this 3D film has predominantly 2D character.

As the sample is heated, the pattern changes, and for the 750 °C measurement,

a typical powderlike scattering pattern is obtained, which is an indication of a three-dimensional distribution of scattering centres. For this temperature, Λ is about 2/3 of the film thickness ($\Lambda/(2R_g) = 6$). However, we cannot rule out that the pattern may also be a wing-type pattern where the particles have grown so large that the wings have shifted so far towards low-q that the full wings cannot be observed any longer, just the outer end of the wings.

As the sample is heated further, the scattering intensity showed a broadening in the y- and z direction. This is especially distinct for the 950 °C measurement, and this is most likely due to a wing-pattern where the wings are disappearing at the low-q end. As already mentioned, this is typical for a two-dimensional distribution, which is to be expected considering that only 1 to 1.5 particle layers are within Λ at these high temperatures. Combining this finding with the result of the Porod analysis for the highest temperatures, where the particles were found to have rougher surfaces, it is a distinct possibility that only the particles in the topmost layer become rougher, whilst the particles further below in the film surface remain smooth.

These considerations lead to a model of the calcination mechanism as follows (see figure 6.22): At 450 °C, in the nucleation regime, the scattering particles are small and having rough surfaces, and they are randomly positioned in the sample. As the sample is heated, the particles are undergoing Ostwald ripening, and the particle surfaces become smoother, until the highest temperatures where the particle surface, at least in the topmost layer, again becomes rougher. The

reason for this may be related to growth instabilities:

If the sample is heated slowly, the particle surfaces is expected to remain smooth as the particles grow. This is because of the minimisation of energy principle - the molecules in the bulk is having lower energy than the molecules on the surface of the particles, as mentioned in the paragraph about Ostwald ripening (in Section 6.2.2). However, if the sample is heated too fast for the particles to equilibriate; more and more molecules are "thrown in on top", the surface of these particles will become rough. Consequently, the roughening observed for the particles at the highest temperatures, may be due to such a growth instability.

6.5.4 GISAXS: Zirconia on silicon, *in situ* heating

Some of the resulting plots from this sample were shown in figure 5.6, and the unified model in form of Eq. (6.34) were fitted to the data. Again, different subsets of the unified model needed to be used, and these are listed in table 6.9. The reason for slightly different values in the end of the fitted q-range is because different cuts are taken at different detector heights; the maximum q-value measured depends on the detector height for which the cut was taken, and this is what is plotted. However, at 600 °C, it was not possible to fit to the last q-values, and the reason for this will be explained in Section 6.5.4.2.

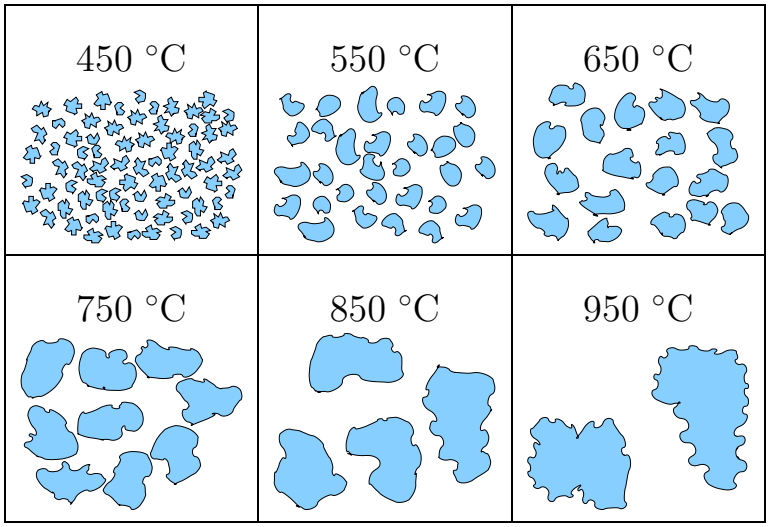

Figure 6.22: Illustration of our interpretation of the available data from the GISAXS experiment (ZrO_2-Y_2O_3 coatings), seen from above. This illustration is considerably simplified; at the lowest temperatures the particles are probably more like polymers, and for all temperatures the particle sizes are more likely to follow a log-normal distribution. The suggested model for particle development during heating program is as follows: First, in the nucleation regime, the particles are small, irregular and randomly positioned. As the sample is heated, particles form larger, and fewer, particles where the average separation distance increases (Ostwald ripening). Since SAXS measures differences in electron density, the medium between the particles could either be material of a different electron density (for example hydrocarbons - which are likely at the lowest temperatures), or simply air (which is most likely at the highest temperatures). [61]

Subset	Temperature [°C]	Levels	$S(q)$	Background (C)	Beamstop	Fit range (q) [nm^{-1}]
I	400	1		Fixed	Wide	0.314-1.22
	450	1		Fixed	Wide	0.26-1.22
	500	1		Fixed	Wide	0.26-1.35
	550	1		Fixed	Wide	0.26-1.35
II	600	1	✓	Fixed	Wide	0.26-1
	650	1	✓	Fixed	Wide	0.26-1.3
	700	1	✓	Fixed	Wide	0.26-1.32
III	700	1		Fixed	Wide	0.26-1.32
	750	1		Fixed	Wide	0.26-1.35
	800	1		Floating	Medium	0.26-1.22
IV	850	1	✓	Floating	Narrow	0.05-1.22
	900	1	✓	Floating	Narrow	0.05-1.22
	950	1	✓	Floating	Narrow	0.05-1.35
	1000	1	✓	Floating	Narrow	0.05-1.35

Table 6.9: Table showing how the unified model (Eq. (6.34)) was used for the data measured at different temperatures.

6.5.4.1 Subset (I):

For the measurement at 500 °C, two different methods was found that could be used for fitting the data. These two methods were found to give different results, and in the following section the reason for the chosen method will be discussed. The method that was not used is discussed first.

Method A: The Guinier plot of the measurements taken at 500 °C is shown in figure 6.23 (left hand panel). The fitted line has a slope of 0.419, and the corresponding radius of gyration is then $R_g^{Guinier} = 1.70$ nm. The same measurement, but plotted using logarithmic values on the axes is shown in figure 6.23 (right hand panel), together with the Guinier term where $R_g^{Guinier} = 1.70$ nm. The fact that the measured intensity at $q < q_{shoulder}$ is lower than the predicted intensity from the Guinier term, suggests that a structure factor needs to be used. However, in

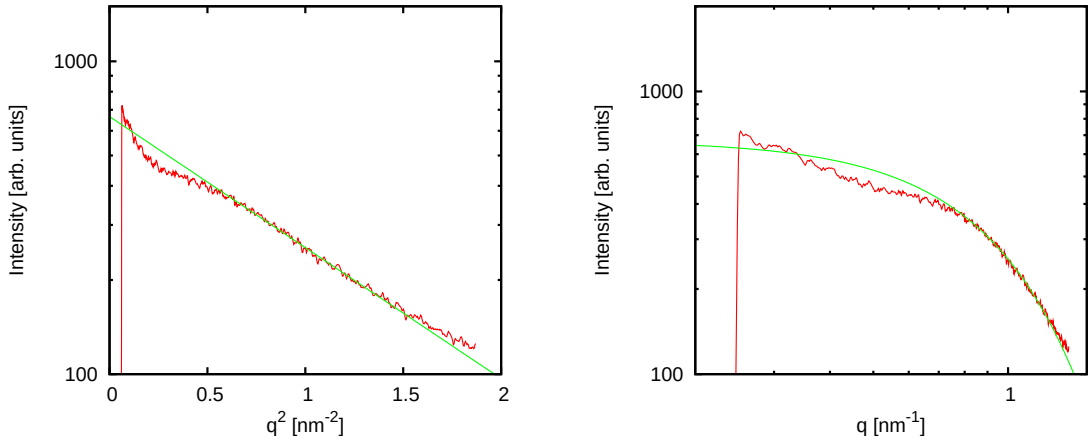

Figure 6.23: 1D-cuts at the Yoneda angle for the GISAXS measurements on the zirconia coated silicon wafer, when the temperature was set to 500 °C. These plots show the results of the Guinier analysis. Left: The Guinier plot ($\log(I)$ *vs.* q^2) shows a long straight slope. Right: the $\log(I)$ *vs.* $\log(q)$ plot of the same data, and the Guinier term using the result for R_q that was found from the Guinier analysis.

order to use the unified model, the Porod term is introduced. The Porod exponent is first fitted to the short linear region at the highest q-values, and then this result for P is used in the rest of the plots without letting it float in these fits. The reason for this is that the straight line at high-q is not long enough to be able to let P float at the same time as all the other parameters.

The constant background contribution was found by first fitting a constant value to the region at very low q-values (behind the beamstop), and then fix the parameter to the value obtained. The plot after the constant C and the structure factor (Eq. (2.36)) was introduced is shown in figure 6.24 (left hand panel). The extra intensity at low q-values ($h(q) = B_0 q^{-P_0}$) is probably due to very large particles. This contribution was attempted to be included in the model, but then the fitting procedure did not converge on any realistic solution. Instead $h(q)$ was

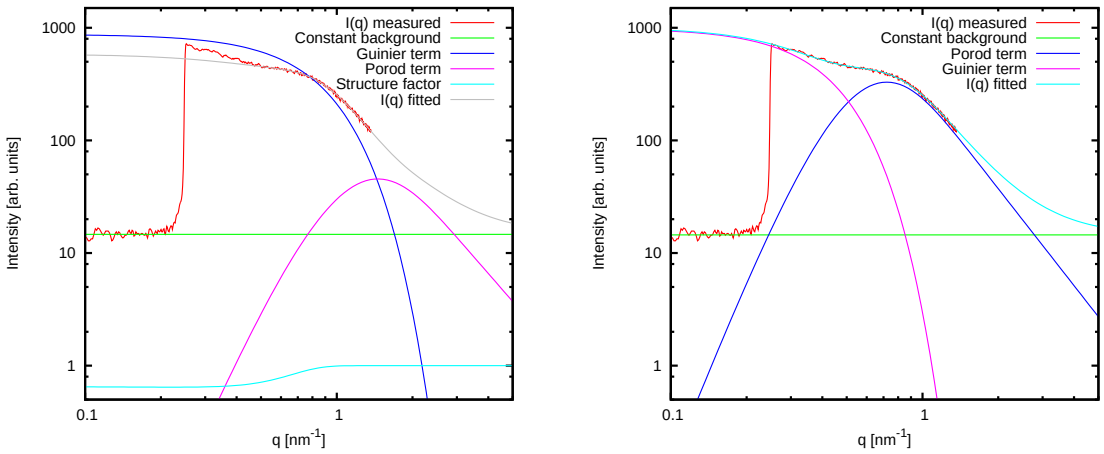

Figure 6.24: Comparison of two different methods of applying the unified model to the data from the measurement on the zirconia coated silicon wafer taken at 500 °C; both models seem to fit well the data measured in the range around the shoulder, and it is therefore difficult to determine which model is the most suitable. Left: Method (A) (not used). Right: Method (B), used as "Subset (I)". Notice the difference in amplitude for the Porod term in the two methods.

set to zero, and the unified model was used in the form

$$I(q) = S(q) \times G \exp(-q^2 R_g^2/3) + B\{[\mathrm{erf}(qR_g/\sqrt{6})]^3/q\}^P + C. \qquad (6.35)$$

This model was then fitted from larger q ($= 0.5$ nm^{-1}) than the smallest measured q-value. The most interesting results are obtained from the parameters describing the particle size, the average separation distance between the particles and the surface structure of the particles, namely R_g, $\bar{a}$ and P, respectively. For example, the results from this fit are: $R_g = (2.07 \pm 0.05)$ nm, $\bar{a} = (4.01 \pm 0.03)$ nm and $P = 2.57 \pm 0.03$.

Method B: Rather than fitting the Guinier term first, and then add everything

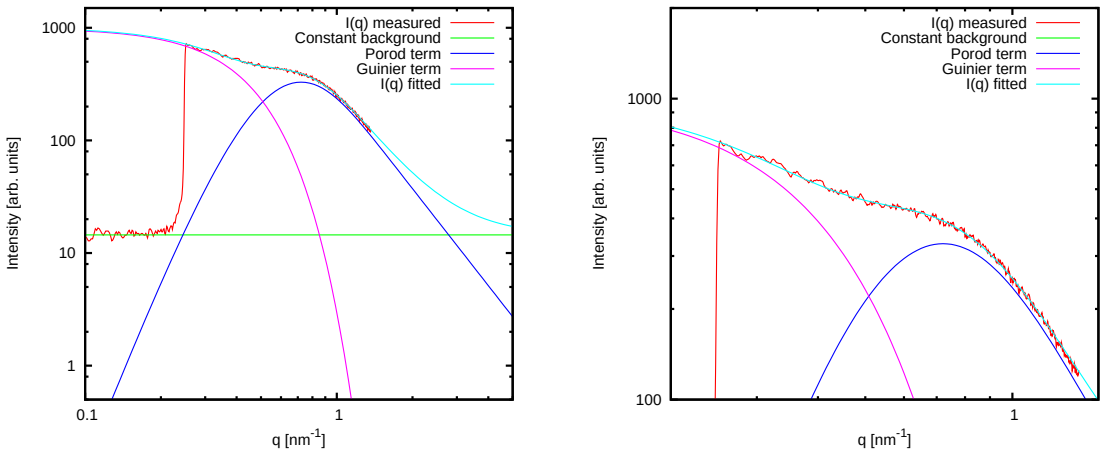

Figure 6.25: In order show how method B fits the data for different ranges on the axes, the same data that was shown in figure 6.24 is now plotted using different axes ranges. Left: same as figure 6.24 (right panel). Right: zoom-in of the ranges such that more details can be seen in the fit and in the data.

else as it fits, the Porod term was fitted first. In this case the structure factor was not needed, and the unified model was used in the form

$$I(q) = G\exp(-q^2R_g^2/3) + B\{[\mathrm{erf}(qR_g/\sqrt{6})]^3/q\}^P + C. \tag{6.36}$$

C was determined from the measured $I(q)$-plot at low q-values, since the beam-stop shadowed the scattered intensity here. All the parameters (except C) were set to float for the entire range, and the result is shown in figure 6.24 (right hand panel).

In order to show the difference between method A and B, figure 6.24 shows each method in a separate panel. Figure 6.25 also shows the plot for method B in more detail.

In method B, fewer fitting parameters were needed, and the entire q-range could be fitted with all the parameters floating. By fitting this model to the other measurements in the same temperature interval, it was noted that only method B was giving converging fits. In the end method B was used for Subset (I), however, we cannot exclude that method A may be more suitable.

The most interesting results are obtained from the parameters describing the size- and the surface structure of the particles, and using this method these values were found to be: $R_g = (4.17 \pm 0.01)$ nm and $P = 2.86 \pm 0.02$, respectively. It is noticed that the radius of gyration found using method B is approximately twice the radius of gyration found by using method A, and approximately the same as the average separation distance found using method A.

6.5.4.2 Subset (II)

This subset was used for the range 600 °C $\leq T \leq$ 700 °C, and an example is shown in figure 6.26 for the measurements at 600 (top panels) and 650 °C (bottom panels). In the measurement at 600 °C, we observe that the slope of the measured intensity suddenly becomes steeper at $q \approx 1$ nm^{-1} (see the top right panel). The reason for this is not known and this behaviour has not been observed in any of the other measurements. Models were attempted to be fitted to the intensity for the entire q-range, including $q > 1$ nm^{-1}, but this was without success. This is why the model is only fitted for $q < 1$ nm^{-1} in this case.

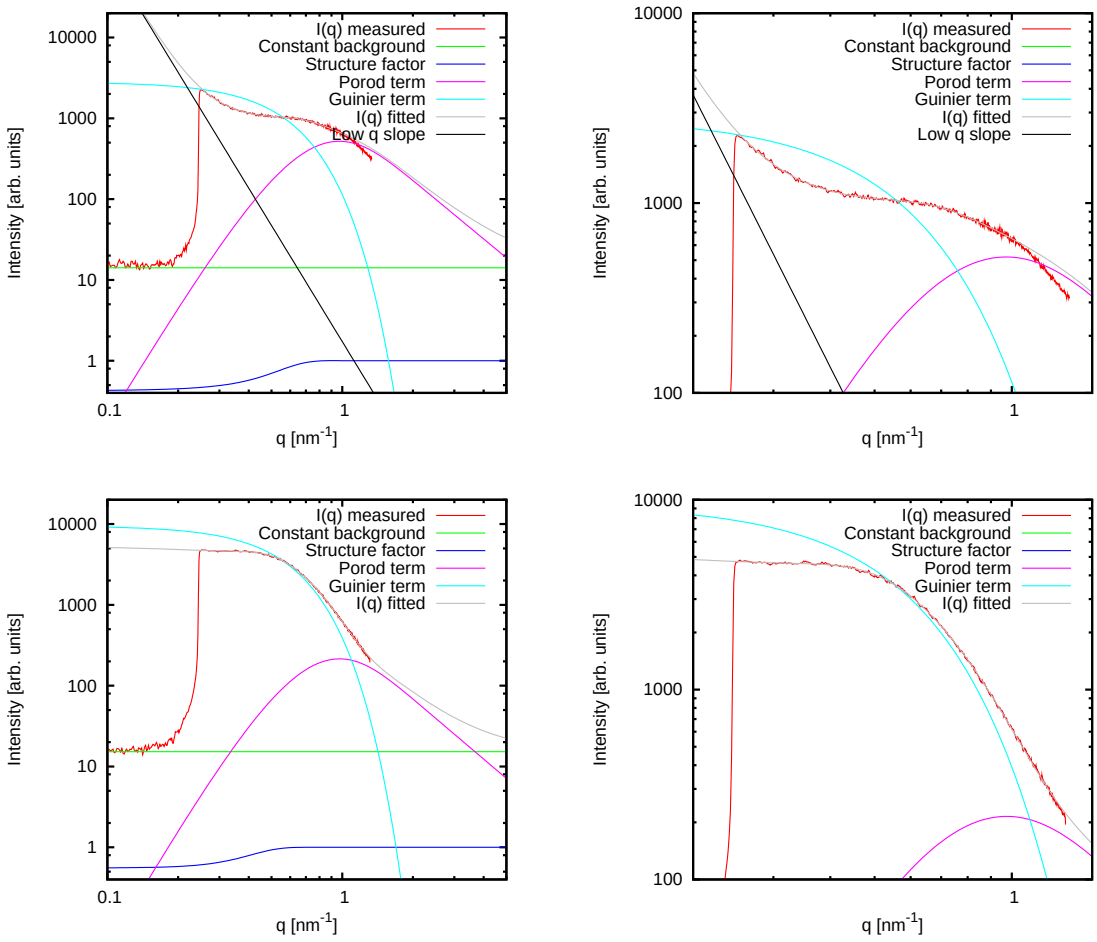

Figure 6.26: The application of Subset (II) to data. Top row: 600 °C. Bottom row: 650 °C. The left hand panels show the extended ranges of the axes, whilst the right hand panels show the zoom-in of the measured pattern. For the measurements at 600 °C, it was noticed that the slope at the high-q end becomes steeper at $q > 1$ nm^{-1}.

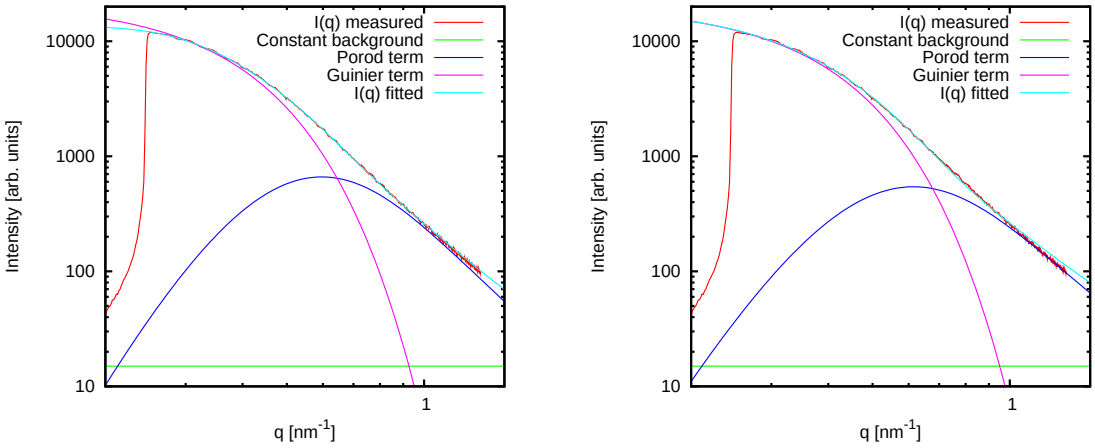

Figure 6.27: The measurement taken at 700 °C. Left: Subset (II). Right: Subset (III). Closer investigations show that Subset (II) fits slightly better to the data at the high-q end.

6.5.4.3 Subset (III)

This subset was used for the range 700 °C $\leq T \leq$ 800 °C, and an example is given in figure 6.27 (right hand panel). The measurement at 700 °C, could be approached using the method used in either Subset (II) or Subset (III), and both results are plotted in figure 6.27. Closer investigation reveals that Subset (II) (left hand panel) gives a slightly better fit at the high-q end than Subset (III) (right hand panel). A structure factor was used in Subset (II), but the intensity of this is too low to be included on the figure.

6.5.4.4 Subset (IV)

This subset was used for the temperatures above 800 °C, and an example is shown in figure 6.28.

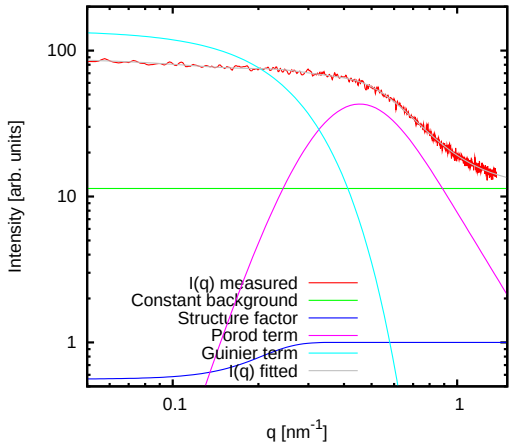

Figure 6.28: The method used in Subset (IV) applied to the data measured at 950 °C.

The results for the radius of gyration, the Porod slope and the average separation distance are plotted in figure 6.29. As can be observed from the results for the radius of gyration, the behaviour can be divided into three regimes, and it is most likely different types of particles that are observed in each of the regimes;

1) 400 °C $\leq T \leq$ 550 °C: Here the particles are small and remain nearly constant in size. The Porod slope is between -2 and -3, which corresponds to pretty rough surface structure, possibly corresponding to mass fractals.

2) 600 °C $\leq T \leq$ 750 °C: The particle size increases significantly within this temperature range. The average separation distance increase significantly as well. The Porod slope could not be determined for the 600 °C measurement, and for higher temperature it changes from around -2 to around -4 which means that the surface structure of this type of particle becomes smoother.

3) 800 °C $\leq T \leq$ 1000 °C: At 800 °C, the value for the radius of gyration is

noticeably smaller than the value obtained at 750 °C. Probably a different kind of particle is measured in this temperature regime. This kind of particle keeps growing slowly as the temperature is increased. Here, as well as in the second regime, the average separation distance increase significantly. The Porod slope varies between -3 and -4, possibly corresponding to surface fractals. At the highest temperature the surface structure of the particles were found to be rougher; at 1000 °C, $P \leq 3$ which corresponds to mass fractals.

From the values obtained from G, B and R_g in the fits, u_{norm} was calculated, and the result is listed in table 6.10. For the first temperature regime, large values of u_{norm} was found, which corresponds a to very large surface area of the particle compared to its volume. Comparing this result to the values for the Porod slope for this regime, $P = [2, 3]$, it is suspected that these particles are mass fractals.

For the second temperature regime, especially for the measurements taken at 650 and 700 °C, the value found for u_{norm} is rather small. It is therefore likely that the scattering particles are having relatively compact shapes at these temperatures.

Within the third regime, a steady increase in the value for u_{norm} is observed, and therefore it is likely that the particles are becoming fractals at these temperatures. By comparing to the values for the Porod slopes, the particles are probably surface fractals, but transforms towards mass fractals when the temperature get high enough, *i.e.* at ~ 1000 °C.

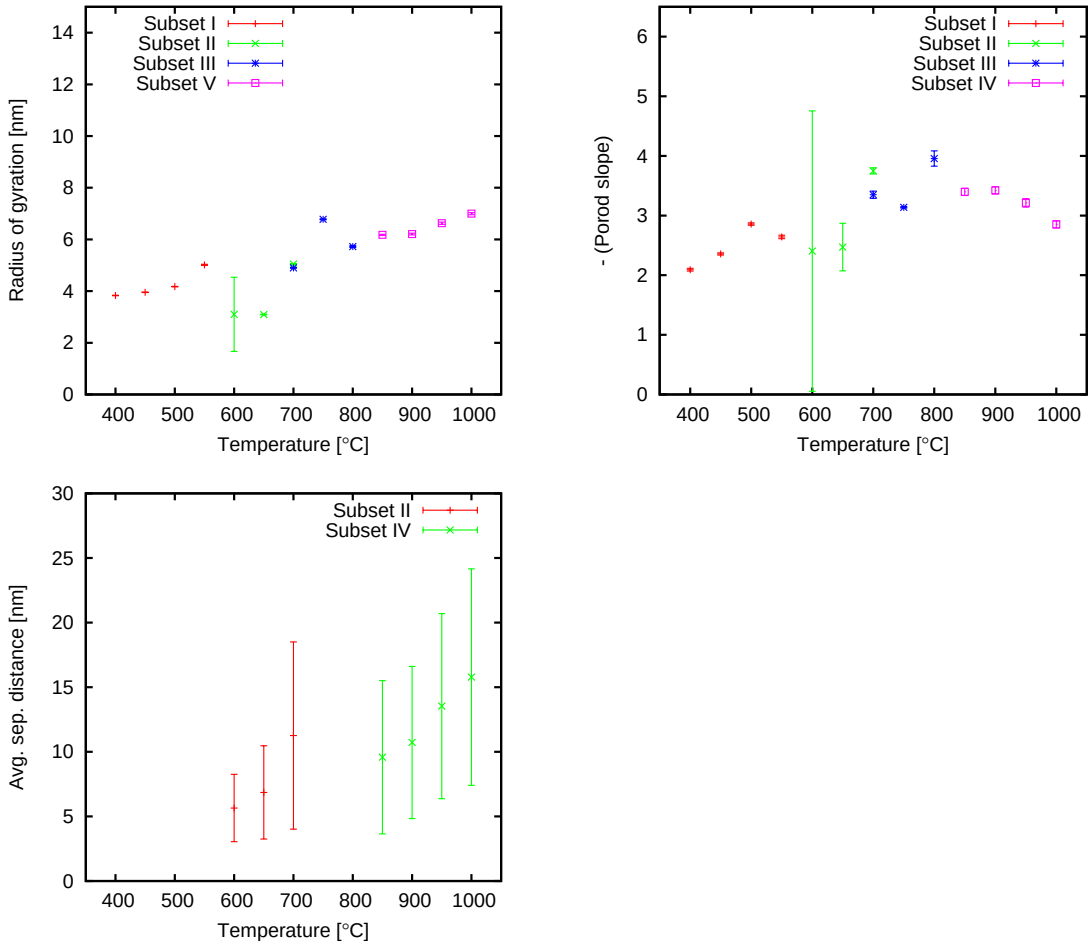

Figure 6.29: The fit parameters obtained after applying the unified model to the 1D-plots from the data measured for the zirconia coated silicon wafer. Top left: radius of gyration. Top right: Porod slope ($-P$). Bottom left: Average separation distance, where the bars are the value of w obtained from the fits.

Regime	Temperature [°C]	$u_{norm} = (R_g^4 B)/(1.62G)$
1	400	86.3
	450	86.8
	500	51.1
	550	65.8
2	600	18.3
	650	1.46
	700 (Subset II)	4.56
	700 (Subset III)	4.35
	750	13.1
3	800	26.1
	850	43.7
	900	45.2
	950	67.6
	1000	100

Table 6.10: The values obtained for u_{norm} for the zirconia coating on a silicon wafer. The different regimes are the regimes found from the investigation of R_g.

Studies of zirconia has also been performed by other research groups. For example, Lenormand *et al.*, found that, by using XRR, XRD and GISAXS, that during the thermal treatment, the removal of the organic residues is concomitant to the crystallisation of the amorphous film which is transformed in a polycrystalline layer with a random orientation of tetragonal zirconia nanocrystals [70].

Recall the discussion that it is difficult to separate cubic and tetragonal phase (section 6.3). Consider figure 2 in the paper by Lenormand *et al.* [70]; this figure is showing the XRD results, and the measurement taken for when the sample was heated to 600 °C, which according to Lenormand *et al.* is tetragonal. In this pattern, Bragg peaks with a certain width, positioned at around $2\theta = 30$, 35, 50 and 60 degrees are observed. This means that, from Lenormand's figure alone, it is difficult to know whether the sample they measured is tetragonal or cubic

zirconia.

Lenormand *et al.* also found that the densification of the layer, up to 86 % of the theoretical tetragonal zirconia mass density at 1000 °C, occurs by a one-dimensional shrinkage, *i.e.*, by a strong reduction of their thickness. Due to their narrow size distribution, the tetragonal zirconia nanocrystals are self-organised in a dense close-packed microstructure which is conserved and evolves by a normal grain growth mechanism up to 1000 °C [70].

This grain growth that Lenormand *et al.* mentioned, is not very clear from these GISAXS measurements, see figure 6.29, top left panel. However, the SAXS measurements (figure 6.10) did show a significant increase in particle size as the temperature was increased. Possible reasons for this discrepancy will be discussed in Section 7.1.1.

6.6 Significance of different yttria concentrations

In order to study the influence of yttria doping, samples containing different concentrations of yttria were investigated, and some of the horizontal cuts for the measurements performed at 850 °C are shown in figure 5.5. The radii of gyration found using the unified model for the measurements performed at the temperatures 800 °C $\leq T \leq$ 1000 °C are shown in figure 6.30 (left panel), and the values obtained for the Porod slope are shown in figure 6.30 (right panel).

The radii of gyration found for the Zr-Y-A and Zr-Y-B coatings are practically the same (except at 1000 °C) whilst for the zirconia coated sample and sample D

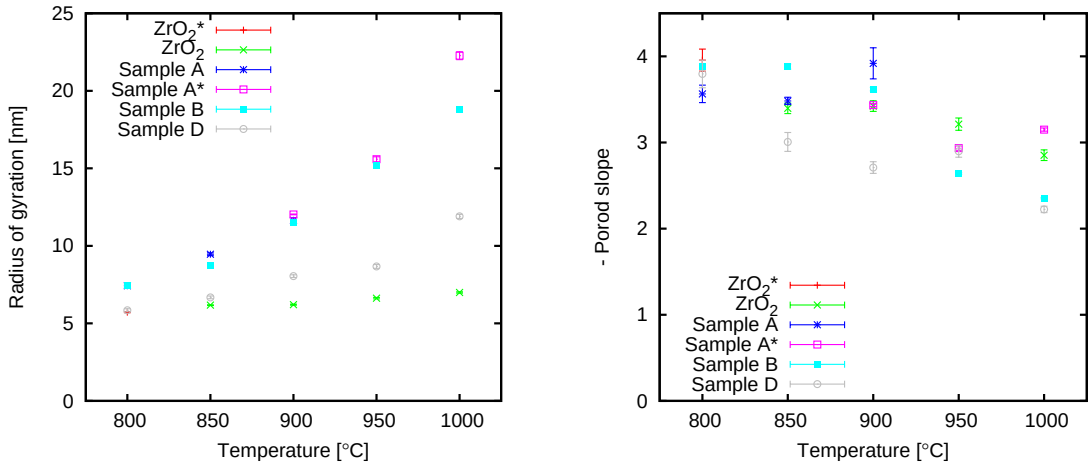

Figure 6.30: Radius of gyration (left) and Porod slope (right) found for the different samples in the temperature range 800 °C $\leq T \leq$ 1000 °C using the unified model (Eq. (6.34)). (*) $S(q) = 1$. Otherwise, $S(q)$ from Eq. (2.36) is used. The error bars are the fitting uncertainties.

it is noticeably smaller. For all of the samples containing yttria, the radius of gyration increases with temperature, and thus the size of the scattering objects increases for these three samples. The radius of gyration obtained for the zirconia coated sample was found to stay approximately constant, or slightly increasing, for this temperature range.

The fitted Porod slope is between -3.5 and -4 (see figure 6.30 (right panel)) for sample A and B between 800 and 900 °C, *i.e.*, the surface structure of the scattering objects is smooth or nearly smooth for this temperature range. For sample A, the Porod slope changes to be around -3 (at 950 to 1000 °C), whilst for sample B it changes even more, to around -2.3 (at 1000 °C), indicating a rougher surface structure. For the zirconia coated sample, the Porod slope remains between -3 and -4 for the entire temperature range, except at 1000 °C where it is -2.85. For sample D the Porod slope changes from -3.8 (800 °C) to -2.6 (900 °C),

and therefore the surface structure of the particles changes from being smooth to becoming rougher at lower temperature than for the other samples. There seems to be a correlation between yttria concentration, and at which temperature the surface structure of the particles become rougher, and this correlation will be explored further in towards the end of this section.

The results obtained for R_g were compared with XRD measurements on *ex situ* samples which were annealed at 900 °C (see figure 5.11). The Bragg peaks were found to be wider for the samples containing more yttria, and the resulting size parameter t from Scherrer analysis of the diffractograms is given in table 6.3. In order to compare the results from the Scherrer analysis with the results obtained from GISAXS, the values are plotted as a function of yttria content in figure 6.31.

Figure 6.31 shows that the measured values for t and R_g differ significantly for low yttria concentrations and for pure zirconia, whilst for high yttria concentrations the values are more similar. Recall that t is the thickness of the "platelet" (see Section 6.3.2), and that t thus gives information about the size in the vertical direction. Since R_g was obtained from the horizontal cuts of the GISAXS patterns, the measured value of R_g here only gives information about the particle size in the direction along the sample surface. If the particles are spherical, t and R_g should show relatively similar values. It is therefore likely that for the low yttria content or pure zirconia, the scattering particles are having a more cylindrical shape. In the pure zirconia coating, the diameter of the cylinders remains approximately constant within this temperature range (see figure 6.30), whilst

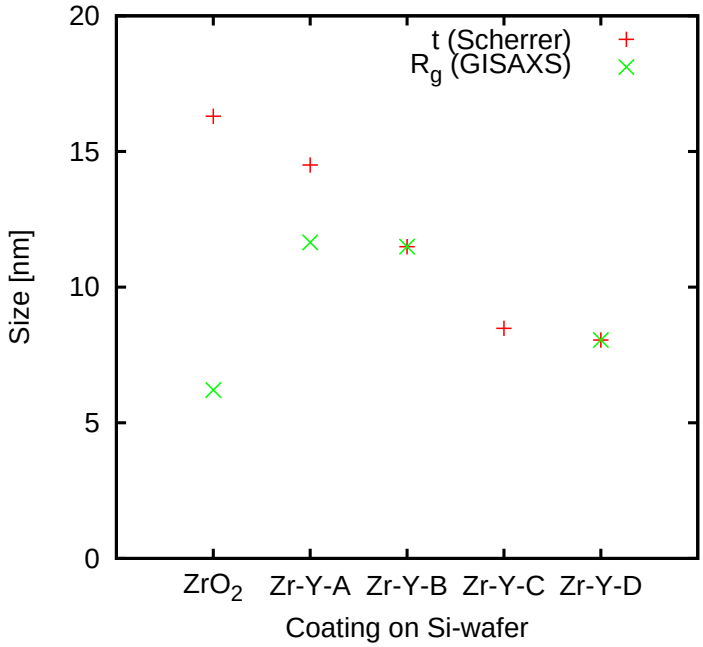

Figure 6.31: Values obtained for t from the Scherrer analysis of the X-ray diffractograms taken for the samples which were annealed at 900 °C, compared to the values obtained for R_g using the horizontal cuts of the GISAXS pattern which was measured when the sample was heated to 900 °C.

the height of the cylinders increase with increased temperatures (see table 6.3). For higher yttria contents, however, the relative values of t and R_g were showing similar behaviour for increasing yttria content, and the shape of the scattering particles would therefore be more spherical.

On the other hand, whilst R_g of the zirconia sample remained approximately constant as the sample was heated from 800 to 1000 °C, R_g of the Zr-Y-A coating increased significantly. The hypothesis for this particle system at this temperature range is therefore that the pure zirconia coating consists of ZrO_2 crystalline pillars that increase in height but not in diameter as the sample is heated and that the yttria rich coatings consist of spherical crystallites of YSZ that increase in size with increased temperature. The Zr-Y-A coating is likely to consist of a mixture

of the ZrO_2 pillars and spherical YSZ particles, where the pillar height and the size of the spherical particles increase with increased temperature.

For the yttria-containing samples, the size of the crystallites decreases with increased yttria content (see figure 6.31). Recall from the discussion of the Porod slopes, that the onset of surface roughening of the particles happens at lower temperature as the yttria concentration increases. The reason for these observations may be that there is more chemical disorder in the crystalline lattice within the particles of the samples with the higher yttria concentration, which is due to the onset of phase separation into yttria-richer and yttria-poorer regions.

In the XRD discussion earlier in this chapter we found that the lattice parameter increased with increased yttria concentration, see Section 6.3.3. Our results were found to agree with the results of Hayashi *et al.* (see Section 6.2.1). This increase of the lattice parameter was explained by the increase of Y-O bond lengths; since the Y-O distance (0.23 nm) is longer than the Zr-O distance (0.21 nm) [5]. These longer bond-lengths will result in a more disordered crystalline lattices within the samples containing more yttria.

6.7 Different incident angles

Eqs. (2.73) and (2.41) show that the penetration depth of the X-rays depends on the angle of incidence. In order to investigate the behaviour of the GISAXS pattern as the incident angle is varied, GISAXS patterns were measured using several different incident angles.

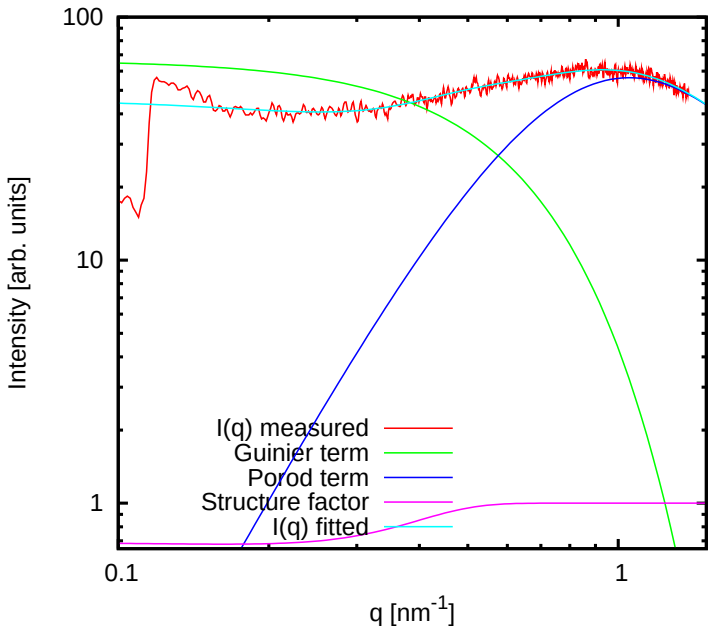

Figure 6.32: The unified model applied to the data measured using GISAXS on the zirconia coated silicon wafer heated to 500 °C, *ex situ*.

The sample used here was a Si(100)-wafer which was dip-coated into the zirconia-sol 4 times, and dried inbetween each layer. It was then annealed at 500 °C *ex situ*, brought to the beamline and the measurements were performed under ambient temperatures.

Some of the resulting GISAXS patterns were shown in figure 5.8, and no obvious differences can be observed by eye from these patterns. 1D cuts were taken at the Yoneda feature (figure 5.9), and the only obvious difference in these plots are the overall intensity, and some extra intensity at low q-values for the shallowest angle measurement, which comes from the diffuse part of the reflected beam which is not relevant for the SAXS pattern. The difference in overall intensity is explained by Fresnel reflectivity theory; recall figure 2.5.

Note the similarities in the plots of these 1D-SAXS patterns with the SAXS

patterns measured during the *in situ* dipping experiment, figure 5.3 (upper left panel). For these SAXS data, the unified model could not be used. On the other hand, for the GISAXS measurements taken at 500 °C, the unified model was successfully applied to the 1D-cuts as shown in figure 6.32, and the results are plotted in figure 6.33. The reason for why the unified model could be used for the GISAXS measurements and not for the SAXS measurements, is probably mostly because of the high-q slope: The GISAXS measurements have a well enough defined Porod slope for the unified model to be applicable, whilst the SAXS data does not; recall that the peak in the SAXS data behaves more like to a broad Bragg peak.

For the different angles the measured sizes remained approximately constant (R_g and $\bar{a}$). On the other hand, the Porod slope appears to change for larger incident angles such that the particles within the illuminated scattering volume become smoother. This agrees with the values measured for u_{norm}; these values seem to decrease for larger incident angle. Since the depth penetrated by the X-rays is dependent on the angle of incidence, this may mean that particles further down in the coating are smoother than the particles at or near the surface.

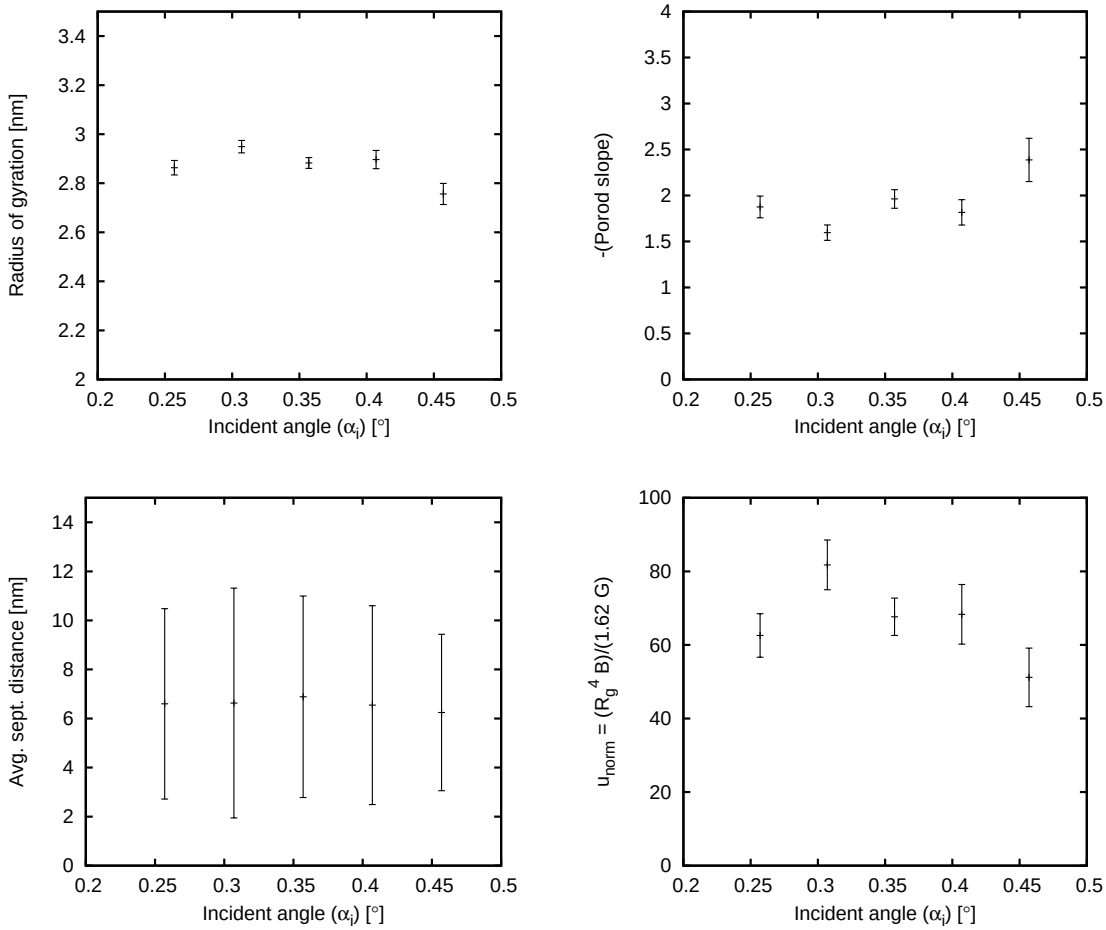

Figure 6.33: Fit parameters obtained from the GISAXS patterns of the zirconia coated silicon wafer; 4 dips were performed and the sample was heated to 500 °C *ex situ*.

Chapter 7

Summary

X-ray techniques have been used to study zirconia- and yttria doped zirconia coatings. The experimental techniques used are laboratory-based X-ray diffraction (XRD) and synchrotron radiation based small-angle X-ray scattering techniques in both transmission mode; small-angle X-ray scattering (SAXS), and reflection mode; grazing-incidence small-angle X-ray scattering (GISAXS).

By using XRD measurements information has been gained about the crystal structure of the coatings, and using (GI)SAXS information has been gained about size- and surface structure of the scattering particles (R_g and P, respectively), and also about the average separation distance between the particles ($\bar{a}$). The kind of materials studied in this work only allows for the use of restricted models, and spherically symmetric particles have been assumed (except for the pure zirconia coating, as discussed in Section 6.6). This is because when a sample is produced by sol-gel processing, the shape of the resulting nanoparticles is not well-defined,

and spherical symmetric particles are used as an approximation of the particle shape.

For extracting the relevant parameters, such as R_g, P and $\bar{a}$, Beaucage's unified model has been applied. This is because the traditional Guinier and Porod plot methods are only valid for restricted parts of the q-range; the Guinier method is generally only valid for $qR_g \lesssim 1.3$, and the Porod method is only valid for the high-q slope. These limitations are corrected for in the unified model. Also, the traditional methods only account for one level of structural features, whilst the unified model can be extended to account for multiple levels of structural features, and it is therefore valid for the entire q-range. In these (GI)SAXS experiments, the unified model has been applied successfully to most of, or the entire measured q-range.

Our XRD-data for the coatings did not reveal any structure altering phase transitions, not even for pure zirconia; which stayed in the mainly cubic structure for all the temperatures measured at: 500, 700 and 900 °C (see figures 5.10 and 5.12), instead of the monoclinic structure typical for bulk ZrO_2 previously found for these temperatures. This can, however, be explained: Previously, phase transitions have been measured for bulk ZrO_2 crystals. Since the experimental results are often controlled by the small quantities of unintentional impurities, the intrinsic behaviour of ZrO_2 is difficult to observe. We measured the diffraction patterns of sol-gel derived ZrO_2 coatings; it is therefore not surprising that we did not observe any phase transitions. The crystal structure was found to be mainly cubic, but

maybe containing a small amount of tetragonal domains, for all of the different coatings measured at 500, 700 and 900 °C. However, within our group, we have also measured the diffraction pattern from sol-gel derived ZrO_2 *powder*, when it was incrementally heated in 50 °C steps *ex situ*, and in this experiment we found a phase transition from mainly cubic to monoclinic around 500 °C [14]. Possible reasons for this discrepancy may be that perhaps it makes a difference whether the zirconia is in the form of a coating or a powder. Also the recipe used for producing the zirconia as a coating (see section 3.2.2) and as a powder (see [14]) was slightly different (less isopropanol and less acetic acid was used in the recipe for the powder experiment). Another difference is that in the powder experiment, the same sample was incrementally heated, whilst in the experiment where the zirconia was in the form of a coating, three different samples were heated to three different temperatures, and these samples were produced eight days before the actual XRD measurements were performed.

Even though XRD results did not show any obvious phase changes, the *in situ* heating scattering measurements did reveal that the scattering patterns from the zirconia coating changed significantly for each temperature in the range $700\ °C \leq T \leq 900\ °C$ (SAXS) and $550\ °C \leq T \leq 850\ °C$ (GISAXS). On the other hand, the scattering patterns measured from the yttria-doped zirconia coatings during *in situ* heating, showed a slow and gradual transition between the lowest and the highest temperature measurement.

7.1 *In situ* heating

Generally, for the *in situ* heating experiments, it was found that the size of the particles and the separation distance between particles both increase with increased temperature. This is interpreted as Ostwald ripening of the particle system. Ostwald ripening is the process where many small particles goes together to form fewer and larger particles; this means that the observed size as well as average separation distance will increase, and this is indeed what is observed.

7.1.1 Zirconia

The zirconia coating was measured using both SAXS and GISAXS; each method giving slightly different results:

The SAXS results reveal first one type of particle that remains at approximately constant size,$\sim$ 25 nm, as the sample is heated, until it disappears at $T > 800$ °C. Another particle type appears at 700 °C; this particle type keeps increasing in size as the temperature is increased - even after stabilising the temperature on 950 °C, this particle size keeps increasing for about 10 more measurements when the temperature is kept at 950 °C (see figure 6.10). The Porod slope remains nearly constant; $P \lesssim 4$ for the entire experiment, except for a region between 750 °C $\leq T \leq$ 850°C, where it is difficult to determine an accurate value of the Porod slope.

The GISAXS results, however, show first one small particle type that do not change significantly in size, between 4 and 5 nm, for the range 400 °C $\leq T \leq$ 550 °C,

and the results from the Porod slope shows that these particles are likely to be mass fractals. At 600 °C, this particle type disappears, and another smaller particle type appears. The latter particle keeps increasing significantly in size when the temperature is increased, until at 750 °C where this particle type disappears. Within this range the Porod slope changes significantly, from -2 to -4 (approximately), which indicates that the surface of the particles change from being very rough (mass fractals) to be smooth. At 800 °C another particle type appears, which increase slowly in size for the rest of the heating programme ($\leq$ 1000 °C). From the Porod slopes, these particles are found to be surface fractals. It is therefore concluded that the nano-structure of the zirconia coating changes significantly in the range 550 °C $\leq T \leq$ 850 °C (see figure 6.29).

The reason for the discrepancy in the results from the SAXS- and from the GISAXS experiment is probably due to the GISAXS experiment only measuring the surface layers of the zirconia coating, whilst the SAXS experiment is measuring the entire thickness of the sample, including the mica substrate, in transmission set-up. The coating procedure was also different; for the SAXS experiment, the mica was left to soak in a zirconia-sol for a week, whilst for the GISAXS experiment, dip-coating was performed.

In principle, these differences between the SAXS and GISAXS results could be used for obtaining depth-sensitive information, such as particle size at different depths. However, in this case, this is not trivial because we did not succeed in subtracting the signal from the mica from the total signal of the SAXS measurement.

A better way of getting depth sensitive information would be to vary the incident angle in the GISAXS experiment. This has already been done for the zirconia sample heated to 500 °C, and for this sample we found that the radius of gyration and the average separation distance remained similar for the measurements performed using different incident angles, and that the Porod slope changed only slightly. But similar measurements should also have been performed for samples heated to higher temperatures, such as 1000 °C, in order to investigate whether the parameters, such as the radius of gyration, still remain approximately constant, or whether there indeed is a difference between the surface layer and the interior of the film. This is something that would be interesting to measure and investigate in the future.

7.1.2 Yttria-doped zirconia

At low temperatures the particles were found to be having small size and rough surface structure. As the temperature is increased, the size of, as well as the average distance between, the scattering particles were found to increase. The surface structure was found to become smoother with increased temperature, and then become rougher again at the highest temperatures (see figures 6.20 and 6.30).

7.2 *In situ* dipping

The SAXS pattern did not change significantly for the different number of dipping cycles; especially the sizes (radius of gyration, correlation distance and average

separation distance) remained at a nearly constant value. The most noticeable difference is the significant increase of scattering particles in each layer which was found to follow a power law for the measurements at 700 °C (see figure 6.13).

The SAXS patterns from the sample containing 4.17 mol% yttria measured at 500 and 700 °C were found to be significantly different (see figure 5.2): The hypothesis for this system is a gradual transition of these coatings from a polymer structure based on a hydrocarbon backbone to one with a Zr-O-Zr backbone. At 500 °C many of the organic chain molecules will have evaporated leaving behind pores and some organic residue; the coating is left in the state of a porous low-density zirconia-"polymer". At 700 °C, however, the sample is almost entirely ceramic.

The XRD measurement from the zirconia sample which was heated to 500 °C was having quite broad Bragg peaks, and was found to show mainly cubic structure. This is not contradictory to the hypothesis about the sample coating being a low-density zirconia-"polymer" because the SAXS result refers to the nanostructure, which is polymeric and porous. The XRD result shows that the Zr and O atoms are arranged locally in the same way as in cubic ZrO_2, but with more disorder (broadening). Locally, the structure is cubic (perhaps containing small amount of tetragonal domains), but the porosity disrupts the alignment of lattice planes and broad Bragg peaks are therefore observed in the measured XRD pattern (see figure 5.10).

7.3 The effect of different yttria concentration

From the results of the *in situ* dipping experiment when the furnace was set to 500 °C, it seems that for the yttrium-doped coatings, the more yttria, the more of the gelation process has taken place.

For all of the samples having different concentrations, the GISAXS experiment showed that the particle size is increasing as the temperature is increased. The particle size was found to be almost the same for the samples with the lowest yttria content (2.04 and 4.17 mol%). The particle size within the sample with the higher yttria content (19.1 mol%) was found to be significantly smaller (see figure 6.30).

The Porod slopes extracted from the GISAXS experiments showed that for low and medium temperatures, the surface structure of the particles go from being rough (probably mass fractals), becoming smoother (surface fractals), to being smooth at temperatures around 800 °C. Then the surface structure was found to become rougher again at the highest temperatures, and a correlation was observed between the yttria content and the temperature for this transition; the more yttria, the earlier (*i.e.* at lower temperature) this transition started (see figure 6.30).

The suggested hypothesis for why rougher particles are observed at lower temperatures for higher yttria content is as follows: Growth instabilities occur when different configurations compete. If there is more yttrium in the structure than zirconia can accommodate comfortably, there are two competing processes: one will try to minimise the surface area and the other will try and segregate yttria.

As a result, yttria-rich pockets form, but they do not fit in with the low-yttria YSZ structure, resulting in a rougher particle. The more yttria there is, the stronger is this second process, and the lower is the temperature at which this roughening occurs. Consequently, we suggest that particles segregate into regions of higher and lower yttria content at high temperatures. Further investigations are required which have not been possible in the scope of this project, and they will be discussed in the Outlook section (Section 8.2).

Chapter 8

Conclusion and Outlook

8.1 Conclusion

Zirconia and yttria-doped zirconia (ZrO_2-Y_2O_3) films, containing different concentrations of yttria, have been produced by sol-gel routes and dip-coating, and investigated using the X-ray techniques SAXS (small-angle X-ray scattering), GISAXS (grazing-incidence -SAXS) and XRD (X-ray diffraction). The latter has been used *ex situ* for structural determination of the films, whilst the small-angle scattering techniques, SAXS and GISAXS, have been used for studying the development of the nano-structure of the films under *in situ* conditions. The main aim of this work was to investigate how the results obtained from the *in situ* measurements could be quantitatively compared, and to figure out the nano-structural behaviour of the films as they underwent processes such as incremental heating and heating-and-dip-coating cycles.

It is not difficult to obtain quantitative SAXS data under *in situ* heating, since the sample geometry does not change with increased temperature. For GISAXS however, this is not quite so simple, and in this thesis I have demonstrated a procedure which allows data sets measured at different temperatures to be quantitatively compared.

The *in situ* heating GISAXS experiments showed that particles undergo Ostwald ripening as the temperature is increased, and that the surface structure of the particles vary between being rough and being smooth for different temperatures. The high temperature transition towards rougher particles was found to start at lower temperatures the higher the yttria content is in the coatings. This suggests that yttria-rich particles segregate into regions of higher and lower yttria content at higher temperatures.

These films have also been prepared during an *in situ* dipping-and-heating SAXS experiment, and it was found that when the sample was heated to 500 °C between each dip and measurement the coating behaved as a porous low-density polymer where the local structure is mainly cubic, but could also have domains of tetragonal structure. When the sample was heated to 700 °C, however, the sample coating was found to form a ceramic.

8.2 Outlook

The nanostructure of zirconia and yttria-doped zirconia coatings was investigated in this work, and so far only using the techniques XRD, (GI)SAXS and ellipsom-

etry. In order to obtain more depth-sensitive information about the samples, it would be interesting to perform an additional GISAXS experiment on the samples which are heated to higher temperatures (for example 1000 °C) using different incident angles.

These X-ray techniques just mentioned give a good overview of the distribution of particles, but less information about parameters such as individual particle shapes. For example, it would be necessary to employ other techniques in order to validate the hypothesis about the particles segregating into regions of higher and lower yttria content. As an outlook for future studies, it is suggested that the coatings should be investigated further, for example using an imaging technique such as SEM (scanning electron microscopy) or a chemically sensitive imaging technique, such as PEEM (photoemission electron microscopy).

SAXS and GISAXS was found to be well suited techniques for studying films and coatings during *in situ* treatment. The *in situ* heating measurements are important for obtaining information about the structure of protective coatings as the sample is heated to very high working temperature. Moreover, this technique has a wide range of uses for *in situ* experiments where dynamic structures of films need to be studied.

List of commonly used symbols

Below is a list of symbols used in this thesis, along with a description and the page number where each symbol is first explained.

$-P$ Porod slope , page 27

$2\theta_f$ Scattering angle parallel to sample plane , page 44

2θ scattering angle , page 17

$\alpha(T)$ Thermal expansion coefficient , page 73

α_c Critical angle of total external reflection , page 34

α_f Exit angle of scattered beam , page 44

α_i Incident angle , page 32

α_t Refracted angle , page 32

$\bar{a}$ Average separation distance , page 28

β Broadening of diffraction line (FWHM) , page 131

β Correction to the refractive index, imaginary part , page 39

δ Correction to the refractive index, real part , page 39

Λ Penetration depth , page 41

λ Wavelength , page 14

$\hat{\mathbf{e}}_i$ Unit vector ($i = \{x, y, z\}$) , page 16

$\mathbf{E}$ Electric field , page 16

$\mathbf{k}$ Wave-vector , page 17

$\mathbf{k}_f$ Wave-vector of the scattered wave , page 17

$\mathbf{k}_i$ Wave-vector of the incident wave , page 17

$\mathbf{k}_r$ Wave-vector of specularly reflected wave , page 35

$\mathbf{q}$ wave-vector transfer vector , page 17

$\mathbf{r}'$ Distance vector between scattering centre and origin , page 18

$\mathbf{r}$ Real space distance vector , page 16

$\mathcal{R}$ Intensity reflectivity , page 47

$\mathcal{T}$ Intensity transmittivity , page 47

μ Linear absorption coefficient , page 32

μ Mean value , page 22

ω Angular frequency of X-rays , page 17

ϕ Phase , page 18

ρ Mass density , page 34

ρ_e Electron density , page 19

σ Standard deviation , page 22

θ_B Bragg angle , page 15

A Amplitude , page 16

A Atomic mass [u] , page 34

A' Group of physical constants: $(N_A r_e)/(2\pi)$, page 38

B Prefactor for Porod term , page 29

C Constant

c Velocity of light in vacuum , page 15

D Sample-Detector distance , page 67

d Distance between lattice planes , page 15

E Energy , page 14

e Magnitude of electronic charge , page 33

f' Anomalous correction factor, real part , page 38

f'' Anomalous correction factor, imaginary part , page 38

$F(\mathbf{q}, \mathbf{r}')$ Form factor amplitude , page 20

f_a Atomic scattering factor ($f_a = f_{a0} + f' + if''$) , page 34

F_{hkl} Structure factor for a Bragg reflection , page 54

G Prefactor for Guinier term , page 29

h Planck's constant , page 15

I Intensity , page 18

K Constant used for Scherrer analysis , page 132

m_e Mass of electron , page 33

N Number of pixels or channels , page 78

n Effective refractive index between two media , page 32

N_A Avogadro's number , page 33

n_e Number of electrons , page 29

n_f Refractive index for medium f , page 32

n_i Relative molar content , page 39

N_p Number of irradiated particles , page 22

$P(\mathbf{q}, \mathbf{r}')$ Form factor , page 21

R Radius of spherical particle , page 22

r Reflected amplitude coefficient , page 46

r_e Classical electron radius , page 37

R_g Radius of gyration , page 25

s Pixel size , page 78

$S(q)$ Structure factor , page 28

S_p Surface area of particle , page 30

T Temperature

t Grain size obtained by Scherrer analysis , page 132

t Transmitted amplitude coefficient , page 47

u_{norm} $= (R_g^4 B)/(1.62G)$, page 157

V_p Particle volume , page 20

w $= \sigma/\sqrt{2}$, page 29

y_0 Horizontal position (pixel number) of the beam centre , page 91

z_0 Vertical position (pixel number) of sample plane , page 92

Bibliography

[1] I. Gurrappa. Thermal barrier coatings for hot corrosion resistance of CM 247 LC superalloy. *Journal Of Materials Science Letters*, 17(15):1267–1269, 1998.

[2] R. Taylor, J. R. Brandon, and P. Morrell. Microstructure, composition and property relationships of plasma-sprayed thermal barrier coatings. *Surface & Coatings Technology*, 50(2):141–149, 1992.

[3] X. Chen, Z. Mutasim, J. Price, J. P. Feist, A. L. Heyes, and S. Seefeldt. Industrial Sensor TBCs: Studies on Temperature Detection and Durability. *International Journal of Applied Ceramic Technology*, 2(5):414–421, 2005.

[4] S. P. Terblanche. Thermal-expansion coefficients of yttria-stabilized cubic zirconias. *Journal Of Applied Crystallography*, 22:283–284, 1989.

[5] H. Hayashi, T. Saitou, N. Maruyama, H. Inaba, K Kawamura, and M. Mori. Thermal expansion coefficient of yttria stabilized zirconia for various yttria contents. *Solid State Ionics*, 176(5-6):613 – 619, 2005.

[6] P. Salas, J. Montoya, V. M. Castao, and R. Rodrguez. Segregation effects in sol-gel zirconia-silica materials analyzed through their radial distribution functions. *Materials Research Innovations*, 3(4):205–211, 2000.

[7] http://cst-www.nrl.navy.mil/lattice/spcgrp/index.html.

[8] D. N. Wang, Y. Q. Guo, K. M. Liang, and K. Tao. Crystal structure of zirconia by Rietveld refinement. *Science In China Series A-Mathematics Physics Astronomy*, 42(1):80–86, 1999.

[9] A. Predith, G. Ceder, C. Wolverton, K. Persson, and T. Mueller. *Ab initio* prediction of ordered ground-state structures in ZrO_2-Y_2O_3. *Physical Review B*, 77(14):144104, 2008.

[10] E. C. Subbarao and H. S. Maiti. Solid Electrolytes With Oxygen Ion Conduction. *Solid State Ionics*, 11(4):317–338, 1984.

[11] C. N. Chervin, B. J. Clapsaddle, H. W. Chiu, A. E. Gash, J. H. Satcher, and S. M. Kauzlarich. Aerogel synthesis of yttria-stabilized zirconia by a non-alkoxide sol-gel route. *Chemistry Of Materials*, 17(13):3345–3351, 2005.

[12] H. G. Scott. Phase Relationships In Zirconia-Yttria System. *Journal Of Materials Science*, 10(9):1527–1535, 1975.

[13] Alexander Tikhonovsky. *Plastic deformation of cubic zirconia single crystals - the influence of the orientation of compression axis and yttria stabilizer content*. PhD thesis, der Mathematisch-Naturwissenschaftlich-Technischen Fakultät der Martin-Luther-Universität Halle-Wittenberg, 2001. Chapter 3.

[14] T. Barnardo, K. Hoydalsvik, R. Winter, C. M. Martin, and G. F. Clark. In Situ Double Anomalous Small-Angle X-ray Scattering of the Sintering and Calcination of Sol-Gel Prepared Yttria-Stabilized-Zirconia Ceramics. *Journal of Physical Chemistry C*, 113(23):10021–10028, 2009.

[15] S. Garcia-Martin, D. P. Fagg, and J. T. S. Irvine. Characterization of diffuse scattering in yttria-stabilized zirconia by electron diffraction and high-resolution transmission electron microscopy. *Chemistry Of Materials*, 20(18):5933–5938, 2008.

[16] I. R. Gibson, G. P. Dransfield, and J. T. S. Irvine. Sinterability of commercial 8 mol% yttria-stabilized zirconia powders and the effect of sintered density on the ionic conductivity. *Journal of Materials Science*, 33(17):4297–4305, 1998.

[17] M. C. Williams. Solid oxide fuel cells: Fundamentals to systems. *Fuel Cells*, 7(1):78–85, February 2007.

[18] T. Barnardo. *Time Resolved Anomalous Small Angle X-ray Scattering of the Sol-Gel Process*. PhD thesis, Aberystwyth University, 2010.

[19] André Guinier and Gérard Fournet. *Small-Angle Scattering of X-Rays*. Wiley, New York, 1955.

[20] P. Krishnamurti. Studies in X-Ray Diffraction Part 1: The structure of amorphous scattering, Part 2: Colloidal solutions and liquid mixtures. *Indian Journal of Physics*, 5:473–500, 1930.

[21] B. E. Warren. X-ray diffraction study of carbon black. *The Journal of Chemical Physics*, 2(9):551–555, 1934.

[22] O. Glatter and O. Kratky, editors. *Small-Angle X-ray Scattering*. Academic Press, 1982.

[23] John Rodenburg. http://www.rodenburg.org/theory/Ewaldsphere21.html.

[24] J. S. Pedersen. Analysis of small-angle scattering data from colloids and polymer solutions: modeling and least-squares fitting. *Advances In Colloid And Interface Science*, 70:171–210, 1997.

[25] Lord Rayleigh. On the Diffraction of Light by Spheres of Small Relative Index. *Proceedings of the Royal Society of London. Series A, Containing Papers of a Mathematical and Physical Character*, 90(617):219–225, 1914.

[26] T. Chraska, A. H. King, and C. C Berndt. On the size-dependent phase transformation in nanoparticulate zirconia. *Materials Science and Engineering A*, 286(1):169 – 178, 2000.

[27] G. Beaucage, H. K. Kammler, and S. E. Pratsinis. Particle size distributions from small-angle scattering using global scattering functions. *Journal Of Applied Crystallography*, 37:523–535, 2004.

[28] Karl Rottmann. *Mathematische Formel-sammlung*. B.I. Hochschultaschenbücher. Bibliographisches Institut Wissenschaftsverlag, 2nd edition, 1960.

[29] G. Kostorz. *Physical Metallurgy*, chapter 12, pages 1115–1199. North-Holland, 1996. p. 1165.

[30] Small-Angle X-ray (Neutron) Scattering (SAXS). http://www.eng.uc.edu/ gbeaucag/Classes/XRD/SAXS

[31] J. R. Levine, L. B. Cohen, Y. W. Chung, and P. Georgopoulos. Grazing-Incidence Small-Angle X-Ray-Scattering - New Tool For Studying Thin-Film Growth. *Journal Of Applied Crystallography*, 22:528–532, 1989.

[32] D. Le Messurier, R. Winter, and C. M. Martin. *In situ* SAXS studies of the morphological changes of an alumina-zirconia-silicate ceramic during its formation. *Journal Of Applied Crystallography*, 39:589–594, 2006.

[33] R. Hosemann. Die parakristalline feinstruktur naturlicher und synthetischer eiweisse - visuelles naherungsverfahren zur bestimmung der schwankungstensoren von gitterzellen. *Acta Crystallographica*, 4(6):520–530, 1951.

[34] R. Hosemann and S. N. Bagchi. The interference theory of ideal paracrystals. *Acta Crystallographica*, 5(5):612–614, 1952.

[35] G. Beaucage and D. W. Schaefer. Structural Studies Of Complex-Systems Using Small-Angle Scattering - A Unified Guinier Power-Law Approach. *Journal Of Non-Crystalline Solids*, 172:797–805, 1994.

[36] S. Lenz, S. K. Nett, M. Memesa, R. F. Roskamp, A. Timmann, S. V. Roth, R. Berger, and J. S. Gutmann. Thermal Response of Surface Grafted Two-Dimensional Polystyrene (PS)/Polyvinylmethylether (PVME) Blend Films. *Macromolecules*, 43(2):1108–1116, 2010.

[37] G. Beaucage. Approximations leading to a unified exponential power-law approach to small-angle scattering. *Journal Of Applied Crystallography*, 28:717–728, 1995.

[38] K. V. Kravchyk, Yu. P. Gomza, O. V. Pashkova, O. I. V'yunov, S. D. Nesin, and A. G. Belous. Effect of synthesis conditions on the fractal structure of yttrium-stabilized zirconium dioxide. *Journal of Non-Crystalline Solids*, 355(52-54):2557–2561, 2009.

[39] G. Renaud, R. Lazzari, and F. Leroy. Probing surface and interface morphology with Grazing Incidence Small Angle X-Ray Scattering. *Surface Science Reports*, 64(8):255–380, 2009.

[40] L. G. Parratt. Surface Studies Of Solids By Total Reflection Of X-Rays. *Physical Review*, 95(2):359–369, 1954.

[41] Y. Yoneda. Anomalous Surface Reflection Of X Rays. *Physical Review*, 131(5):2010–2013, 1963.

[42] O. J. Guentert. Study of anomalous surface reflection of x rays. *Journal Of Applied Physics*, 36(4):1361–1366, 1965.

[43] I. S. Grant and W. R. Phillips. *Electromagnetism*. Wiley, 2nd edition, 1990.

[44] http://physics.nist.gov/cuu/constants/index.html. *CODATA 2006*.

[45] Mario Birkholz. *Thin Film Analysis by X-Ray Scattering*. Wiley-VCH, 2006. Birkholz does actually use Avogadro's number, but calls it Loschmidt's number.

[46] G. H. Vineyard. Grazing-Incidence Diffraction And The Distorted-Wave Approximation For The Study Of Surfaces. *Physical Review B*, 26(8):4146–4159, 1982.

[47] M. F. Toney and S. Brennan. Observation Of The Effect Of Refraction On X-Rays Diffracted In A Grazing-Incidence Asymmetric Bragg Geometry. *Physical Review B*, 39(11):7963–7966, 1989.

[48] J. R. L. Parrill, P. Georgopoulos, Y. W. Chung, and J. B. Cohen. Gisaxs - Glancing Incidence Small-Angle X-Ray-Scattering. *JOURNAL DE PHYSIQUE IV*, 3(C8):411–417, 1993.

[49] W. C. Marra, P. Eisenberger, and A. Y. Cho. X-Ray Total-External-Reflection-Bragg Diffraction - Structural Study Of The GaAs-Al Interface. *Journal Of Applied Physics*, 50(11):6927–6933, 1979.

[50] P. Müller-Buschbaum. *A Basic Introduction to Grazing Incidence Small-angle X-ray Scattering*, chapter 3, pages 61–89. Springer, 2009. Book title: Applications of synchrotron light to scattering and diffraction in materials and life sciences.

[51] J. Als-Nielsen and D. McMorrow. *Elements of Modern X-ray Physics*. Wiley, 2001.

[52] Francis A. Jenkins and Harvey Elliott White. *Fundamentals of optics*. McGraw-Hill, 4th edition, 1981.

[53] Alain Gibaud. *X-Ray and Neutron Reflectivity: Principles and Applications*, chapter 3: Specular Reflectivity from Smooth and Rough Surfaces, pages 87–120. Springer, 1999.

[54] S. K. Sinha, E. B. Sirota, S. Garoff, and H. B. Stanley. X-ray and neutron-scattering from rough surfaces. *Physical Review B*, 38(4):2297–2311, 1988.

[55] http://www.gisaxs.de/theory.html.

[56] B. E. Warren. *X-Ray Diffraction*. Addison-Wesley, 1969.

[57] L. Combemale, G. Caboche, D. Stuerga, and D. Chaumont. Microwave synthesis of yttria stabilized zirconia. *Materials Research Bulletin*, 40(3):529 – 536, 2005.

[58] http://www.rapidonline.com/electronic-components/semiconductor-hardware/transistor-mounting/to-220-kits-type-2/31563.

[59] C. J. Brinker and A. J. Hurd. Fundamentals Of Sol-Gel Dip-Coating. *Journal de Physique III*, 4(7):1231–1242, July 1994.

[60] L. D. Landau and B. G. Levich. Dragging of a liquid by a moving plate. *Acta Physiochim, U. R. S. S.*, 17:42–54, 1942.

[61] K. Hoydalsvik, T. Barnardo, R. Winter, S. Haas, D. Tatchev, and A. Hoell. Yttria-zirconia coatings studied by grazing-incidence small-angle x-ray scattering during in situ heating. *Physical Chemistry Chemical Physics*, 12(43):14492–14500, 2010.

[62] Y. Okada and Y. Tokumaru. Precise determination of lattice parameter and thermal expansion coefficient of silicon between 300 and 1500 K. *Journal of Applied Physics*, 56(2):314–320, 1984.

[63] T. C. Huang, H. Toraya, T. N. Blanton, and Y. Wu. X-ray powder diffraction analysis of silver behenate, a possible low-angle diffraction standard. *Journal of Applied Crystallography*, 26(2):180–184, 1993.

[64] W. H. Press, S. A. Teukolsky, W. T. Vetterling, and B. P. Flannery. *Numerical Recipes in C*. Cambridge University Press, 2nd edition, 1992. Chap. 12.2.

[65] B. Lee, C. T. Lo, S. Seifert, and R. E. Winans. Silver behenate as a calibration standard of grazing-incidence small-angle X-ray scattering. *Journal of Applied Crystallography*, 39(5):749–751, 2006.

[66] B. Kutsch, O. Lyon, M. Schmitt, M. Mennig, and H. Schmidt. Small-angle x-ray scattering experiments in grazing incidence on sol-gel coatings containing nano-scaled colloids: A new technique for investigating thin coatings and films. *Journal Of Applied Crystallography*, 30:948–956, 1997.

[67] D. Babonneau, A. Naudon, D. Thiaudiere, and S. Lequien. Morphological characterization of ion-sputtered C-Ag C/C-Ag and Ag/C films by GISAXS. *Journal Of Applied Crystallography*, 32:226–233, 1999.

[68] M. Buljan, K. Salamon, P. Dubcek, S. Bernstorff, I. D. Desnica-Frankovic, O. Milat, and U. V. Desnica. Analysis of 2D GISAXS patterns obtained on semiconductor nanocrystals. *Vacuum*, 71(1-2):65 – 70, 2003. Proceedings of the 9th Joint Vacuum Conference (JVC-9), organised by the Austrian Vacuum Society, in cooperation with the Vacuum societies of Hungary, Croatia, Slovenia, Czech Republic, Slovakia and Italy, Schloss Seggau, Austria.

[69] R. Lazzari. IsGISAXS: a program for grazing-incidence small-angle X-ray scattering analysis of supported islands. *Journal Of Applied Crystallography*, 35:406–421, 2002.

[70] P. Lenormand, A. Lecomte, D. Babonneau, and A. Dauger. X-ray reflectivity, diffraction and grazing incidence small angle x-ray scattering as complementary methods in the microstructural study of sol-gel zirconia thin films. *Thin Solid Films*, 495(1-2):224–231, 2006.

[71] Lorenz Ratke and Peter W. Voorhees. *Growth and Coarsening: Ostwald Ripening in Material Processing*. Springer, 2002.

[72] W. Ostwald. *Lehrbuch der Allgemeinen Chemie*, volume 2. Leipzig, Germany, 1896. Part 1.

[73] http://lipro.msl.titech.ac.jp/scatfac/scatfac.html.

[74] http://www.gnu.org/software/octave/.

[75] D. W. Breiby, O. Bunk, J. W. Andreasen, H. T. Lemke, and M. M. Nielsen. Simulating X-ray diffraction of textured films. *Journal of Applied Crystallography*, 41(2):262–271, 2008.

[76] Theo Hahn, editor. *International Tables for Crystallography*, volume A: Space-group symmetry. D. Reidel Publishing Company, for the International Union of Crystallography, 1983.

[77] S. Kikkawa, A. Kijima, K. Hirota, and O. Yamamoto. Crystal structure of zirconia prepared with alumina by coprecipitation. *Journal Of The American Ceramic Society*, 85(3):721–723, 2002.

[78] Harold P. Klug and Leroy E. Alexander. *X-ray diffraction procedures: for polycrystalline and amorphous materials*. Wiley, New York, 1954.

[79] L. L. Marton and R. A. Fava, editors. *Methods of Experimental Physics: Polymers Molecular Structure and Dynamics*, volume 16 of Methods of Experimental Physics Series. Academic Press, 1980.

[80] J. A. Bearden. X-ray wavelengths. *Reviews Of Modern Physics*, 39(1):78–124, 1967.

[81] A. W. Burton, K. Ong, T. Rea, and I. Y. Chan. On the estimation of average crystallite size of zeolites from the Scherrer equation: A critical evaluation of its application to zeolites with one-dimensional pore systems. *Microporous and Mesoporous Materials*, 117(1-2):75 – 90, 2009.

[82] K. J. McClellan, S. Q. Xiao, K. P. D. Lagerlof, and A. H. Heuer. Determination Of The Structure Of The Cubic Phase In High-ZrO_2 Y_2O_3-ZrO_2 Alloys By Convergent-Beam Electron-Diffraction. *Philosophical Magazine A-Physics Of Condensed Matter Structure Defects And Mechanical Properties*, 70(1):185–200, 1994.

[83] Y. Zhou and T. C. Lei. Diffusionless Cubic-To-Tetragonal Phase-Transition And Microstructural Evolution In Sintered Zirconia Yttria Ceramics. *Journal Of The American Ceramic Society*, 74(3):633–640, 1991.

[84] M. Yashima, K. Ohtake, M. Kakihana, H. Arashi, and M. Yoshimura. Determination of tetragonal-cubic phase boundary of $Zr_{1-X}R_XO_{2-X/2}$ (R=Nd, Sm, Y, Er and Yb) by Raman scattering. *Journal Of Physics And Chemistry Of Solids*, 57(1):17–24, 1996.

[85] G. H. Aylward and T. J. V. Findlay. *SI chemical data*. Wiley, Brisbane, 1998. 4th ed.

[86] S. Sykora. K-space images of n-dimensional spheres and generalized sinc functions. *Stan's Library (http://www.ebyte.it/library/docs/math07/SincN.html)*, Vol. II, 2007.

[87] B. K. Vainshtein. *Diffraction by Chain Molecules*. Elsevier: Amsterdam, 1966.

Appendix A

Derivation of the form factor amplitude for a sphere.

The particle form factor amplitude $F(\mathbf{q}, \mathbf{r}')$ is related to the Fourier transform of the shape of the particle, and the derivation is described below. Consider first the expression for the scattering amplitude from Eq. (2.13). For one single particle, it takes the form

$$A_p(\mathbf{q}, \mathbf{r}') = \int_{V_p} \rho_e(\mathbf{r}') e^{-i\mathbf{q}\cdot\mathbf{r}'} d\mathbf{r}'. \tag{1}$$

where ρ_e is the electron density within this particle. By using that the electron density is constant within the scattering particle,

$$A_p(\mathbf{q}, \mathbf{r}') = \rho_e \int p(\mathbf{r}') e^{-i\mathbf{q}\cdot\mathbf{r}'} d\mathbf{r}', \tag{2}$$

where $p(\mathbf{r}')$ is the distribution function. The following derivation is based on the webpage in [86], but is here simplified and adapted for the relevant situation.

The distribution function for a homogeneous sphere is given by

$$p(\mathbf{r}') = \begin{cases} 1 & \text{if } |\mathbf{r}'| \leq R \\ 0 & \text{elsewhere} \end{cases} \tag{3}$$

Next, let

$$W(\mathbf{q}, \mathbf{r}') \equiv \int p(\mathbf{r}') e^{-i\mathbf{q}\cdot\mathbf{r}'} d\mathbf{r}' \tag{4}$$

be the n-dimensional q-space representation of a sphere, and thus the scattering amplitude becomes

$$A_p(\mathbf{q}, \mathbf{r}') = \rho_e W(\mathbf{q}, \mathbf{r}'). \tag{5}$$

In the case of a sphere of radius R, $W(\mathbf{q}, \mathbf{r}')$ is replaced by $W(\mathbf{q}, R)$. The symmetry of $p(\mathbf{r}')$ simplifies the solution: For any direction of $\mathbf{q}$, it is possible to rotate the coordinate system to make $\mathbf{q}$ coincide with the first axis, $\mathbf{q} = \{q, 0, \ldots, 0\}$. $W(\mathbf{q}, R)$ depend only on the magnitude $\mathbf{q}$, and not its direction, so we only need to determine the radial profile $W(q, R)$. Using that $\mathbf{q} = \{q, 0, \ldots, 0\}$ and $\mathbf{r}' = \{r_1, r_2, \ldots, r_n\}$, such that $\mathbf{q} \cdot \mathbf{r}' = qr_1$, then

$$W(\mathbf{q}, \mathbf{r}') = W(\mathbf{q}, R) = W(q, R) = \int_{V_R} e^{-iqr_1} d\mathbf{r}' \tag{6}$$

where the integral is taken over the volume V_R. The next step is to scale the integral in Eq. (6) so that the integration extends over the unit volume V_1 of a sphere of unit radius $\hat{r}$. Then, $\mathbf{r}' = R\hat{\mathbf{r}}$, $r_1 = R\hat{r}_1$, $d\mathbf{r}' = R^3 d\hat{\mathbf{r}}$ and by setting $x = -qR$:

$$W(q, R) = R^3 \int_{V_1} e^{ix\hat{r}_1} d\hat{\mathbf{r}}. \tag{7}$$

From this, it can be seen that $W(0, R)$ is the volume of an n-dimensional sphere of radius R, and therefore, due to scaling properties, the ratio $(W(q, R))/(W(0, R))$ depends only on x. For any value of R, a function of x can be defined such that

$$\mathrm{sinc}(n, x) = \frac{W((-x/R), R)}{W(0, R)}. \tag{8}$$

Eq. (8) can be described as the normalised radial profile of the Fourier transform of a uniform n-dimensional sphere with unit volume. By rearranging, we see that

$$W((-x/R), R) = W(0, R) \cdot \mathrm{sinc}(n, x) \tag{9}$$

and for three dimensions ($n = 3$) this becomes

$$W(q, R) = W(0, R) \cdot \mathrm{sinc}(3, x). \tag{10}$$

The general solution for the first factor is given by

$$W(0, R) = R^n \frac{2\pi^{n/2}}{3\Gamma(n/2)}, \tag{11}$$

and for n=3, $\Gamma(3/2) = (1/2)\sqrt{\pi}$ and thus

$$W(0, R) = \frac{4\pi}{3} R^3 \tag{12}$$

for a three-dimensional sphere. The general solution of the second factor in Eq. (10) is

$$\mathrm{sinc}(3, x) = 3\frac{\sin x - x\cos x}{x^3}. \tag{13}$$

By putting Eq. (12) and Eq. (13) into Eq. (10), and setting in for $x = -qR$, the following expression is obtained

$$W(q,R) = 3V_p \frac{\sin(qR) - qR\cos(qR)}{(qR)^3} \tag{14}$$

where $V_p = (4\pi R^3)/3$ is the volume of the spherical particle with radius R. By comparing Eq. (2.14) and Eq. (5), the form factor amplitude is found to be given by $F(q,R) = W(q,R)/V_p$, such that

$$F(q,R) = 3\frac{\sin(qR) - qR\cos(qR)}{(qR)^3}. \tag{15}$$

Appendix B

Derivation of the Hosemann model and the structure factor.

Several papers have published equations for the structure factor based on the Hosemann model, but different versions of this equation were found. Therefore, a summary mostly based on Vainshtein's book [87] is given here.

Densely packed particles cause interference in the scattered intensity, and it is therefore necessary to derive this interference pattern from the distribution function of particles.

When the probability function of the nearest neighbour is known, we know that there is another probability function of nearest neighbours to this one, and so it repeats itself. Say, for example, that the intermolecular distances are not completely fixed, but vary about an average value $\bar{a}$. The probability function for for this molecule is given with a certain width. Next, go to the second neighbour. If starting from the first neighbour, the probability function for the first neighbour, but displaced a distance $\bar{a}$ will be obtained. But now, if instead starting in origin, the probability of the second neighbour can be found from the first neighbour, but since the intermolecular distance have a small uncertainty, this uncertainty will follow through, and cause the probability function of the second neighbour to have the same shape as the first neighbour, but broader; the standard deviation increase. It therefore seems logical that the probability function of the second neighbour is the self-convolution of the first neighbour.

The *disposition function* $A(\mathbf{r})$ can be used to specify an array of identical

scattering units in space, such as positions of the centres of gravity. Here we use the disposition function to describe a set of N points lying at the ends of vectors $\mathbf{r}_j$,

$$A(\mathbf{r}) \equiv \sum_{j=1}^{N} \delta(\mathbf{r} - \mathbf{r}_j). \tag{16}$$

Now, the distribution function is defined as the *self-convolution* of $A(\mathbf{r})$:

$$W(\mathbf{r}) \equiv A(\mathbf{r}) * A(\mathbf{r}) = \int A(\mathbf{r}')A(\mathbf{r}' - \mathbf{r})d\mathbf{r}' \tag{17}$$

The structure factor can be found from the Fourier transform of the *normalised distribution function*, $P(x) = W(x)/N$, where $P(x)$ is obtained as follows: First we find the distribution function for the second neighbour based on the information we have about the first neighbour. This model uses the convolution of H_1 with itself: H_1 is displaced from the origin and has a certain width; convolution produces once more the same displacement and same broadening. The result is a broader function of lower peak height,

$$H_2(x) = \int_0^\infty H_1(x')H_1(x - x')dx' = H_1 * H_1 = \tilde{H_1}^2. \tag{18}$$

The normalised distribution function is given as

$$P(x) = H_0 + \sum_{m=1}^{\infty} [\tilde{H_1}^m + \tilde{H_{-1}}^m], \tag{19}$$

where

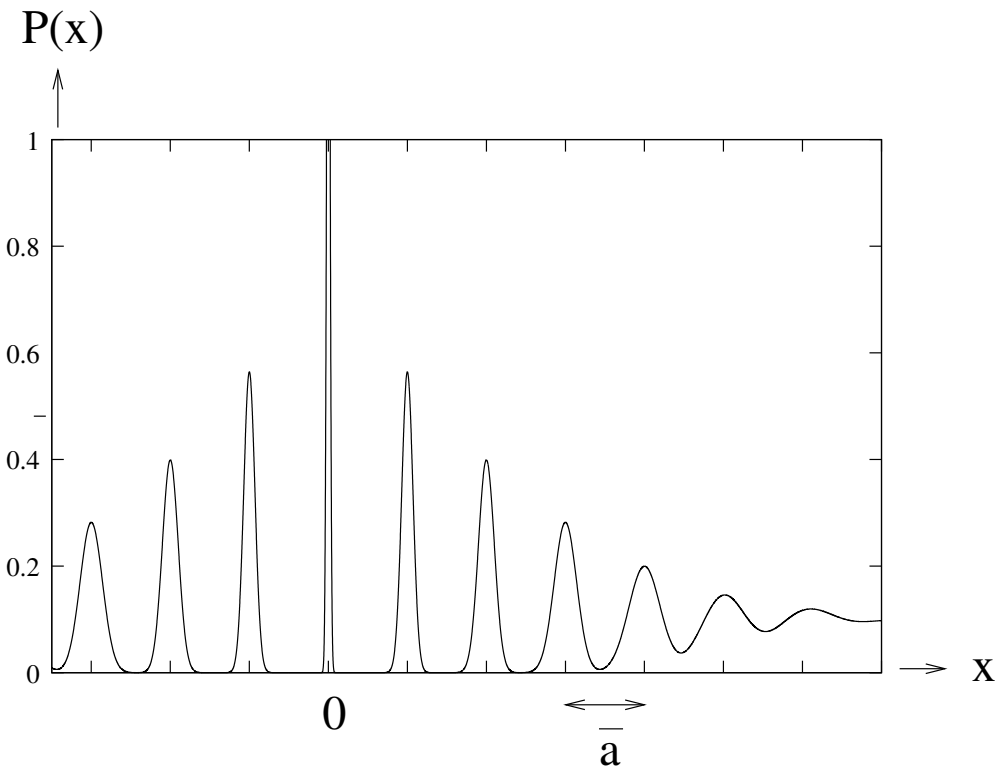

Figure 1: The normalised distribution function, $P(x)$. The peak at $x = 0$ is $H_0(x)$, whilst the peak to the left and right of it is $H_{-1}(x)$ and $H_1(x)$, respectively. The total normalised distribution function is the sum of each of these terms. In the figure, a Gaussian distribution function is used for describing the peaks, each tic on the x-axis is at intervals of $x = 10$, and the average separation distance between particles was in this case set to $\bar{a} = 10x$, such that each tic corresponds to $\bar{a}$. For the first order peaks, $H_{-1}(x)$ and $H_1(x)$, the standard deviation was set to $\sigma = 2\sqrt{2}$, and for each consecutive peak the standard deviation increase with $\sqrt{2}$ compared to the previous peak (because of the self-convolution of the Gaussian function).

$$H_0(x) = \delta(x) \tag{20}$$

is simply the delta function, and it is plotted in figure 1.

The structure factor can now be found by Fourier transform of $P(x)$:

$$S(q) = \mathcal{F}[P(x)] = \mathcal{F}[H_0 + \sum_{m=1}^{\infty} [\tilde{H_1}^m + \tilde{H_{-1}}^m]] \tag{21}$$

$$= \mathcal{F}[H_0] + \mathcal{F}[\sum_{m=1}^{\infty} [\tilde{H_1}^m + \tilde{H_{-1}}^m]] \tag{22}$$

$$= \mathcal{F}[\delta(x)] + \mathcal{F}[\sum_{m=1}^{\infty} \tilde{H_1}^m] + \mathcal{F}[\sum_{m=1}^{\infty} \tilde{H_{-1}}^m] \tag{23}$$

$$= 1 + \sum_{m=1}^{\infty} B^m(q) + \sum_{m=1}^{\infty} B^{*m}(q) \tag{24}$$

where we have used that the transform of the delta function is 1, $\mathcal{F}[H_1(x)] \equiv B(q)$, $\mathcal{F}[H_m(x)] \equiv B^m(q)$ and $\mathcal{F}[H_{-m}(x)] = B^{*m}(q)$.

By using the geometric series

$$\sum_{m=1}^{\infty} B^m(q) = \frac{B(q)}{1 - B(q)}, \tag{25}$$

we get that

$$S(q) = 1 + \frac{B}{1 - B} + \frac{B^*}{1 - B^*}. \tag{26}$$

The modulus and phase can be used to represent the complex $B(q)$:

$$B = |B| \exp(i\phi) \qquad \text{and} \qquad B^* = |B| \exp(-i\phi) \tag{27}$$

This gives the result

$$S(q) = \frac{1 - |B|^2}{1 - 2|B|\cos\phi + |B|^2}, \tag{28}$$

where it has been used that $e^{i\phi} + e^{-i\phi} = 2\cos\phi$. The operation of the displacement on a distance $\bar{a}$ in object space corresponds to the appearance of a phase factor in reciprocal space:

$$\exp(i\phi) = \exp(2\pi i q\bar{a}) \tag{29}$$

such that

$$\phi = 2\pi q\bar{a}. \tag{30}$$

$B(q)$ and $P(x)$ is governed by the format of $H_1(x)$. $H_1(x)$ is normally *not* symmetric, but we neglect this in the first approximation. The Gaussian distribution around origin is given by

$$f(x) = \frac{1}{\sqrt{2\pi}\sigma} e^{-\frac{1}{2}(x^2/\sigma^2)}. \tag{31}$$

Next the substitution $w \equiv (\sigma/\sqrt{2})$ is used:

$$f(x) = \frac{1}{2w\sqrt{\pi}} e^{-x^2/4w^2}. \tag{32}$$

H_1 is here a Gaussian curve that is displaced with the distance $\bar{a}$:

$$H_1(x-\bar{a}) = \frac{1}{2w\sqrt{\pi}} e^{-(x-\bar{a})^2/4w^2} \tag{33}$$

The Fourier transform of $f(x)$ can be solved by

$$g(q) = \int_{-\infty}^{\infty} f(x) e^{iqx} dx = \frac{1}{2w\sqrt{\pi}} \int_{-\infty}^{\infty} e^{-x^2/4w^2} e^{iqx} dx = \frac{1}{2w\sqrt{\pi}} I \tag{34}$$

where

$$\begin{aligned} I &= \int_{-\infty}^{\infty} e^{-x^2/4w^2} e^{iqx} dx \\ &= \int_{-\infty}^{\infty} e^{-\left(\frac{x}{2w}\right)^2 + iqx} dx \cdot e^{A^2q^2} e^{-A^2q^2} \\ &= e^{A^2q^2} \int_{-\infty}^{\infty} e^{-\frac{x^2}{4w^2} + iqx - A^2q^2} dx \end{aligned} \tag{35}$$

where we have used the trick of completing the square. Now we use that

$$-\left(\frac{x}{2w} - Aq\right)^2 = -\frac{x^2}{4w^2} + \frac{A}{w} qx - A^2q^2 \tag{36}$$

where we match the cross terms in Eqs. (35) and (36) in order to determine A. The result is $A = iw$, and consequently;

$$A^2 = -w^2. \tag{37}$$

From Eqs. (35) and (36), we see that

$$I = e^{A^2q^2} \int_{-\infty}^{\infty} e^{-\left(\frac{x}{2w} - Aq\right)^2} dx, \tag{38}$$

and by setting in for A^2,

$$I = e^{-w^2q^2} \int_{-\infty}^{\infty} e^{-\frac{(x-2wqA)^2}{(2w)^2}}. \tag{39}$$

This is a Gaussian integral, and it can be solved by using that

$$\int_{-\infty}^{\infty} e^{-\frac{(x+b)^2}{c^2}} dx = c\sqrt{\pi}. \tag{40}$$

The result is

$$I = e^{-w^2q^2} 2w\sqrt{\pi} \tag{41}$$

and putting this result back into Eq. (34) shows that the Fourier transform of the Gaussian probability function $f(x)$ (Eq. (32)) is given by

$$g(q) = e^{-w^2q^2}. \tag{42}$$

Displacement of a function ($x \to x - \bar{a}$) causes the result of the Fourier transform to be multiplied with another phase factor

$$\mathcal{F}[H_1(x - \bar{a})] = g(q)e^{-iq\bar{a}}, \tag{43}$$

such that

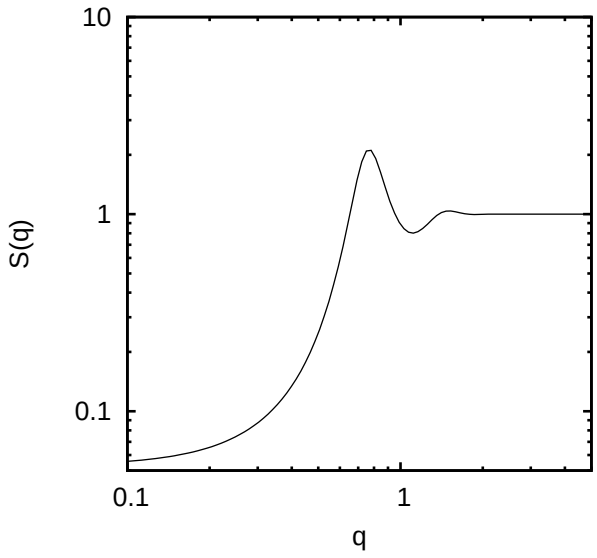

Figure 2: The structure factor from Eq. (46) plotted using $\bar{a} = 8$ nm and $w = 1.3$ nm ($\sigma = 1.84$ nm).

$$\mathcal{F}[H_1(x - \bar{a})] = e^{-w^2q^2}e^{-iq\bar{a}}. \tag{44}$$

However, only the amplitude and not the phase are needed for Eq. (28):

$$|B| = \exp(-w^2q^2). \tag{45}$$

Putting this into Eq. (28), the following expression for the structure factor is obtained:

$$S(q) = \frac{1 - \exp(-2w^2q^2)}{1 - 2\exp(-w^2q^2)\cos(q\bar{a}) + \exp(-2w^2q^2)} \tag{46}$$

where we have used that $\cos\phi = \cos(2\pi q\bar{a}) = \cos(q\bar{a})$. This expression is plotted in figure 2.

Appendix C

Octave script for performing the reflectivity calculations.

```
clear all; close all;
format short
% Author: Kristin Hoydalsvik, khoydalsvik@gmail.com
% Date: 8th Feb. 2010

%%%%%%%%%%%%%%%%%%%%%%%%  Input  %%%%%%%%%%%%%%%%%%%%
% experimental parameters
E=10008; % X-ray energy [eV]
alpha_in=0.257 % incident angle [degrees]

% material parameters
rho=5150;  % Mass density [kg/m3]
rho_s=2330; % Mass density of substate [kg/m3]
t=113; % Film thickness [nm]

% material
n(1) = 0; % Element 1: Si
n(2) = 22.31; % Element 2: Zr
n(3) = 1.94; % Element 3: Y
n(4) = 47.53; % Element 4: O

%%%%%%%%%%%%%%%%%%%%%%%%  Constants  %%%%%%%%%%%%%%%%%

h=4.135667*10^(-15); % Planck's constant [eV*s]
c=299792458; % Speed of light [m/s]
Aprime=2.7009*10^(11);  % constant in delta [m/kg]
E1=10000;
E2=15000;

% Molar mass:
A(1) = 28.086; % Si
A(2) = 91.224; % Zr
A(3) = 88.906; % Y
A(4) = 15.999; % O

% proton number:
Z(1) = 14; % Si
Z(2) = 40; % Zr
```

```
Z(3) = 39; % Y
Z(4) = 8; % O

% Anomalous scattering factor (from e.g.
% http://lipro.msl.titech.ac.jp/scatfac/scatfac.html)
% (for l=1.24 ):
fprime(1) = 0.1841; % Si
fprime(2) = -0.6301; % Zr
fprime(3) = -0.7198; % Y
fprime(4) = 0.0311; % O

fdprime(1) = 0.2164; % Si
fdprime(2) = 1.5318; % Zr
fdprime(3) = 1.3790; % Y
fdprime(4) = 0.0204; % O

% X-Ray Mass Attenuation Coefficients divided by density:
% From http://physics.nist.gov/PhysRefData/
% XrayMassCoef/tab3.html:
% Silicon:
mrE1(1)=33.89; % mu/rho [cm2/g] for E = 10000 eV
mrE2(1)=10.34; % mu/rho [cm2/g] for E = 15000 eV
% Zirconium:
mrE1(2)=74.17; % mu/rho [cm2/g] for E = 10000 eV
mrE2(2)=24.63; % mu/rho [cm2/g] for E = 15000 eV
% Yttrium:
mrE1(3)=68.71; % mu/rho [cm2/g] for E = 10000 eV
mrE2(3)=22.79; % mu/rho [cm2/g] for E = 15000 eV
% Oxygen:
mrE1(4)=5.952; % mu/rho [cm2/g] for E = 10000 eV
mrE2(4)=1.836; % mu/rho [cm2/g] for E = 15000 eV

%%%%%%%%%%%%%%%%%%%%%% Calculations %%%%%%%%%%%%%%%%

nd=size(n)(2);

%%%% X-ray attenuation %%%%%

% Find weight ratio for the components in the molecule:
for i=1:nd
  M(i)=n(i)*A(i);
endfor
mass=sum(M);
```

```
for i=1:nd
   w(i)=M(i)./mass;
endfor

% Extrapolating to find the mr value for used X-ray energy
fr=(E-E1)/(E2-E1);

for i=1:nd
  mrE(i)=mrE1(i)-(mrE1(i)-mrE2(i))*fr;  % mr for given X-ray energy E
endfor

% Adding up the contributions from the different components:
for i=1:nd
  mr(i)=w(i)*mrE(i);
endfor
mr_tot=sum(mr); % mu/rho [cm2/g] for compound molecule

% Linear attenuation coefficient:
rho_g=rho/1000; % density in [g]
mu=mr_tot*rho_g % [cm-1]

%%%%% delta and beta %%%%%%%
lambda=(h*c)/E; % wavelength [m]
d=Aprime * rho * (lambda)^2 ; % prefactor
d_s=Aprime * rho_s * (lambda)^2; % prefactor for the substrate

% evaluate the sums in delta and beta:
for i=1:nd
T1(i)=(n(i).*(Z(i)+fprime(i)));
endfor
T1n=sum(T1);

for i=1:nd
T2(i)=(n(i).*fdprime(i));
endfor
T2n=sum(T2);

for i=1:nd
N(i)=(n(i).*A(i));
endfor
Nn=sum(N);

delta=d*(T1n./Nn)
beta=d*(T2n./Nn)
```

```
%substrate
delta_s=d_s*(Z(1)+fprime(1))./(A(1));
beta_s=d_s*(fdprime(1))./(A(1));

% critical angle
alpha_c_rad=sqrt(2*delta);
alpha_c=(alpha_c_rad*180)/pi() %critical angle [degrees]

%%%%% refractive index %%%%%%%

% Find ni
clear i
n0=1;
n1=1-delta-i*beta; % film
n2=1-delta_s-i*beta_s; % substrate

% effective refractive index
neff01=n1/n0;
neff12=n2/n1;

%format short
% effective angle inside film/substrate
alpha_in_rad=(alpha_in*pi()/180);
alpha1_rad=acos(cos(alpha_in_rad)/neff01);
alpha1=(alpha1_rad*180)/pi()
alpha2_rad=acos(cos(alpha1_rad)/neff12);
alpha2=(alpha2_rad*180)/pi()

%%%% Wavevector %%%%%

% Find k_(z,i) From Gibaud1999, eq. 3.67
clear i;
k0 = (2*pi()) / lambda; % [m]
kz0 = -k0*sin(alpha_in_rad);
kz1 = -k0*sqrt(alpha_in_rad^2-2*delta-2*i*beta);
kz2 = -k0*sqrt(alpha_in_rad^2-2*delta_s-2*i*beta_s);

%%%% Transmission/absorption %%%%%
% travel distance in film:
tcm=t*10^(-7); % film thickness in [cm]
d=tcm/sin(real(alpha1_rad)); % 1/2 travel distance [cm]

tau=exp(-2*mu*d)
```

```
%%%% Penetration depth %%%%%

L=((lambda)/(4*pi()*imag(alpha1_rad)))*10^9 % [nm]

%%%% Fresnel coefficients %%%%%

clear i
r01=(kz0-kz1)/(kz0+kz1);
R1=r01*conj(r01)

t01=(2*kz0)/(kz0+kz1);
T1=t01*conj(t01)

r12=(kz1-kz2)/(kz1+kz2);
R2=r12*conj(r12)

t10=(2*kz1)/(kz1+kz0);
T3=t10*conj(t10)
```

Appendix D

cif-files used for cubic and tetragonal zirconia.

The coordinates and positions are taken from *International Tables for Crystallography, Volume A: Space-group Symmetry.*

Cubic zirconia: Space group: Fm$\bar{3}$m (No. 225)

```
##############################################################

loop_
_symmetry_equiv_pos_site_id
_symmetry_equiv_pos_as_xyz
1 x,y,z
2 x,y+1/2,z+1/2
3 x+1/2,y,z+1/2
4 x+1/2,y+1/2,z

_cell_length_a 5.135
_cell_length_b 5.135
_cell_length_c 5.135
_cell_angle_alpha 90
_cell_angle_beta 90
_cell_angle_gamma 90
loop_
_atom_site_label
_atom_site_type_symbol
_atom_site_fract_x
_atom_site_fract_y
_atom_site_fract_z
Zr1 Zr 0.0000   0.0000   0.0000
O1  O  0.2500   0.2500   0.2500
O2  O  0.2500   0.2500   0.7500
```

Tetragonal zirconia: Space group: $P4_2/nmc$ (No. 137)

```
##################################################################

loop_
_symmetry_equiv_pos_site_id
_symmetry_equiv_pos_as_xyz
1 x,y,z
2 -x+1/2,-y+1/2,z
3 -y+1/2,x,z+1/2
4 y,-x+1/2,z+1/2
5 -x,y+1/2,-z
6 x+1/2,-y,-z
7 y+1/2,x+1/2,-z+1/2
8 -y,-x,-z+1/2
9 -x,-y,-z
10 x+1/2,y+1/2,-z
11 y+1/2,-x,-z+1/2
12 -y,x+1/2,-z+1/2
13 x,-y+1/2,z
14 -x+1/2,y,z
15 -y+1/2,-x+1/2,z+1/2
16 y,x,z+1/2
_cell_length_a 3.596
_cell_length_b 3.596
_cell_length_c 5.177
_cell_angle_alpha 90
_cell_angle_beta 90
_cell_angle_gamma 90
loop_
_atom_site_label
_atom_site_type_symbol
_atom_site_fract_x
_atom_site_fract_y
_atom_site_fract_z
Zr1 Zr 0.75000 0.25000 0.25000
O1  O  0.25000 0.25000 0.05000
```